KARLSTADS UNIVERSITET

Thermal barrier coatings for diesel engine exhaust application

Termiska barriärsskikt för grenrörsapplikationer

Christoffer Blomqvist

Faculty of health, science and technology
Degree project for master of science in engineering, mechanical engineering
30 credit points
Supervisor: Christer Burman
Examiner: Jens Bergström
Date: Spring semester 2014, 2014-06-09

Abstract

The strive to increase the engine efficiency in terms of fuel consumption and lower emissions have lead to higher demands on materials. In this thesis five different thermal barrier coatings applied using air plasma spraying to three materials commonly used for exhaust application are evaluated. This thesis work was done at Scania CV in Södertälje with main focus on evaluation during thermal cycling. The goal of this thesis is to evaluate the coatings and correlate their behaviour to their characteristic microstructure.

The coatings were evaluated through their stability in thermal conductivity, fracture toughness, hardness, porosity and failure modes. The parameters where obtained using laser flash, Vickers indentation, Vickers indentation fracture toughness and microscopic evaluation methods.

The evaluation shows that conventionally used zirconia based materials exhibits low thermal conductivity, high hardness, and stable fracture toughness compared to other evaluated materials. One material that can be applicable in diesel exhaust application is mullite, which showed similar performance to zirconia based materials. For the use of TBC together with SiMo51 a different bondcoat than conventional NiCrAlY needs to be evaluated.

Sammanfattning

Strävan efter att konstruera effektivare motorer för att generera minskade utsläpp och bättre bränsleekonomi har genererat högre krav på konstruktionsmaterialen som används idag. I detta examensarbete som utförts på Scania CV i Södertälje utvärderas fem olika termiska barriärsskikt som belagts med plasma sprayning på tre vanligt förekommande konstruktionsmaterial för grenrör. Målet med detta examensarbete är att utvärdera beläggningarnas beteende under termisk cykling och koppla deras beteende till karakteristiska mikrostrukturer.

Beläggningarna utvärderades genom att jämföra deras värmeledningsförmåga, hårdhet, brottseghet och porositet. Materialparametrarna utvärderades genom laser flash, Vickers hårdhetsmätning, Vickers brottseghet samt mikroskopiska bildanalyser.

Resultaten visar att kommersiellt använda zirkonium baserade material uppvisar låg värmeledningsförmåga, hög hårdhet och hög brottseghet i förhållande till övriga material. Ett annat material som analyserats, mullit, visar på liknande beteenden som zirkonium baserade material men behöver utvärderas ytterligare. Om SiMo51 används som substratmaterial finns behovet att utvärdera användningen av andra typer av bindskikt än det austenitiska NiCrAlY nu använt.

Acknowledgment

I would like to thank everyone at Scania CV in Södertälje for the help with information and interesting discussions during this project. I especially want to thank my supervisor Madeleine Ekström at Scania/KTH for excellent support.

I also want to thank Christer Burman at Karlstad University for great feedback and supervision. I would also like to thank my examiner Jens Bergström.

A Final big thanks to everyone else who has helped me with the project.

Christoffer Blomqvist, Karlstad 27/5-2014

Table of Content

1 Introduction

1.1 Scania

Scania is one of the leading actors in truck manufacturing with operations in over 100 countries. The production is localized in seven countries were 12.400 employees of the total 35.000 is active. The main site, holding production, head office and the research and development, in Södertälje is where the history of Scania started in 1891. The research and development today houses 2.400 employees working together to maintain a leading role as truck and engine manufacturer.

1.2 Background

With continuous legislation within the European union to generate lower emissions a more efficient combustion is preferred to minimize the emission of particles. A more efficient combustion not only lowers the emission in terms of particles but also lowers the fuel consumption. This solution generates positive effects in both economical and environmental terms. This increase in efficiency can be achieved by increasing the combustion pressure resulting in increased fuel efficiency and increased temperatures. The strive to increase efficiency and performance has generated the internal goal for the Scania division NMGV to increase the combustion pressure. With this, the increase in temperature, the exhaust components, mainly the exhaust manifold will experience a much higher strain, generating new and higher demands on construction materials. The material used today exhibits properties that make it less effective at these temperatures resulting in premature failure. A simple solution would be to change to a more durable material, but a more efficient solution, generating decreased heat losses and further increases the efficiency would be to apply a Thermal barrier Coating, TBC to the current material, a ferritic ductile iron named SiMo51, already used material. A TBC is usually a two-component surface coating consisting of a bondcoat and a ceramic topcoat. The ceramic topcoat generates a steep thermal gradient through the coating that can generate temperature difference up to 300^{o}C protecting the substrate material. If a TBC is applied to the component the same material as earlier can be used without resulting in premature failure due to oxidation, phase transformations etc.

1.3 Exhaust manifold and operating conditions

The exhaust manifold primary function is to collect the exhaust from the individual cylinder heads and consolidate the exhausts through the turbo charger. This component, due to its position and function exhibits different operating condition based on both time and position. As can be seen in Fig.1, the manifold stretches from left to right and the flow rate and temperature increases with the numbers of cylinders being connected. Generating the highest temperature and flow rate after all four cylinder heads.

Figure 1 View of exhaust manifold mounted onto Scania engine DC 16. Source: http://scania.com/_system/img/doc/engines/i/DC1686A_566kW.pdf

In the extreme condition the engine generates an operating environment pushing the manifold close to its limit. The exhaust flows with a rate of 40000 litres/min, the exhaust temperature reaches a maximum of 760^{o}C with a pressure of 14bars. These conditions combined with the engine-induced vibrations, that can reach levels up to 20g, and the cyclic nature of the process where the parameters vary with engine load, puts high demands on the intended coating material.

1.4 Thermal barrier coating material

Today when discussing thermal barriers the most widely used material is Yttria stabilized Zirconia, YSZ, due to high thermal stability and close match in thermal expansion to many metallic materials. There are many other ceramic materials to choose from, based on rare earth minerals and other variations of Zirconia, but many have been ruled out due to lower service temperatures than YSZ. The driving force for development in thermal barriers has been the aerospace industry, or more specific the turbine engine manufactures. The operating temperature of turbine engines in aerospace applications exceeds 1000^{o}C, which is well above the maximum temperature reached in the exhaust manifolds of an internal combustion engine. This fact makes it interesting to evaluate materials that have been ruled out for aerospace application for diesel engine applications. Some of the materials, which at least in theory should be able to function within an internal combustion engine, are~~,~~ Mullite, Forsterite, 8YSZ, Nano-sized 8YSZ and $La_2Zr_2O_7$.

To be able to coat the exhaust manifold using TBC the durance of the coating material needs to be evaluated. As mentioned earlier, the manifold connects to the turbo charger, meaning that the consequence if pieces of the coating starts to spall from the surface could generate a turbo failure and complete standstill. This generates the need for a coating system that can withstand induced stresses without cracking, delamination and spallation within a given time period.

The complex geometry of the manifold presents a challenge in terms of coating method. For the TBC method to be effective the coating needs to be applied internally reducing the numbers of coating procedures and almost excludes the conventionally used plasma spray method at the dimensions used. This generates the need to evaluate other, no line of sight, coating methods that can generate durable coatings within economically justified boundaries.

1.5 Objective

The objective of this thesis is to evaluate the thermal cyclic behaviour of five different thermal barrier coatings applied using the conventional Air Plasma spray method. The coatings are applied onto three different substrate materials, which are commonly found in exhaust manifolds of diesel- and gasoline engines. The relationship between characteristic microstructure, chemical composition and thermal properties of the different materials are investigated.

1.6 Restrictions

The restrictions made for this thesis are based on the influence of the elements present in the exhausts that will only be covered in theory. No experimental investigation within hostile environments will be covered. The influence of abrasive wear and vibrations will only be covered in theory. The methods used for evaluating the samples are restricted to in-house equipment for the thermal cycling and methods applicable to the shape and size of the coated samples since no modification or new samples could be done.

2. Theory

The steady increase in interest to produce more efficient combustion engines and at the same time decrease the emissions, with the effect of reduced the fuel consumption and environmental effect of the combustion engines, have led to higher demands of materials [1]. A more efficient engine, in terms of fuel consumption and emissions, generates higher temperatures and materials used earlier can no longer provide the desired lifetime of the component. To be able to combine the desired structural strength with desired high temperature performance, within economically justifiable boundaries, the development and focus of research have been driven towards coatings [2]. The most common coatings for high temperature applications are today thermal barrier coatings, TBC. The TBC is a four-layer coating consisting of a substrate material, a bond coat, a thermally grown oxide layer, TGO and a ceramic topcoat [3], see Fig.2. The primary usage area for thermal barriers today is in turbine engines that operate well above 1000°C [4]. In diesel engines the operating temperature in many components is instead well below 1000°C, making it interesting to examine and evaluate materials that have been ruled out for turbine use.

The overall effect that TBC coatings can have if applied to components in diesel engines can be seen in table 1. As the table states, there are far more positive effects in terms of efficiency then just to increase the power output and reduce the emission. According to Parker, the economical gain from applying the TBC far exceeds the production and application costs of the TBC system [5].

Table 1 effect of thermal barrier coating implementation in diesel engines [5].

Benefit	Percentage change (%)
Fuel savings	11
Engine life extension	20
Power output increase	10
Reduction of emission	20-50
Reductions of particulate	52
Lubricating oil savings	15
Maintenance cost reduction	20

The different layers in the TBC all have different applications. The substrate is the material intended to protect, the bond coat has the first and foremost task to increase the bonding between the substrate and the topcoat and also to decrease oxidation of the substrate. The TGO is an oxide layer intended to protect the substrate and bondcoat from oxidation. The final layer, the topcoat, is a ceramic material intended to decrease the thermal conductivity of the system [2]. For a material to be classified as a suitable candidate for TBC use there are some key material properties that needs to be fulfilled, which are listed below in table 2 [6]. There are today no materials that can be said to fulfil all of the requirements, but there are materials that are seen as good enough.

Table 2: Desired properties of TBC [6]

- Low thermal conductivity.
- Low density that generates low thermal conductivity.
- The outer most surface of the topcoat should in contrary exhibit a dense state to increase the coating resistance to abrasive wear. But also to decrease the absorption of exhausts particles.
- A good strain compliance to withstand thermal expansion mismatches.
- For this specific application ability to maintain compressive stresses in topcoat to reduce crack initiation which reduces risk for chipping out.
- Chemically stable and not react with the chemical compounds in the exhaust.
- Thermally stable within the operating temperature range.

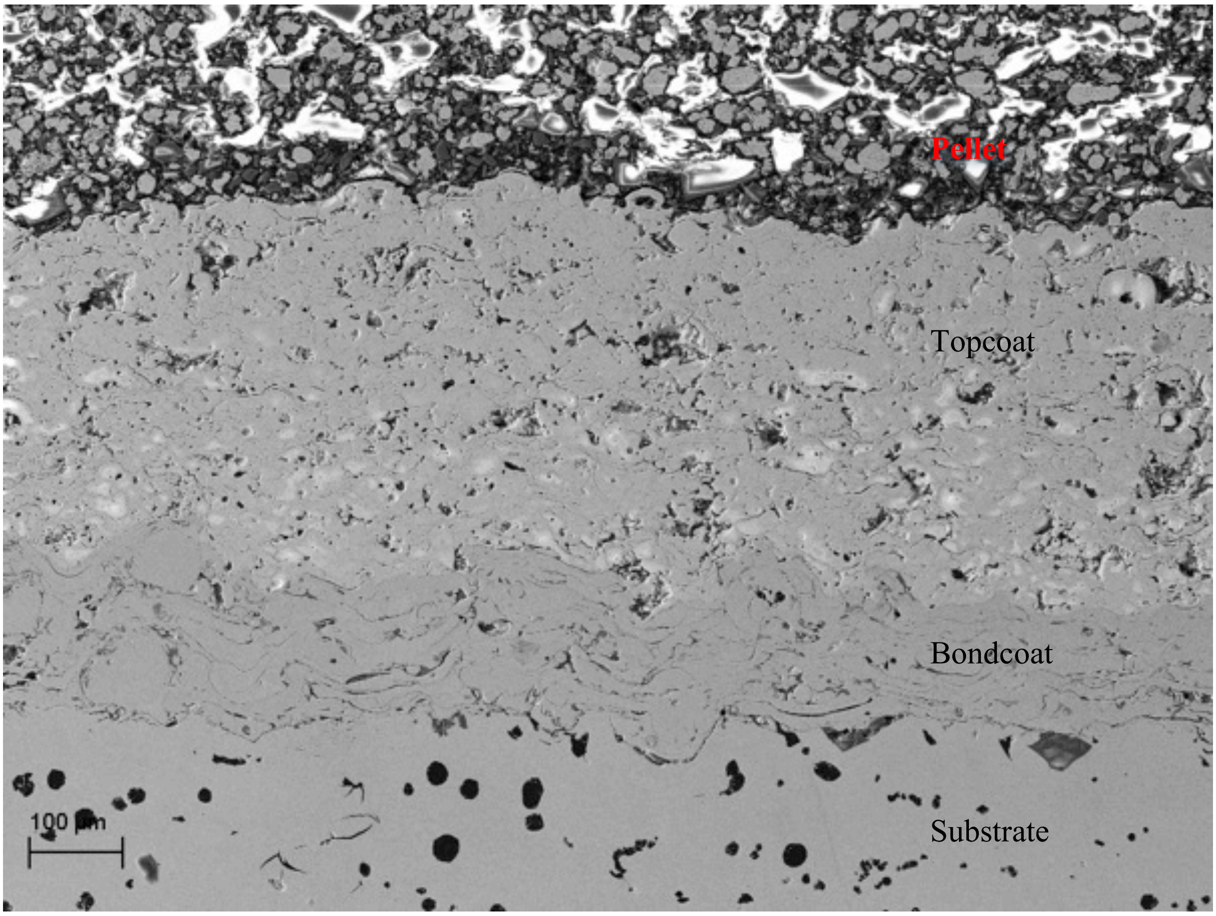

Figure 2 View of typical APS TBC system structure before thermal cycling

2.1 Exhaust manifold loads

When coating the manifold there are some critical aspects that need to be taken into account. Due to the position of the manifold in the exhaust system, right before the turbo charger, Spallation cannot be allowed since even the smallest "chip" can damage and destroy the turbo. There are many factors that affect the manifold in terms of large stress-introducing processes, for example, temperature cycling, vibrations, exhaust flow and pressure. The maximum temperature that the manifold is being subjected to is 760^{o}C due to the hot exhaust-gas flow. The material itself does not reach the above stated temperature but close to it, approximately 755^{o}C. The temperature cycling introduces thermal mismatch stresses that can damage the TBC and cause spallation [7]. The exhausts also generate a pressure change, where the pressure peaks reaches levels up to 14bars. The pressure increase does not only introduce stresses in the top coat but can also increase the thermal conductivity of the system [8], making its desired thermal shielding properties decrease. The flow of exhausts varies over the manifold with the number of cylinders being passed. In the extreme case, the gas flow may reach values of 40kg/min in a high-power diesel engine. This amount of flow presents an erosive damage mode that in time will degenerate the TBC coating and cause spallation [7]. The last main contributing factor to TBC failure in exhaust manifold is the vibrations. Engine-introduced vibrations can reach amplitude levels of up to 20g. The reports on TBC subjected to vibrations (HCF) have shown that TBC has a damping effect generating longer lifetimes of the component [9]. However the damping is an effect of energy loss due to micro crack formation in the TBC topcoat, generating initiation points for spallation**.**

2.2 Substrate materials

The materials described below are all common materials used for the exhaust manifold. Depending on the exhaust manifolds design and operating temperature, the material of choice can be either a ferritic cast iron or an austenitic cast iron / cast stainless steel. A widely used material for diesel engines is the ferritic ductile cast iron SiMo51 [10]. But due to this alloys temperature limitations austenitic materials, D5S [11] and HK30 [13], are more commonly used in Gasoline engines due to higher strength at elevated temperature. The three materials, SiMo51, D5S and HK30 will be covered in more detail below.

2.2.1 SiMo51

The ferritic cast iron SiMo51 is a ductile alloy consisting of Silicon and Molybdenum. The chemical composition can be altered but usually it consists of between 4-5% of Si and around 1% of Mo together with other alloying elements [10]. Spheroidal graphite and M_6C carbides are present to strengthen the ferritic matrix, where the Mo is added to form these M_6C carbides. Si is added to increase the oxidation resistance by the formation of protective SiO_2 but also as strengtheners [13]. At temperatures above 750^oC the protective effect of Si becomes limited and SiMo51 shows a decrease in both oxidation- and fatigue resistance. [13].

2.2.2 D5S

The austenitic cast iron D5S has the same spheroidal graphite as SiMo51 and classifies as a ductile Ni-resist cast iron [13]. The austenitic matrix possessed by D5S generates a higher strength, compared to the ferritic SiMo51. Making D5S more suited for higher temperatures [11]. The maximum prolonged temperature for which D5S is a suitable candidate is 850^oC [13] but the corrosion resistance has shown to be stable up to 1050^oC. The reason for these high temperature properties can be understood by the high content of Nickel. D5S consists of 34% to 37% austenitic stabilizing Nickel, generating this high temperature strength [13]. The nickel content also generates a lower thermal expansion compared to SiMo51 [13]

2.2.3 HK30

HK30 is an austenitic cast stainless steel classified as high temperature resistance. It is commonly used for structural applications subjected to both corrosive environments as well as for temperatures up to 1150^oC [13]. Making HK30 suitable for high performance gasoline engine manifolds [13]. It contains a lower nickel content compared to D5S but has a Cr content between 23-27% [13] generating a high temperature oxidation- and creep resistance. HK30 do on the other hand form brittle sigma phase (iron - chromium) up to temperatures around 800^oC. With prolonged time at this temperature range the sigma phase growth results in a Cr and Si depletion and with that a reduction in high temperature properties [14].

2.3 Coating processes

The two most widely used coating processes for TBC are plasma spraying, PS, and electron beam assisted physical vapour deposition, EB-PVD [15]. However, these two have one common drawback based on their main principle. Both of these processes are classified as what is known as “line of sight processes”[6], meaning that there has to be an open path between the source and the intended coating area of the substrate. For this reason the coating is somewhat limited to simple geometries and present a difficulty in coating the inside of a body without any modifications of the substrate or expensive automation processes [15]. Nevertheless, these two are, as mentioned earlier, widely used for coatings and are for some geometry extremely effective in both quality and cost efficiency [6]. For complex geometries, such as the insides of exhaust manifolds, other process methods need to be evaluated and there are some that show great possibilities in the field of “no line of sight”-processes, for example, sol gel- and slurry coating [16,17]. The two mainly used processes and some processes that in literature have shown great possibilities will be discussed below.

2.3.1 Plasma-Spraying

The process of plasma spraying is often carried out under atmospheric pressure where powder of the desired coating material is fed into a high temperature source and allowed to melt. A stream of gas transports the melted particle to the desired surface at a high velocity [15]. A schematic view can be seen in Fig.3.

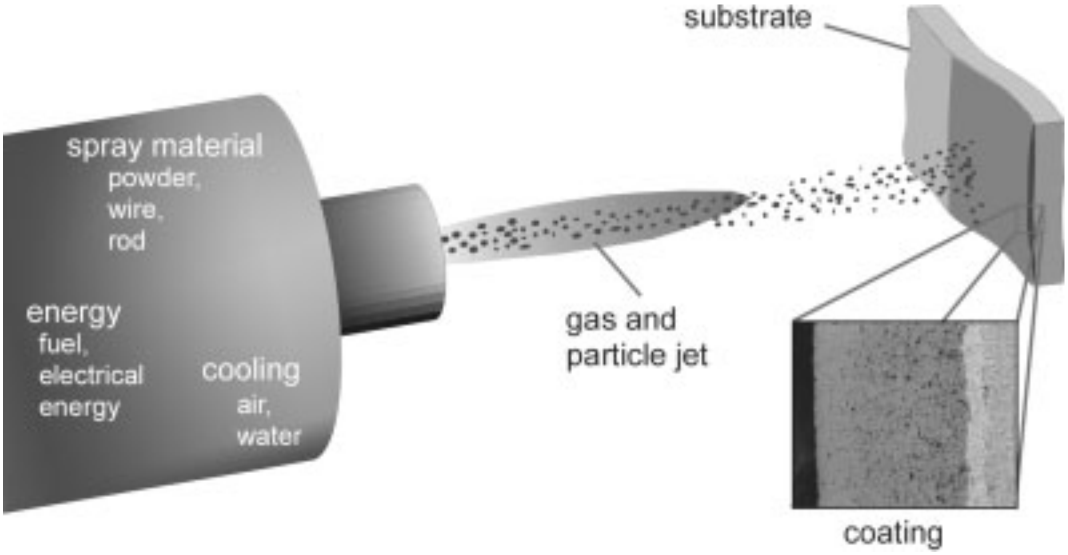

Figure 3 Schematic view of the APS process [15]

Coatings applied by plasma spraying show a very distinct structure consisting of a laminar structure with high porosity, partially or completely unmelted particles and micro cracks [15]. These characteristics are in many ways a product of the rapid cooling of the so-called splats, which are melted particles that deform on the impact with the substrate. The laminar structure grows normal to the substrate surface, with pores that can be found as distances between the splats [6]. This porous structure, in combination with the presence of micro cracks, result in a structure that exhibit low thermal conductivity but only moderate strain tolerance compared to EB-PVD [15]. The are several reasons for the use of the APS process, its low cost, no requirement of protective atmosphere rendering the possibility to coat large substrate, high deposition rate and has the ability to apply thick coatings at low cost [15]. The applicable thickness is theoretically up to 1000µm but with increased thickness the coating becomes more sensitive to the mismatch stresses [6]. Applications of coatings using APS internally of complex geometries with small internal dimensions the plasma gun acts as a limitation in terms of the size where APS is applicable [6].

2.3.2EB-PVD

In electron beam-assisted physical vapour deposition, low-pressure conditions are required. Air is evacuated from the chamber and an electron beam is focused on a target of the intended ceramic coating material. The focused electron beam melts the target material that is later evaporated. Above the target material the component intended as substrate is placed to be able to “receive” the evaporated ceramics. When the evaporated atom interacts with the substrate it solidifies and a diffusion driven process creates the coating [15]. A schematic view of the process can be seen in Fig.4.

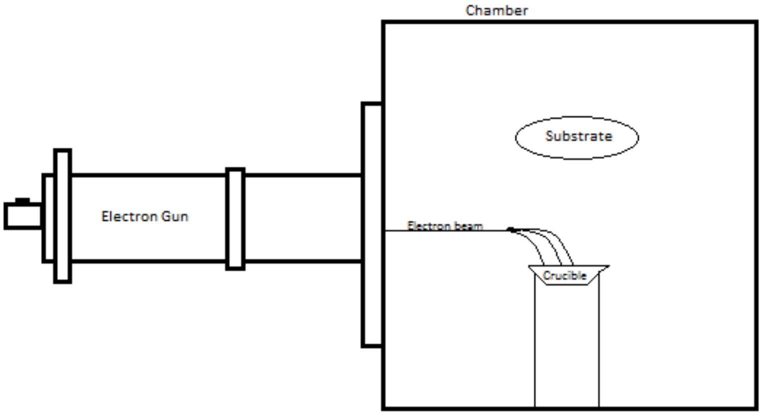

Figure 4 schematic view of EB-PVD process

Electron beam assisted physical vapour deposition, as well as APS, shows a very distinct structure of the deposited coating. The process generates a columnar structure growing perpendicular to the substrate surface, were the porosity arises from the distance between these columns [18]. This structure is far less sensitive to strain than the laminar structure generated by PS, but exhibit a higher thermal conductivity [18]. The higher thermal conductivity is related to both the columnar structure but also the thinner coatings often applied using PVD. The PVD process renders a coating thickness of 1-10µm per layer, but do posses the ability to apply multilayer coatings [18]. The distance between the individual columns in the structure requires a bondcoat well composed for the coating. The bondcoat needs to function as a combiner of the individual columns to avoid spallation, not only to increase the adherence between coating and substrate [6].

2.3.3 Suspension Plasma Spraying

Suspension Plasma Spray (SPS) is a form of the conventional plasma spray that has been developed for first and foremost application of nanosized particles (>5µm) in an effective way. The process involves the same steps, as the conventional APS, were the difference could be found in the feedstock of the powder. Instead of the conventional case were powder is fed into the plasma in its dry state, a carrier liquid is used [19]. The use of a liquid generates the possibility to use smaller particles (>5µm), without their tendency to aggregate as in the case of APS [19]. The carrier liquid usually consists of an alcohol and a dispersion medium that generate a uniform and homogeneous coating using nanosized particles [19]

The use of a liquid instead of dry powder generates a temperature drop in the plasma due to the energy needed to evaporate the carrier [19]. The effect is that the outer most plasma, closest to the feedstock, provides lower energy to the particles compared to centre plasma [20]. This generates an inhomogeneous coating where areas will contain more, or less, unmelted particles [20]. Compared to APS the SPS process requires a shortened working distance due to the small size particles [20]. The smaller sized particles than in i.e. APS are more affected by the heat exchange to the environment, rendering the need to shorten their exposure to the room temperature air, to maintain their melted state [20]. The shortened working distance also increases the influence of the plasma temperature on the substrate, generating a higher substrate temperature [20].

2.3.4 Directed Vapour Deposition (DVD)

Another process involving all the same foundation, as EB-PVD, is Directed vapour deposition, DVD [6]. The difference between the two is that instead of letting the vapour spontaneously reach the substrate by own means the vapour is instead transported to the substrate using a carrier gas [15]. By this small modification of the PVD process, the line of sight process can now be classified as no line of sight. Since the process is diffusion driven the carrier gas could be directed i.e. inside a pipe creating a much alike structure as EB-PVD on the inside of the pipe instead of the outside [21]. This process present the opportunity to create a fine and homogeneous coating internally of complex geometries, but require low-pressure atmosphere, rendering limitations in terms of substrate size. The process also produces thickness similar to PVD but does, to days date, not possess the possibility to create homogeneous multilayer coatings to increase the thickness [21]. The process can be applied using “soft” vacuum, but the produced coating becomes more or less contaminated from the surroundings, making it hard to control the desired properties [15]. A simplified view of the process can be seen in Fig.5.

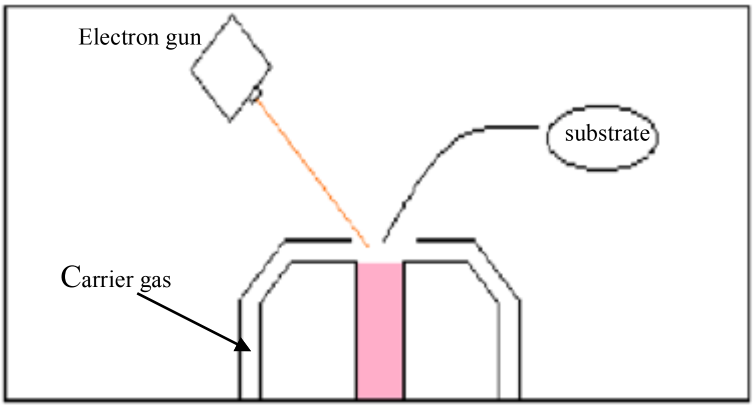

Figure 5 schematic view of the DVD process were a gas flow transports the atoms to its intended substrate.

2.3.5 Slurry coating process

A process that has been used to produce porous ceramic implants for the human body is the slurry coating process [17]. This process can be divided into slurry plasma spray and slurry dipping coating [17]. The slurry spray process has been used to apply thermal barrier coatings as a substitute for pure powder in the conventional plasma spray while the dipping process has been more guided towards implants. Recently, researchers have found other combinations of binders that now make it possible to coat a complex substrate by dipping it into the slurry [17]. One such binder has been PVA, which is commonly used to produce carbon nano wires. The slurry dipping process is a simple and cost-effective process where no expensive tools are involved. The process involves a very fine powder of the intended coating material that is mixed together with a dispersant and a binder [17]. The component is later dipped into the mix and then left to dry. After the drying process the entire product is sintered to achieve a durable, jet porous, ceramic. The porosity is generated when the polymeric binder is burnt off during the sintering process at a higher rate than the densification rate of the ceramic material [17]. The slurry dipping process can also by simple means control the resulting thickness of the coating by applying an activator on the desired coating areas where geometries generates a problem. The process also makes it possible, if the substrate is prepared with a wax layer, to reduce the effect that the entire component is coated, due to poor adhesion of PVA to the wax layer. The substrate material used for this process is limited to materials with higher phase transition temperatures then the sintering temperature of the intended coating material [17]. Materials like Mullite, which is a metallic oxide-based ceramic, has been successfully produced using this process but requires a substrate capable of short operation times at temperatures above 1400^{o}C [22].

2.3.6 Sol-gel process

Sol-gel dip coating is based on 4 different steps, which characterizes the entire process, the substrate is dipped into a fluid known as sol and then removed from the bath in a very controlled manner. During the emerge of the substrate, excess fluid is drained as well as a stage of solvent being evaporated. The substrate is held in air to allow condensation reactions to occur. The component is later heat treated between 400-1000^{o}C, depending on coating material, to process the stable matrix and remove unwanted organic components [16]. The process before heating can be seen in figure 6.

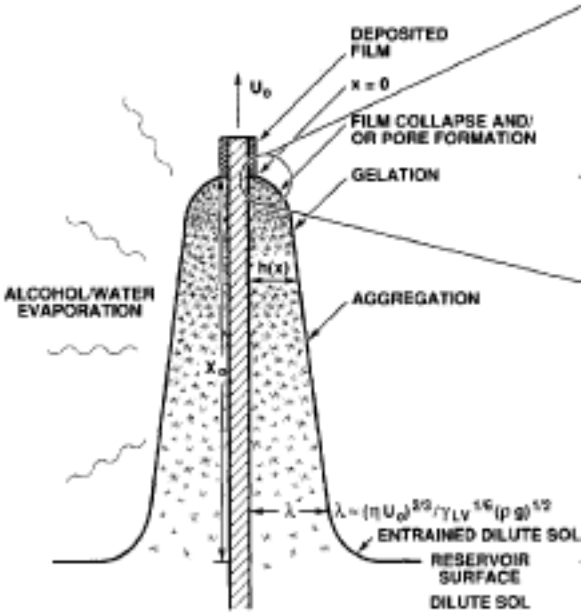

Figure 6 View of the Sol-gel coating process [16]

The reason for the interest in sol-gel coatings is the factor that it is a non-directional deposition technique. Generating a possible technique to coat complex geometries as well as multilayer coating procedures of the geometries [16]. Enabling the development of coatings with different density and properties at different levels [16] the simple process makes the method in terms of cost close to APS to achieve thick enough TBC [16]. Sol-gel has also shown a good adherence to hydroxyl groups. These groups are present at a pre-oxidized substrate surface which have shown to generate good adherence to Sol-gel coatings without the need of applied bondcoat [23]

Sol gel is classified as a wet-chemical process allowing for production of ceramic materials through a polymerization process resulting in a rigid network gel [16]. The process follows a simple recipe that involves an alkoxides that in the presence of water undergoes hydrolysis. After this reaction, condensation takes place that render a desired polymer chain. I.e. in the formation of 8YSZ, Zirconium tetrabutoxide undergoes hydrolysis and the following condensation renders a Zr-O-Zr polymeric chain. The polymer chain is then allowed to undergo pyrolysis that forms the ceramic zirconia (ZrO2). To achieve the yttria stabilization, yttrium acetate is applied as an aqueous solution to the alkoxide becoming intimately mixed. Yttrium acetate does not undergo hydrolysis or condensation, but the intimately mixing traps the acetate inside the structure as the solution gels [36]. The substrate is dipped into the mixture before the condensation and heat treatment and then the entire component is placed in an furnace for pyrolysis. The temperature of the pyrolysis is dependent on the decomposition temperature of organometallic compounds, 450°C in the case of zirconium [23]. The low temperatures associated with Sol-Gel make it applicable to metallic substrate without risking phase transition. Depending on the desired structure the coating can undergo further heat treatments, sintering or the process can be repeated to generate an even thicker layer [23]. The fact that Sol-gel is chemically driven derives the need for a clean environment and contaminant free atmosphere to produce defect free coatings [24].

The most important controllable parameter affecting the durability and quality of the Sol-gel coating is the withdrawal speed of the substrate from the gel [16,23,24]. This parameter affects the porosity, uniformity and thickness of the coating and needs to be closely monitored [16]. The withdrawal speed parameter is set by the evaporation rate and concentration of gel at the coating surface [23]. The viscosity of the gel also affects the withdrawal speed. Sol-gel requires a "still liquid" where no waves or splashes take place, which locally increases the concentration of gel at the substrate [23]. A local increase in Sol-Gel concentration generates an uneven thickness that during the following heat treatment is more affected by induces stresses and lowering the expected lifetime [24].

The two methods used today, APS and EB-PVD both have their limitations in form of the fundamental idea behind them. They are both classified as "Line of sight" processes, which corresponds to that they cannot be used to coat complex geometries or for internal coatings, since the nozzle needs to be in full sight of the position of the substrate that is being coated. This limitation has led to the development of so called No line of sight NLOS processes that can be used to coat complex geometries and also internally. Some processes have shown greater possibilities in this field in form of coating thickness and the ability to control it, complexity and also economically since some processes have shown to reduce the costs for the coating process compared to today cheapest APS. There is another NLOS process, which should be mentioned the CVD method that can also be used to apply the TBC coating. This process will not be covered due to that the resulting coating usually is far too dense, which in this case is undesired and often far too thin for application use.

2.4 Coating general microstructures

The properties of the different TBCs used today are highly correlated to the characteristic microstructure each of the deposition methods generate. This section will cover the structures generated by the deposition methods covered in section 2.3.

2.4.1 EB-PVD

In EB-PVD, the deposited topcoat microstructure is characterised by columnar grains, growing perpendicular to the substrate forming wide spaces between them with multi-scaled porosity [6]. Due to the diffusion driven process EB-PVD generates a far denser microstructure in terms of the bulk material compared to APS. The porosity exhibited by EB-PVD coatings is the distance between the individual columns [25]. This structure results in a strain tolerant coating associated with the columns that have the ability to move relative each other. But with a higher thermal conductivity due to the low porosity levels compared to APS. The characteristic microstructure can be seen in Fig.7.

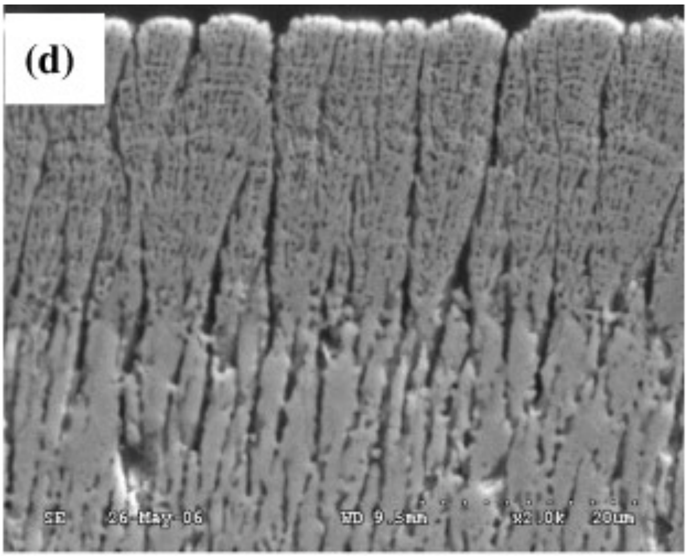

Figure 7 SEM picture showing the characteristic columnar PVD microstructure [25]

2.4.2 APS

The APS microstructure, compared to EB-PVD, is instead laminar where the grains grow parallel to the substrate [6]. When the melted particles interact with the substrate they plastically deform and flatten out, creating “splats” upon solidification [6]. These deformed particles form the laminar structure associated with APS. The rapid cooling of the particles upon impact with the substrate results in voids as distances between individual splats, generating this highly porous structure [26]. The high porosity renders a low thermal conductivity [26], but this laminar structure generates a lower strain tolerance then EB-PVD [6]. The strain tolerance is also affected by the rapid cooling associated with APS that results in a microstructure containing a high volume fraction of micro cracks [6]. A typical microstructure can be seen in figure 8.

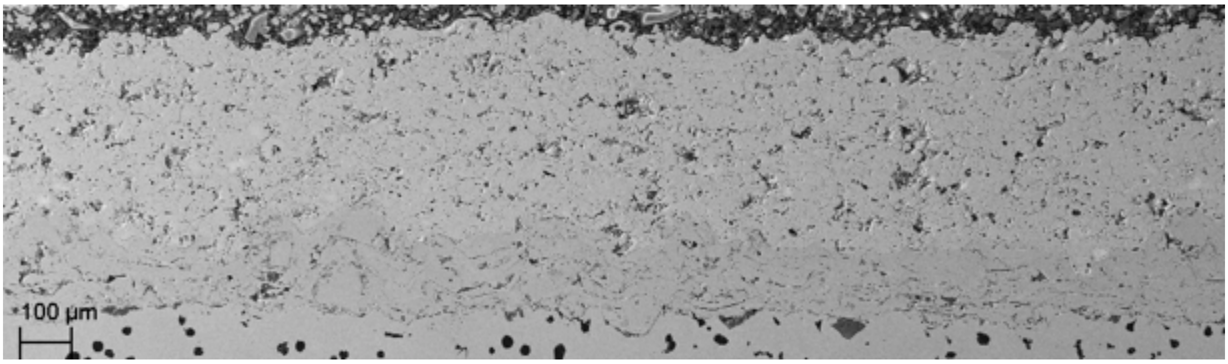

Figure 8 Typical APS microstructure

2.4.3 SPS

The SPS renders a microstructure that can be seen to combine the positive attributes associated with APS and EB-PVD. As can be seen in Fig.9 the structure shows vertical cracks rendering good strain compliance, much like the columnar structure associated with EB-PVD [19]. The different layers associated with plasma spray also generate bands of porosity due to the different passing's that correlates to distances between "nanosplats" [19]. This combination of vertical cracks and finely dispersed pores generates an increase in strain compliance of 300% compared to APS while maintaining a thermal conductivity with only a minor increase from that of APS [27]. Recent developments within SPS have been to increase the porosity to further decrease the thermal conductivity. This has been done by introducing a new material into the suspension, polymers [19]. The polymers are burnt off during the coating process generating an increase in the porosity, with associated decrease in thermal conductivity and increase in elasticity, rendering an even more durable coating [19].

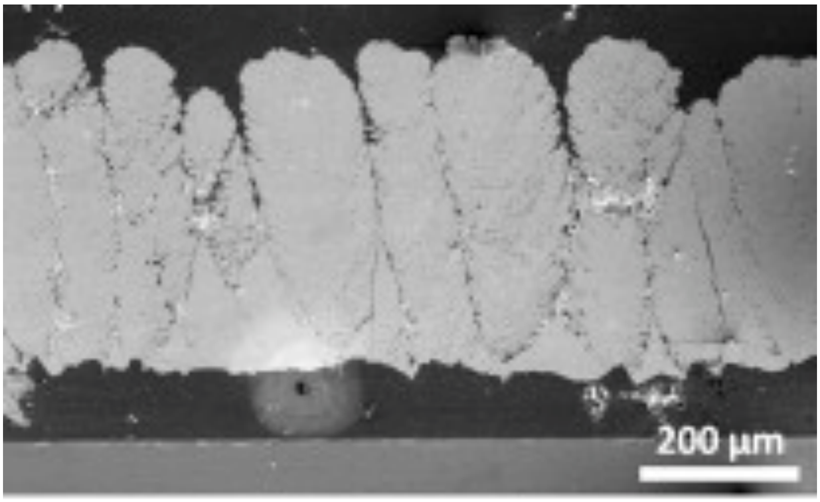

Figure 9 SPS microstructure [27]

Research has shown that like EB-PVD, this columnar structure prompts a good adherence to uneven surfaces due to the vertical instead of parallel growth. This, together with low incident angle dependence and that APS setup can be used, generates a durable jet low cost coating process. [27] The microstructure is, like in the other processes, highly dependent on the working distance. If the working distance is kept short the structure generated is of a denser, columnar structure while longer distance generates a more porous structure [19].

2.4.4 Sol-Gel

Sol gel applied coatings has shown a structure much like the one achieved using the APS process. The microstructure (see Fig. 10 for schematic view) consists of a large fraction of micro cracks, originating from the heat treatment involved not rapid cooling [16], together with a high level of porosity controllable by the heat treatment temperature [17]. Rendering the same behaviour of higher energy needed to drive large cracks through the coating and low thermal conductivity [6]. The thermal cyclic resistance of the Sol gel coatings has shown far less than for the APS coatings due to initial defects originating from the coating procedure [16]. These defects prompt the spallation of the coating due to the process called ratcheting [17]. The parameters that have shown to control the achieved microstructure, size and opacity of fractal precursors, are the rate between condensation and evaporation, capillary pressure and the substrate withdraw speed [16]. With these parameters controlled, the resulting microstructure can be modified in terms of pore size, surface area, pore volume and refractive index. The thickness and porosity are strictly related to the substrate withdrawal speed [16].

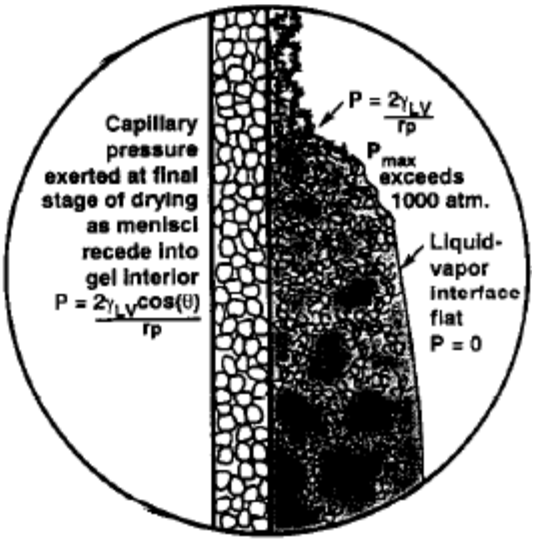

Figure 10 Schematic view of microstructure achieved using Sol-gel dipping process. [16]

2.5 Material properties

In this section material and coating properties that control the durability and effectiveness of a thermal barrier coating will be covered.

2.5.1 Thermal conductivity

In TBCs the thermal conductivity of the system can be seen as a combination of two main controlling factors; the radiation component due to photons and the lattice wave component based on phonons [28]. The lattice waves can be seen as vibration waves that propagate through the lattice due to a displacement from the equilibrium position of atoms [29]. The energy of these waves in an ideal solid without any type of defect would remain constant and hence due to non-thermal equilibrium of the waves, a high thermal conductivity would be achieved [30]. In reality, these ideal solids never exist and due to lattice defects and grain boundaries, lattice waves are scattered upon interaction resulting in thermal equilibrium limiting the thermal conductivity through the material [28].

The radiation component that is generated due to photons is a large contributing factor in the thermal conductivity at high temperatures. Literature has shown that dense materials act as black bodies, absorbing much of the radiated heat. If the amount of defects in the material is increased, the radiation component decreases due to reflection of the photons [28]. In Fig. 11, the coefficient of thermal conductivity at room temperature for some common TBCs is presented. [6].

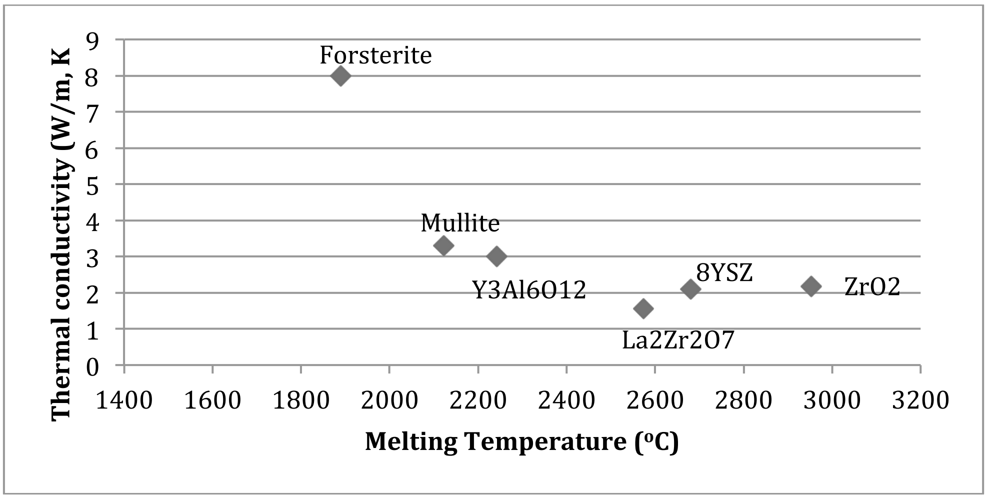

Figure 11 Thermal conductivity at room temperature of selected TBC material [6].

The thermal conductivity can be understood using two simple equations, one that depends on the transportation of heat by phonon transfer through the solid, Eq. 1[31].

$$K = \frac{1}{3} C_v * v * l \qquad (1)$$

Where C_v is the specific heat of the solid, ν is the speed of sound through the solid and l is the mean free path. The mean free path in this equation can be altered to lower the thermal conductivity by introducing lattice defects or porosities into the system that scatter the phonons [31]. The influence of the porosity on the thermal conductivity can be seen by reviewing equation 2 [32].

$$K=\alpha * C_p * \rho \qquad (2)$$

Where instead of the mean free path used in Eq. 1,the density ρ, is used together with the thermal diffusivity, α, and specific heat C_p. When reviewing the specific heat of a solid, C_v and C_p can be assumed the same [31]. As Eq. 2 shows, an increase in density, as in densification during sintering increases the thermal conductivity of the solid, resulting in a non-thermally stable TBC that loses its shielding properties at higher temperatures [31].

The material parameter specific heat, defined as the amount of thermal energy the material can absorb (J/K,mol), plays a large role in the thermal conductivity of the material [31]. The behaviour of the specific heat can be divided into two stages where in the initial stage the specific heat increases with increase temperature [31]. In this stage the specific heat increases due the vibrations of the individual unit cell, vibrations that increases with temperature [31] At a certain temperature the wavelength of the phonons exceeds that of the unit cell, called the Debye temperature. Rendering the specific heat to be independent of the individual vibrations and the specific heat stabilizes [31].

2.5.2 Thermal expansion coefficient

One of the key aspects when designing and choosing a TBC system, in terms of topcoat and bondcoat is the thermal expansion of the individual components [6]. To generate a durable and effective TBC, the thermal expansions of the components should match each other, reducing the thermal stresses induced during the cycling [6]. If the difference in thermal expansion between the topcoat and the underlying material is large enough the generated mismatch stresses will results in failure of the TBC system [8]. The thermal expansion/ contraction depends on the coefficient of thermal expansion and the difference in temperature affecting the different layers in the system [6] Fig.12. Shows the linear CTE of some common topcoat materials together with the common substrates for exhaust components and the NiCrAlY bondcoat [6].

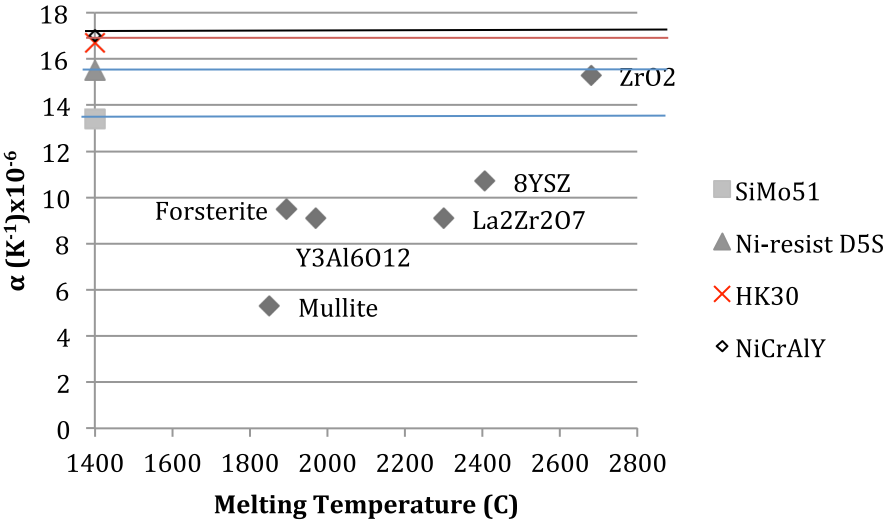

Figure 12 Linear CTE of selected TBC materials [6]

2.5.3 Density

As Eq. 2 shows the thermal conductivity of a coating decreases with a decrease in density [31]. The desired low thermal conductivity of a TBC can be achieved by increasing the porosity of the coating [28]. A high amount of porosity lowers the materials density and increases the amount of oxygen present in the coating, oxygen that has a very low thermal conductivity [33]. Another property that is affected by the porosity is the Young’s modulus. For a topcoat that has a much lower thermal expansion than the metallic substrate, a low Young’s modulus is preferred to be able to “follow” the substrate material and better deal with the thermal mismatch stresses, generating a more durable coating with longer lifetime. [34] Depending on the operational temperatures affecting the component, the level of porosity and density of the coating can, however, change due to sintering problems. A high porosity as a starting structure is more likely to undergo sintering which in the long run means that the density will change and undergo densification creating a far denser structure than the initial microstructure [33]. Consequently, with the densification, the Young’s modulus, hardness, fracture toughness and thermal conductivity will change [34]. Siebert et al.[35] showed that at temperatures around 1000°C, the increase in Young’s modulus of high porosity zirconia topcoats were close to 100% over a time period of 100h.

2.6 Materials for TBC Topcoats

Materials intended for use as a TBC coating should exhibit and fulfil a range of properties and requirements to be classified as suitable for the application [6]. The main purpose for a TBC system is to decrease the thermal exchange to the underlying material generating the need of a low thermal conductivity [6]. To be suitable as a TBC the system should possess high thermal stability where no phase transformations occur within the operating temperatures, high chemical stability, low density and low sintering rate [6]. Aside from the individual properties the system needs to interact well in terms of thermal expansion and adherence [6]. This section covers some materials that satisfy many of the above given properties.

2.6.1 Mullite

Mullite has shown to be a good material for use as thermal barrier coating since it has low thermal conductivity, high resistance towards corrosive and oxidative environments and thermal stability [22]. For the use in engines, where spallation debris could result in failure of other components, the high resistance to crack propagation should also be mentioned. The decrease in crack propagation is due to the extremely low creep rate of the material resulting in far less stress relaxation in the topcoat [22]. The rapid cooling associated with plasma spray results in high percentage of amorphous phase of Mullite in the applied coating. When thermal cycling reaches temperature between 750-1000°C the amorphous phase begins to crystallize and the resulting volume contraction that can generate debonding or crack initiation [36]. Mullite also exhibits a low thermal expansion; much lower that most of the substrate materials, resulting in large mismatch stresses between topcoat and substrate that lowers the expected lifetime due to that it prompts delamination [36]. Mullite exhibits a stable thermal conductivity up to 1500°C, correlating to the phase stability, seen in Fig.13. Highly porous Mullite has, up to 1500°C, shown only moderate densification with a density increase of only 2% after 100h [36]. The thermal conductivity in Mullite, shows according to tabulated values, a strong dependency on the temperature due to the high Debye temperature [37]. As the temperature increases, the thermal conductivity increasing, making the substrate material affected at higher temperatures [37].

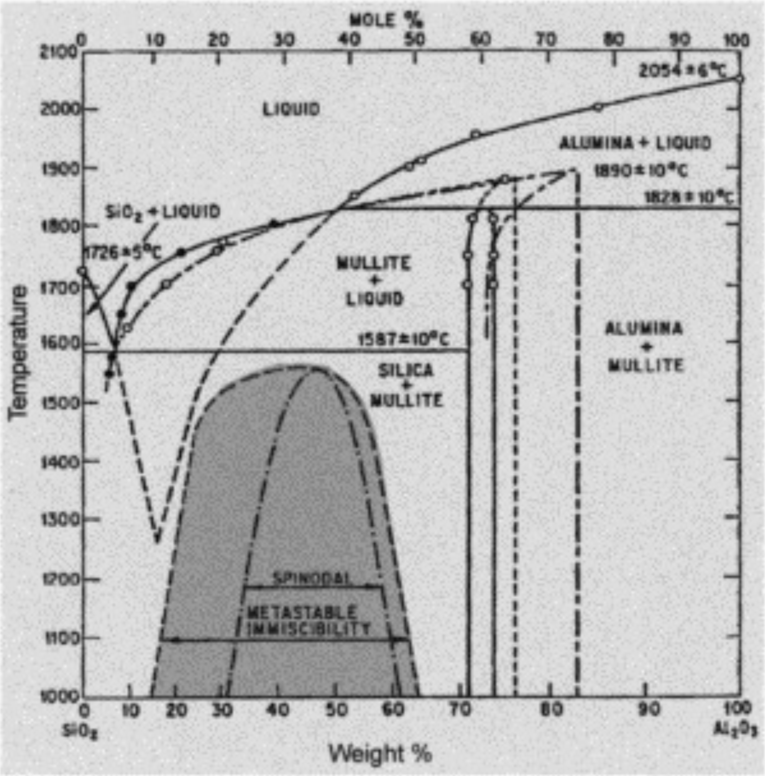

Figure 13 phase diagram showing the evolution of Mullite [38]

2.6.2 Zirconate

Zirconia based thermal barrier coatings is today the far most understood and commercially used TBC available. Pure Zirconia has very limited operating conditions due to its tendency upon cooling to transform from a tetragonal phase to a monoclinic form at fairly low temperatures (~670^{o}C) [39]. This phase transformation results in a volume expansion of the material that in many cases leads to failure in catastrophic manner. The structural problem a side, pure zirconia possesses properties that make it an interesting material for TBC materials, low thermal conductivity, high melting point, high thermal expansion and chemical inertness [6]. One solution to the phase transformation has been to stabilize the zirconia using Y_2O_3. [39] By introducing 7- 8% Y_2O_3 into zirconia, a material what is commonly known as 8YSZ, 8% yttria stabilized zirconia is created. In YSZ the main properties of zirconia remains at levels suitable for TBC including that no phase transformation occurs at temperatures below ~1200^{o}C [6]. One of the main drawbacks regarding YSZ is its low resistance towards hot corrosion [40]. Degradation of the YSZ in exhaust applications has much to do with the stabilizer Y_2O_3 reacting with S, Na and V that are present in different kind of fuels. 8YSZ has shown very sensitive towards impurities in form of SiO_2. SiO_2 segregates at the grain boundaries leading to changes in grain size, with the effect of increased creep rate. The depletion of Y_2O_3 leads to localized degradation and polycrystal superplasticity of ZrO_2 resulting in increased sintering rate [41]. The stress relaxation of the top coating generates a problem, the compressive stresses present in the coating generates a good barrier for crack propagation and at elevated temperatures this effect degenerates and can result in spallation of the top coat [42]. The 8YSZ is not fully stabilized, the cubic phase can at higher temperatures generate a crystallographic change in structure due to the presence of the metastable t’-phase that can be seen in Fig. 14. This tetragonal phase has a tendency to cluster [43], which leads to localized stress fields and an inhomogeneous material. This problem can be solved with annealing, especially in sol gels or introduction of nanosized YSZ [43].

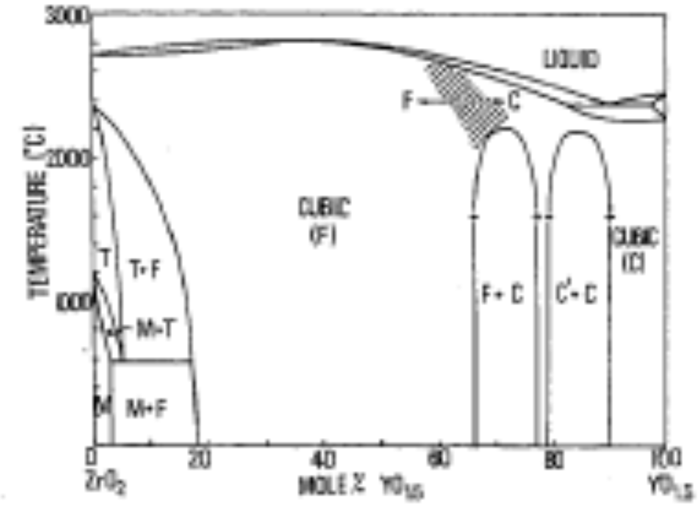

Figure 14 Phase evolution in Yttria- Zirconia system [39]

2.6.3 $La_2Zr_2O_7$

As a member of the pyrochlore type zirconium oxide $La_2Zr_2O_7$ shows low thermal conductivity, high melting point, high thermal expansion and high stability which have made it interesting as TBC topcoat [44]. The phase stability of the $La_2Zr_2O_7$ has been proven up to 1400°C, but if $La_2Zr_2O_7$ is applied together with a NiCrAlY bond coat the Al content can react with the La_2O_3 creating a degradation of the coating even at temperatures below 1000°C [45]. If comparing the $La_2Zr_2O_7$ to YSZ, the former exhibits a lower thermal expansion, which in TBC application would generate larger stresses due to mismatch with the substrate material [44]. One solution to the low thermal expansion has been to use $La_2Zr_2O_7$-graded YSZ [46], which increases the thermal expansion but allows $La_2Zr_2O_7$ to maintain its cubic pyrochlore structure [46].

2.6.4 Forsterite

One material that has been ruled out for TBC coatings in turbo engines due to the low service temperature (1000°C) is Forsterite [1]. Forsterite can be classified as an Mg rich olivine structure having a high melting point and shows no phase transformations below 1890°C [47]. Forsterite has as a material a quite larger, for the material class, thermal expansion coefficient, which correlates better with many metal substrates resulting in lower mismatch stresses [48]. It has also been shown that the thermal conductivity of the material is almost as low as for Mullite [49]. The reason for the low temperature under which Forsterite can operate is the tendency for Magnesium to diffuse at grain boundaries generating a diffusion driven creep deformation [50]. The low service temperature is not the only thing resulting in the limited use of Forsterite. The structural strength of Forsterite has shown to be far less than for the 8YSZ, in particular when talking about fracture toughness. The fracture toughness of Forsterite is five times as lower than for 8YSZ [51]. This generates a lager tendency for the topcoat to spall of during thermal cycling.

2.6.5 Nanostructure YSZ

Research is focused on refining the properties of the yttria stabilized zircon by applying the coating with nanostructured YSZ (NYSZ) With the objective to refine the properties of the otherwise commercial "common" YSZ [6]. As the nanostructured YSZ possesses a denser microstructure, the oxidation rate through the topcoat to the bondcoat is reduced, thus generating a more stable coating with higher resistance to spallation [52]. The thermal expansion of the nanostructured YSZ shows no significant change, despite the microstructure refinement, which has to do with that the bulk material in itself is the same. Due to the finer grain size (approx. 1μm) that prompts crack deflection at grain boundaries, the topcoat is more reluctant for cracks and spallation [53]. The nanostructure also exhibits a lower Young's modulus and influence of thermal stresses, generating a more stable performance during thermal cycling [53].

NYSZ has been developed to increase the stability of YSZ for first and foremost thin TBCs. NYSZ has generated an increase in maximum operating temperature compared to conventional YSZ. The decrease in grain size generates a denser microstructure which decreases the oxidation transfer through the topcoat making the nanostructure YSZ less affected by hot corrosion [53]. According to literature the microstructure of the NYSZ is denser than the conventional YSZ but exhibits a lower thermal diffusivity [53]. When applying a heat treatment to them both, it is clear that when temperatures reaches ~1200°C some sintering effects can be seen as the thermal diffusivity for both NYSZ and YSZ follow the same gradient increase. The difference can be seen after approximately 1hour when instead of an increase in thermal diffusivity, with decrease rate, that YSZ exhibits; the NYSZ is seen to stabilize and become more or less stable [54]. To understand this difference one can compare the phenomena showed when applied using APS. During the first hour both exhibit self-healing of the process introduced porosity due to sintering [55]. The difference that takes place is that when NYSZ stabilizes itself. This is the effect of the different sintering rate of the matrix and the "nanozones" [55]. The nanozones exhibit a higher sintering rate than the matrix, making the material more porous [55]. The decrease in volume of the nanozones is not in phase with the matrix, creating voids between them, making the porosity to increase and thereby more or less stabilize the diffusivity [55] The porosity and its stabilization can also be used to evaluate the Young's modulus, by applying the equation $E=\rho v^2$, where v is the velocity of traveling waves in the lattice. It becomes clear that the young's modulus decreases with decreased density [56]. For materials used as thermal barriers, a lower young's modulus is preferred due to the increase in strain compliance due to that the topcoat follows the bondcoat [55].

2.7 Failure modes during thermal cycling

The most common failure mode of TBCs is spallation of the topcoat, which is associated with the effect of crack formation in the topcoat close to the interface [7]. The general explanation for this behaviour is formation of an oxide layer at the interface between bondcoat and topcoat together with mismatch in thermal expansion between the topcoat and bondcoat or topcoat and substrate, which generates internal stresses that buckles, due to strain, the interface creating crack initiation points [57].

The environment that TBC coatings usually operate in can be classified from how they are being subjected to heat. For applications in diesel engines, the types vary depending on the location, where combustion chamber can be classified as thermal chock and the exhaust application thermal cycling. Naturally, these different heating environments require that the TBC coatings for the different environments have different physical and chemical properties to generate a sustainable coating [57]. Since this thesis focuses on TBC in exhaust applications, the properties that generate a sustainable coating during thermal cycling will be investigated.

When subjected to thermal cycling, many different processes are active and contribute to degradation and final failure of the TBC coating. The main reason for TBC failure are related to stresses, governing from mismatch in thermal expansion, TGO growth, bondcoat creep, depletion of Al present in the bondcoat, sintering and densification, delamination, buckling and cracks [58]. These failure mechanisms are highly dependent on the system, application and environment, making it difficult to pinpoint an exact failure mechanism. Fig. 15 shows a schematic view of activated failure mechanisms in a TBC system subjected to thermal cycling.

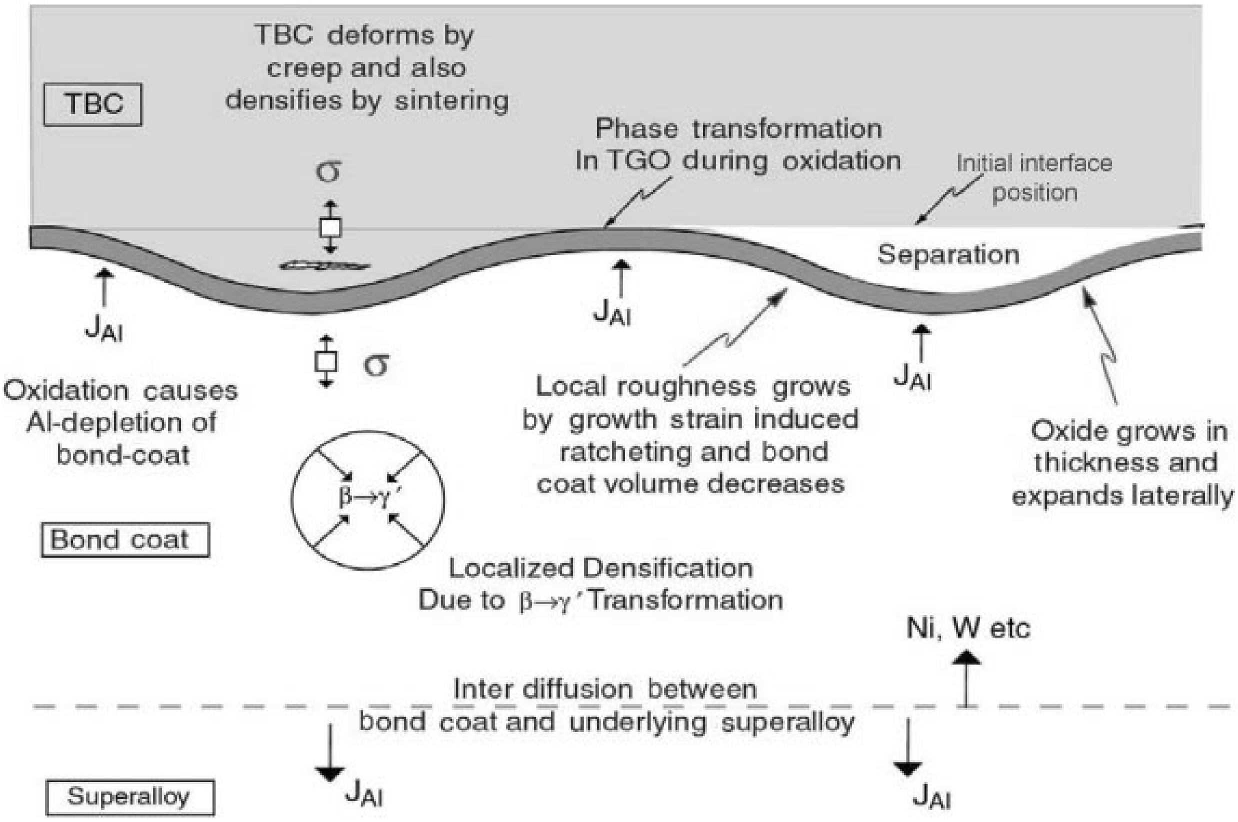

Figure 15 Failure mode in TBC systems [58]

2.7.1 Spallation

Spallation means that pieces or large areas of the topcoat are broken off and removed from the coating system. This failure mode generates not only a poorer TBC in terms that it can no longer protect the substrate material from the hot environment in the same way, but also that the debris formed present a danger to other components in the system [58]. In the application covered here, exhaust manifolds, the next component in line, the turbo charger, is sensitive to debris. Hence, spallation cannot be allowed since this could generate a complete failure of this component.

The largest contributing factor to TBC failure is associated with the thermally grown oxide [58]. There are two main classes of bondcoats used today that are designed to increase bonding between substrate and coating and also to form Al_2O_3 when being exposed to air and high temperature [58]. The Al_2O3, which is one of the slowest growing oxides at high temperature, is preferred as it acts like an oxidation barrier for the substrate. The Al_2O3 results in the layer referred to as TGO present between the bondcoat and topcoat. This desired shielding mechanism also counts for many of the problems generating failure over time. Due to both high temperature and diffusion, depletion of Al in the bondcoat may occur [58]. This depletion becomes damaging when the Al concentration falls below 8% in the bondcoat, Aluminium oxide is no longer the preferred oxide formed in the TGO, resulting in less protective spinels. These spinels increase the oxidation rate of the substrate, generating a premature failure. Since this change in preferred oxide formation takes place, the result is a gradual phase transformation in the TGO with accompanied volume change. The phase transformation and volume change can affect the coating in different ways but, in general, the growth of TGO result in failure introduced by either buckling or delamination [7]. The buckling/delamination and accompanied spallation of the coating is generally introduced due to compressive stresses present in the TGO due to the interlocking of TGO with the bond coat during subsequent growth [57]. As a result, the TGO layer becomes wavy to reduce the built up strain energy. The growth of TGO is not the only reason for the buckling. Compressive stresses can be introduced into the different layers by stresses from a mismatch in thermal expansion between the substrate and coating [7]. The buckling of the layers is accompanied by a plastic deformation of the TGO and bond coat and subsequently a separation of the TGO from the topcoat. During the buckling process, the compressive stresses in the interface changes to tensile stresses making it easier for crack propagation in the area [59]. The buckling introduces a roughness in the interface between the bond coat and topcoat, as can be seen in figure 15, the distance the crack needs to grow to reach a critical length is reduced. The inhibited micro cracks at the interface boundaries can travel along the TGO and the fact that the stresses change to tensile makes it easier for them to grow together [59].

To cope with the problem of bond-coat oxidation, one solution is to apply a thicker layer of topcoat to reduce the interface temperature [6]. However, with increased thickness the stresses affecting the topcoat internally increase [6], increasing the risk of spalling [1]. The thickness itself is not the only problem but also the thickness distribution. During the process of applying the coating the overall distribution of coating thickness over the substrate needs to be closely monitored. If the deviation over the surface is too large, it can result in spallation of the coating due to large local stress variation as Fig. 16 shows [6].

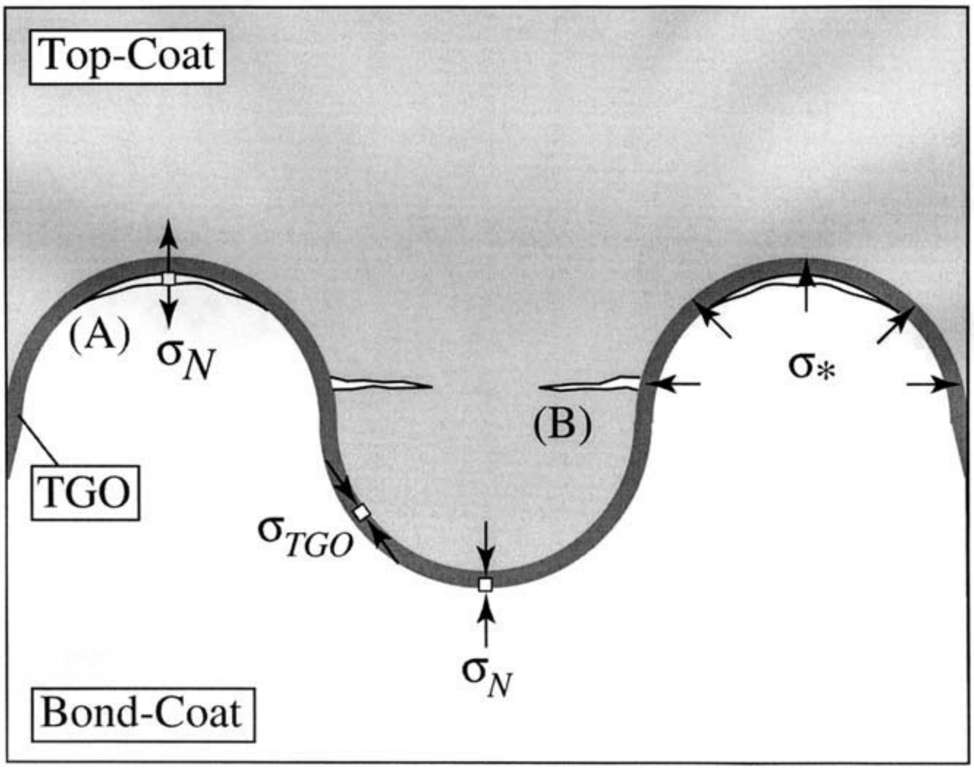

Figure 16 Failure modes in plasma-sprayed thermal barrier coatings [59]

2.7.2 Fatigue loads in manifolds

During operation of the engine, the exhaust manifolds are exposed to loads from both low cycle- (LCF) and high cycle fatigue (HCF), affecting the TBC. The thermal cycling generates the LCF and pressure change of the exhausts, while the engine-introduced vibrations generate the HCF [36]. The thermal cycling and the pressure change have been covered in earlier sections; the combination of HCF and LCF will be covered here.

The combination of HCF and LCF generates a much higher crack density on the ceramic topcoat compared to pure LCF loading [9] and therefore generates a much higher spallation risk. The micro cracks do not only present a problem in terms of the spallation risk, cracks at the surface can promote particle intrusion [9]. Particle or gas intrusion can in most cases lead to an increase in thermal-introduced stresses due to their different volume expansion and also an increase in thermal conductivity [9], all resulting in a far less effective thermal barrier. The effects generated by this combination of both LCF and HCF is, in manifold applications, dangerous since the spallation can cause a catastrophic failure of the engine due to turbo-charger failure [36]. TBC have, on the other hand, shown to have a positive effect on the HCF lifetime of the substrate material. The coating system, due to its tendency to produce and drive micro cracks trough the topcoat have a damping effect on the vibrations [9], increasing the HCF lifetime of the substrate.

2.7.3 Creep

Since most failures occur at the interface between TGO and topcoat during cooling, the stress levels in the TGO becomes an important parameter [60]. Rösler et. al. showed that the radial stresses acting through the entire TBC depend primary on thermal expansion and TGO growth [61]. What Rösler found was that the stresses cased by TGO growth could be reduced by creep relaxation, either in topcoat or in the TGO. If TGO is creep deformed, the effect is a significant reduction in TGO growth stresses and, hence, longer TBC life expectancy [60]. The cycling process can also activate creep relaxation. The coating process-induced compressive stresses present in the topcoat undergo a relaxation due to creep, which in a ceramic material has a large impact on the fracture toughness and hardness [60]. Even though creep can function as a stress relaxation-mechanism, creep from thermal cycling is one of the driving forces behind roughening of the interfaces between TGO/top-coat and TGO/bond-coat [61]. This phenomenon is referred to as ratcheting and can arise, during thermal cycling and in the presence of imperfections in the interface. The ratcheting means that TGO penetrates the bond coat and subsequent formation of stresses acting normal to the interface that eventually results in failure [61].

2.7.4 Hot Corrosion and material resistance

Zirconate

One of the big problems associated with thermal barrier coatings is their tendency to crack and spall. Some fuels contain compounds of Na and V, which can form salts, such as Na2SO4 or NaVO3, which can be distributed over the barrier surface [62]. The reaction causes a degeneration of the stabilizing yttria that makes the temperature stability of the TBC decrease. The degeneration of yttria introduces the phenomenon that pure zirconia exhibits, namely phase transformations. Zirconia forms the monoclinic phase upon cooling in the gas cycle and this crystallographic change leads to a volume increase, normally around 3-5% [63]. This volume increase is then accompanied by cracks and spallation. To increase the lifetime of TBCs working in these environments, one solution is to introduce a new top layer above the YSZ consisting of Al2O3 [62]. Alumina is more stable than yttria, resulting in a decrease in crack formation and spallation risk.

Mullite

When hostile environments are a problem, Mullite is usually used as a protective coating to cope with this problem. Experiments have shown that substrates coated with Mullite remain unaffected of hot corrosion and that after more than 100h only 1 µm of the Mullite coating has found to be affected [64]. This should mean that for Na and V rich environments, Mullite would show good resistance to hot corrosion. It should be mentioned that during these tests, Mullite was coated using CVD process and that the more porous microstructure characterized by APS should be more affected [22].

$La_2Zr_2O_7$

As for Mullite, $La_2Zr_2O_7$ shows greater resistance towards hot corrosion if vanadium is present. At temperature up to 1000°C, the bonding between topcoat and bond coat is almost unaffected compared to surface characteristics without presence of vanadium [65]. Experiments have shown that during heat treatment, LaVO4 forms as a new phase, which due to volume changes could affect the bond area. Luckily, is been shown that at temperature below 1000°C, this new phase present itself as a minor component and has shown to have no effect on the bonding [66]. The volume change has, on the other hand, an effect on the topcoat itself due to the stresses it introduces, but since the LaVO4 is only a minor component this should not affect the lifetime in a sever way [65]. If instead sulphur is present in the environment, La2Zr2O7 shows a large reduction in thickness due to cracking and delamination. At the same temperature as above, reduced thickness by as much as 50% has been recorded over a short period of time. The so far best estimation is that the decomposition of the coating is due to formation of MgO. Mg, which is a result of the decomposition of the sulphur salt, reacts with the coating and creates volatile phases and chemically breaks down the coating [67].

Forsterite

Studies of Forsterite have shown no signs of effect of the salts at temperatures below 1000°C, no matter the atmosphere or environment [68]. Forsterite that is of the cordierite ceramic could, on the other hand, display similar behaviour as the others. Na-salts have shown to degenerate the Mg content of the bulk topcoat and increase the Mg content at the outermost surface. At the surface, it has also been found that during temperatures above 1000C, idiomorphic crystals forms, MgO and Mg2SiO4 [96]. The Mg2SiO4 forms as a result of a Na2SO4-rich environment while MgO forms in NaCl environments. The same phenomena can be seen from K-salts (KCl and K2SO4) where Mg2SiO4 forms as a result of the environment [69]. With this fact, it should be possible for Mg2SiO4 (Forsterite) to be a very stable coating during these kinds of environments. If NaCl is present, it should be noted that the Mg content closest to the bond coat could suffer depletion if MgO is formed at the TGO, creating a volumetric change that can lead to failure over a long period of time [64].

As stated above, both 8YSZ and Mullite have shown to be quite stable in the presence of NaCl. Tests have shown that in the presence of pure synthesized NaCl at high temperatures between 700-930°C, there are no signs of spallation or hot corrosion of 8YSZ [70]. The effect that sodium has on the Mullite coating is so small that it can be neglected for this application. Sea salt, which have other chlorides than NaCl and also sulphate compounds, have, on the other hand, shown to have a derogating effect on the La2Zr2O7-based thermal barrier coating together with the damaging effect is has on the NiCrAlY bondcoat where chloride ions react with aluminium and creates a depletion due to the formation of aluminium chloride [64, 70].

3. Method

To investigate the performance of the different thermal barrier systems, five different topcoats were applied using APS onto three different types of substrates. The topcoats together with the bondcoat Amdry 962, were supplied in as-sprayed condition from Sulzer. Four samples of each system were place inside a furnace with a programmable thermostat. The thermostat was programmed for thermal cycling following the profile seen in figure 19. The samples were held inside the furnace for 1000h (170 cycles) and a surface analysis was performed every 15 cycle. After 500h (85 cycles), one sample of each combination was removed and a cross-section analysis was performed. The same analysis was the conducted on remaining samples after the complete 1000h cycling. The results from the cross-section- and the surface analysis were compared to reference samples.

3.1 Sample preparation

The samples used for this evaluation can be seen in figure 17. The coins where constructed with a radius of 6mm and a thickness of the substrate of 4mm.

Figure 17 Air Plasma sprayed prepared sample

The substrate materials, SiMo51, D5S and HK30 were cast into blocks with geometry as shown in Fig. 18. The setup with cylinder edges was used to even out the temperature gradient of the area highlighted in black as well as to reduce the shrinkage porosity. The cylinders as well as 7 mm of the edges of the planar plate were cut, leaving a central plat for sample preparation. The plate was then cut into bars that were lathed into 12mm diameter rod. These rods where cut into coins with a thickness of 4mm. These samples were sent to Sulzer Metco for coating. Sulzer coated the samples using a setup with an Internal APS gun F210. The Spraying parameters can be seen in table 3. Table 4 shows the number of passes together with the application rate for each of the applied coatings. In table 4 the presented thickness of each coating from Sulzer is presented together with the measured thickness.

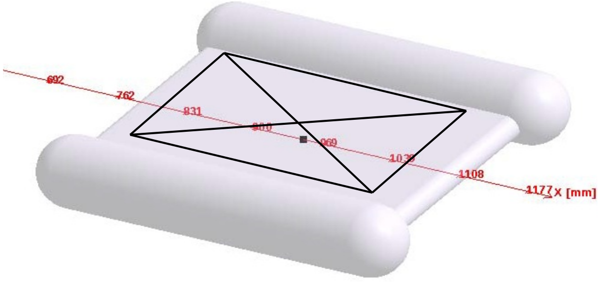

Figure 18 Schematic view of the cast plates used as substrate

Table 2 Spray parameters presented by Sulzer

Layer	Ar flow [NLPM]	H2 flow [NLPM]	Current [A]	Feed rate [g/min]	Stand-off distance [mm]
Bond coat	30	3.5	350	30	45
Top coats materials	30	5	400	40	45

Table 3 Spray parameter for each of the applied materials

Material	Passes	Application rate [µm/pass]	Thickness [µm]	Measured thickness [µm]
Amdry 962	12	16.67	200	135 ± 12
8YSZ	42	10.71	450	381 ± 13
Mullite	18	24.44	440	440 ± 21
Forsterite	14	27.14	380	301 ± 9
Nanostructured 8YSZ	30	13.33	380	261 ± 23
La2Zr2O7	26	14.62	360	294 ± 7

3.2 Thermal cycling

For the thermal cycling a Carbolite 1100 CWF furnace was used together with a programmable thermostat, Eurotherm 3208. The thermal cycling profile together with the programmable parameters can be seen in figure 19. Due to the limitations of the furnace, the ramp rate varies. Because of the lack of cooling equipment during the cycling, the cooling rate is dependent on the self-cooling of the furnace. Between step 1 and 2, the cooling rate was set to 30°C/min, between 2 and 3 to 6°C/min and between step 3 and 4 to 30°C/min, and between 5 and 6 to 25°C/min, which was the maximum rate of the specific furnace at given temperature ranges. The atmosphere in the furnace was held at laboratory air.

Four test specimens of each TBC systems were placed into the furnace and the cycle shown in Fig. 19 was repeated over a time period of 1000h, generating a total of 170 cycles. Every 15 cycle, the furnace was stopped to be able to analyse the surfaces of the test specimens. After half the time, 500 h, one specimen of each TBC system was removed from the furnace and a cross section analysis was performed together with surface analysis. The remaining samples were then analysed every 15 cycle and held in the furnace until the complete cycle time had ended. These samples where then analysed using the same procedure as for 500h.

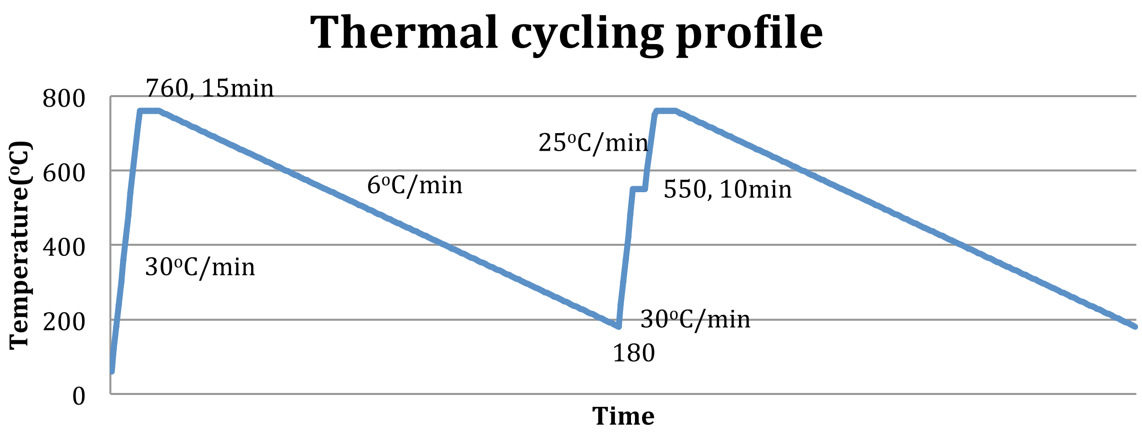

Figure 19 Thermal cycling profile and programmed values

3.3 Thermal Conductivity

The thermal conductivity was determined using Eq. 2, giving the thermal conductivity as function of the thermal diffusivity, specific heat and density, described in section 2.5.1.
The properties are determined using a Laser flash method, image analysis and theoretical calculation models further described below.

3.3.1 Thermal diffusivity

The thermal diffusivity of the TBC system was measured using a multilayer Laser flash method [71] over a temperature range from room temperature to 1000°C. The Laser flash was conducted on all TBC-systems applied on SiMo51 at Jönköping University. The method for determining the thermal diffusivity of a system containing three layers follows the ASM standard E1461-02. The schematic view of the setup can be seen in Fig. 20.

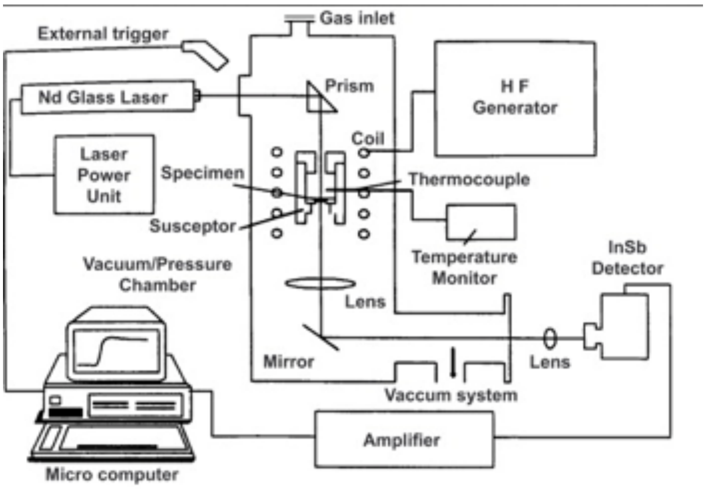

Figure 20 Schematic view of the laser flash method [71]

During the process, the sample is heated inside the furnace to the temperature for which the experiment should be conducted. When the temperature of the specimen is uniform, a short pulse, typically 1ms, from the laser of flash lamp is fired onto one side of the sample. On the unaffected side a non-contact Ir-detector is placed to record the temperature change over time [72]. The data obtained, together with the thickness of the sample is then used to obtain the thermal diffusivity following Eq. 3 [72].

$$\alpha = \frac{1{,}37d^2}{\pi^2 t_{1/2}} \tag{3}$$

Where d is the thickness of the sample and $t_{1/2}$ is the time for the opposite side to reach half of its maximum temperature.

To evaluate the different topcoats the influence of the substrate material and the bondcoat needs to be corrected for [71]. The data for the substrate material was obtained from a separate Laser flash measurement while the data for the bondcoat was obtained from literature.

3.3.2 Specific heat and density

C_p of the different coatings was calculated using a weighted average value based on the mass of the elements present. To compensate for the porosity of the layers an image analysis was performed. The resulting value were then thought of as an average of entire surface, rendering an at room temperature C_p value of the porous layer. The room temperature densities of the layers were also calculated using the porosity. A literature value of the density for a full dense material was modified for the specific porosity showed using the image analysis.

Density

The density of the bondcoat and topcoats was determined with an image analysis method [106]. This image analysis method involves determining the area fraction of different phases, in this case the pores. The density of a fully dense material (less then 0,5% porosity) is then modified to fit the given porosity following Eq. 4 [73].

$$\rho_m = (1 - f)\rho_{99,5} + f\rho_{phase2} \tag{4}$$

Where f is the pore volume fraction, $\rho_{99,5}$ is the density of the fully dense material and ρ_{phase2} is the density of the second phase present. In this case the ρ_{phase2} is set to zero due to the small density contribution of oxygen.

The image analysis was performed using the Zeiss Axio imager A2m together with the Axiovision Rel. 4.8 software. For each of the samples five measurements were conducted and an average area fraction was used. The resulting values from as-coated condition can be seen in table 5.

Table 4 densities of the different materials

Material	Mullite	Forsterite	8YSZ	$La_2Zr_2O_7$	Nano 8YSZ	NiCrAlY
Density (g/cm^3) at the most 0,5% porosity	3,17(74)	3,275(75)	6,10(76)	6,05(77)	6,10(76)	-
Measured porosity (%)	15,6	20,8	16	16,5	24,2	-
Density at given porosity (g/cm^3)	2,68	2,59	5,12	5,01	4,62	6,58 (78)

As can be seen in table 5, the density for the NiCrAlY alloy has been collected from literature due to small variations in average porosity level, if applied using the APS method [78].

Specific heat

The specific heat at room temperature was theoretically calculated using the Neumann-Kopp rule [79]. The Neumann-Kopp rule states that the specific heat of an alloy can be estimated using Eq.5.

$$C = \sum_{i=1}^{N} C_i * f_i \tag{5}$$

Where f_i is the volume fraction of alloying element i and C_i its specific heat.

The Neumann-Kopp rule has been found to generate values close to experimental for metallic alloys, but is limited in the presence of oxygen [79]. The standard Neumann-Kopp rule generates a too high error margin when viewing oxygen as a constituent of its own. Therefore, the Neumann-Kopp rule can be modified, using the constituent additive method [80] to apply to oxides. The constituent additive method states that the specific heat of a complex compound, $A_aB_bC_c$ can be computed from its constituent oxides [80] generating the expression seen in Eq. 6.

$$C_p(A_aB_bC_c) = \alpha C_p(A_xC_{c1}) + \beta C_p(B_yC_{c2}) \tag{6}$$

Were the prefixes α, β, *x, y, c1 and c2* are fractions to balance the constituent oxide combination. For example the specific heat of $La_2Zr_2O_7$ can be calculated as the specific heat of $La_2O_3 + 2ZrO_2$. The NiCrAlY alloy does not contain any oxide and the standard Neumann-Kopp rule can therefore be applied.

Since the constituent additive method applies in mole, the imperial standard for specific heat, J/mK, must be used. This generates a third expression for the specific heat in the SI- unit, J/gK, which can be seen in Eq. 7.

$$C_p\left[\frac{J}{gK}\right] = \frac{C_p[\frac{J}{mK}]}{m[\frac{g}{mole}]} \tag{7}$$

The constituent oxides and elements that apply to the materials, together with their specific heat and molar mass can be seen in table 6.

Table 6 Tabulated values of different oxides and elements

	Al_2O_3	SiO_2	MgO	La_2O_3	ZrO_2	Y_20_3	Ni	Cr	Al	Y
Molar mass (g/mole)[81]	101.96137	60.08439	40.30449	325.80924	123.2228	225.8099	58.6934	51,996	26,981	88.90585
Cp (J/mK)[82]	79	44,4	37,2	108,8	56.2	102,5	26,1	23,4	24,2	26,5

In Table 7, the different constituent combinations of the coating materials, together with the calculated specific heat and some tabulated reference values can be found. As can be seen in the table, the specific heat at room temperature, for the conventional and nano-sized 8YSZ are given the same value. Literature show that the room temperature values are close together but the temperature dependence vary between the two [82].

Table 7 Constituent combinations and Cp values at room temperature

Material	Mullite	Forsterite	La2Zr2o7	8YSZ	Nano 8YSZ	NiCrAlY
Constituent combination	$3Al_2O_3 \cdot 2SiO_2$	$2MgO \cdot SiO_2$	$La_2O_3 \cdot 2ZrO_2$	$21ZrO_2 \cdot Y_20_3$	$21ZrO_2 \cdot Y_20_3$	-
Calculated Cp (J/gK)	0,76	0,84	0,39	0,455	0,455	0,485
Tabulated Cp (J/gK)		0,84 [83]		0,45 [84]		

3.4 Evaluation procedure

3.4.1 Surface analysis

The specimens that are used in the cyclic test are first analysed before being subjected to the thermal cycling. This analysis follows the same procedure as described below to generate a clear view of the starting position. To analyse the surface after a specified amount of cycles, 15, an IR-camera and a stereomicroscope are used for image analysis. When the samples are removed from the furnace an visual observation was done to ensure that the samples within the same TBC system looks approximately the same, to generate a fair view of the procedure.

Ir-camera

To analyse small defects, an Optris PI 400 Thermal imager was set up. The idea was that when cracks and spallation occurs the areas affected generates a higher thermal conductivity than the unaffected areas. The specification of the thermal imager implies that the thermal difference measurable is 80mK, this should generate the ability to spot crack propagation early [85].

The camera was set up at a distance of 20cm from the specimens to generate the highest resolution according to specification. The samples are placed under the lens and a video sequence was recorded in 120 Hz for each of the specimens. To minimize the heat loss to the environment the samples were placed on a hotplate held at 180°C. The video was later analysed using the Optris software PI connect, keeping the cycle downtime to a minimum.

Stereo microscope

The stereomicroscope, Zeiss Discovery V12, was used to investigate the surface after each 15 cycle. The samples where allowed to cool down after the thermal imaging and placed under the stereomicroscope. The same resolution was used for all of the samples giving an overview picture of the entire surface over time.

3.4.2 Cross section Analysis

To investigate the effect of thermal cycling on the microstructure, cross-sections of one sample of each TBC system after 500h and 1000h thermal cycling, where analysed using EDX, SEM and LOM. These samples are casted into a copper and Bakelite pellet using conventional methods. The pellets was then grinded approximately 3mm to reveal the sample cross-section. The cross-section surface was grinded and polished in the conventional way.

EDX/WDS

To analyse the chemical composition of the different elements in the layers and investigate oxide growth, EDX and WDS analyses was conducted. The EDS sensor, Oxford X-max 50 mm^2, was positioned in a Zeiss Sigma VP stationed at Scania. The WDS analysis preformed to easier classify the light elements was conducted at Swerea Kimab using a "Jeol 7000F, FEG-SEM equipped with Oxford Wave detector and X-Max $50mm^2$ EDS detector". Before each EDX session a quant optimization using a Cobalt sample was performed. For the evaluation of the EDS results the INCA software was used. Before the samples were placed into the SEM they were cleaned using the Fischione 1020 Plasma cleaner for 5 minutes.

LOM/SEM

The SEM Zeiss Sigma VP was used to visually analyse the different failure modes visible. Analysis was performed on both the surface and the cross section. The SEM was used together with the BSD to get a good view of the different layers and segregations.

3.5 Hardness measurement

The Vickers micro hardness of the materials is determined using the Matzuzawa MXT30 micro indentation. The hardness was measured in as-coated condition and after 1000h of cycling with the load of 300g. To generate an average value for the hardness the indentations was made on the cross-section samples. 10 indentations was performed following a zigzag pattern, schematically shown in Fig. 21, where X = 200µm and Y= 50µm.

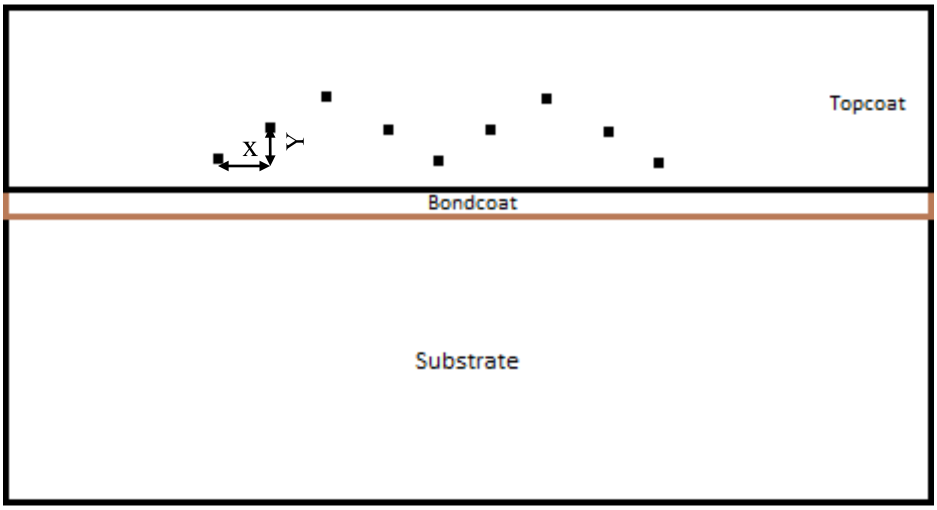

Figure 21 Schematically view of the Vickers indentation pattern

3.6 Fracture toughness and Young's modulus

Using the cracks initiated by the indentation during Vickers hardness test, the fracture toughness can be determined for brittle ceramic materials [86]. The method applies to use micro Vickers indentation with a load of 300g and measure the length of the initiated crack. A schematic view of the indentation can be seen in figure 22.

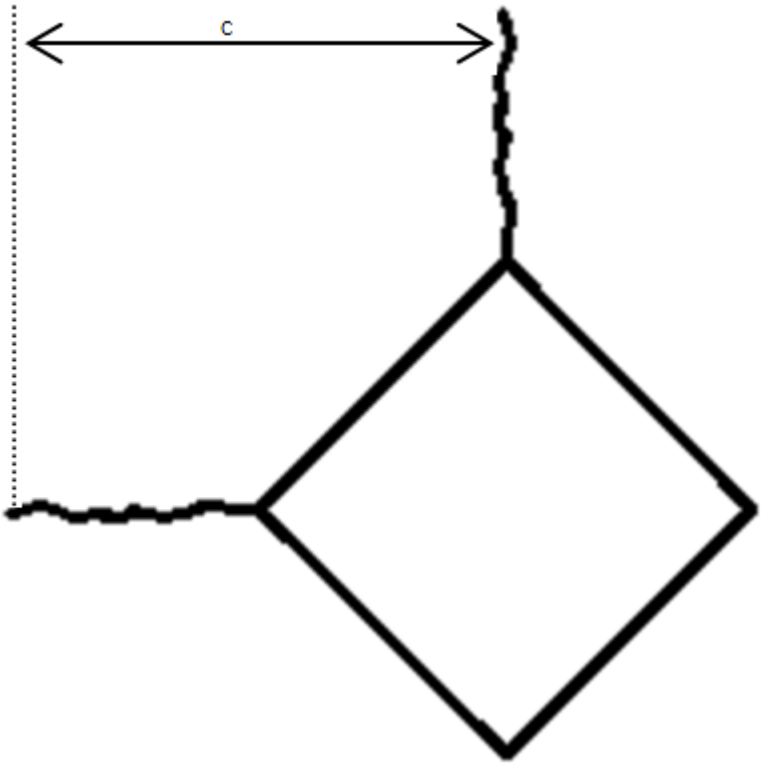

Figure 22 Schematic view of measurement of indentation generated cracks.

The fracture toughness of the coatings was determined using Eq.9 [86]. The influence of the hardness and effective young's modulus was used to acquire the fracture toughness for the coating. The effective Young's modulus (E^*) was calculated using Eq. 8 [86] using values tabulated values for the Young's Modulus (E) and poisons ratio (ν) seen in table 4, together with measured porosity (θ) from image analysis. The hardness (H) used in eq. 9 was the measured values from the hardness indentation test and the subsequent measured crack length (c) associated with each hardness measurement during the hardness test. C is the length of the crack measured from the centre of the indentation. The tabulated material parameters used can be found in table 4. The α parameter in Eq.9 is an empirical correction parameter set to 0,016 [86]

$$E^* = E\,\frac{(1-\theta)^2}{1+b_k\theta} \qquad (8)$$

Where:

$$b_k = \frac{1+\nu}{2(1-2\nu)}$$

$$K_{1c} = \alpha\sqrt{\frac{E^*}{H}\frac{P}{c^{3/2}}} \qquad (9)$$

In Eq. 9, E^* and H should be used in Pa, P, applied load during indentation, in Newton and c, radial crack length initiated during indentation, in meters.

Table 8 characteristic material properties for fully dense material.

Material	Mullite	Forsterite	La2Zr2O7	8YSZ	Nano 8YSZ
Young's modulus (GPa)	143 (87)	150 (88)	237 (89)	220 (90)	220 (90)
Poisson ratio	0.238 (87)	0,24 (88)	0,28 (89)	0,32 (90)	0,32 (90)
b_k	1,18	1,19	1,455	1,83	1,83

4. Result

4.1 Thermal conductivity

Fig. 23 below shows the thermal diffusivity of the different coating materials, with the exception of $La_2Zr_2O_7$ measured using laser flash. $La_2Zr_2O_7$ are not shown due to malfunction of the analysis software during these measurements.

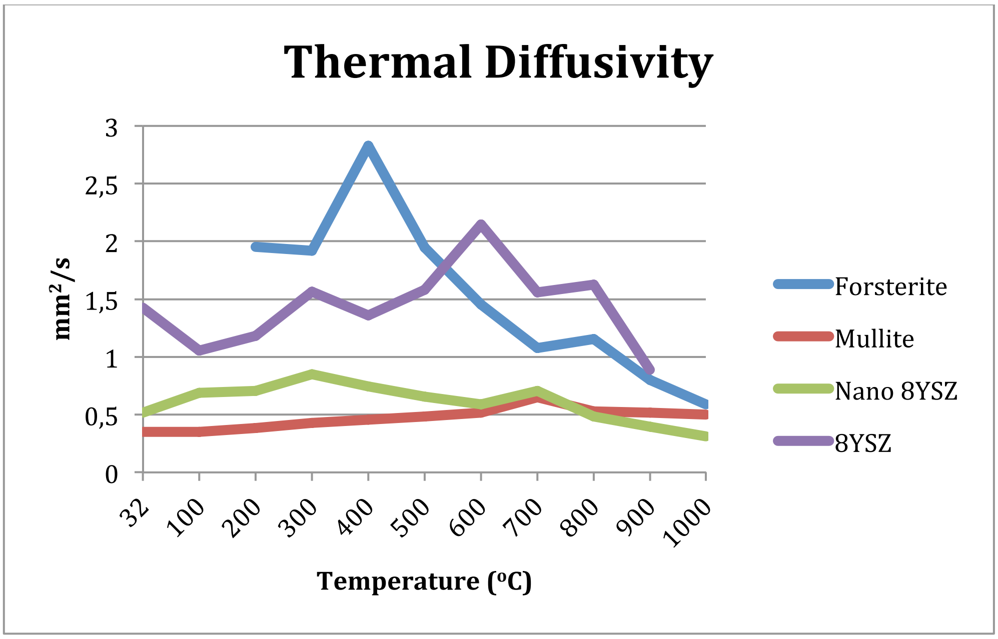

Figure 23 Thermal diffusivity of the coated systems

The Thermal conductivity for the materials can be seen in Fig.24 below. As the figure shows, the material exhibiting the highest thermal conductivity is Forsterite. Mullite and the nano 8YSZ coatings show a similar behaviour with the lowest thermal conductivity. The nanosized 8YSZ showed lower thermal conductivity compared to 8YSZ.

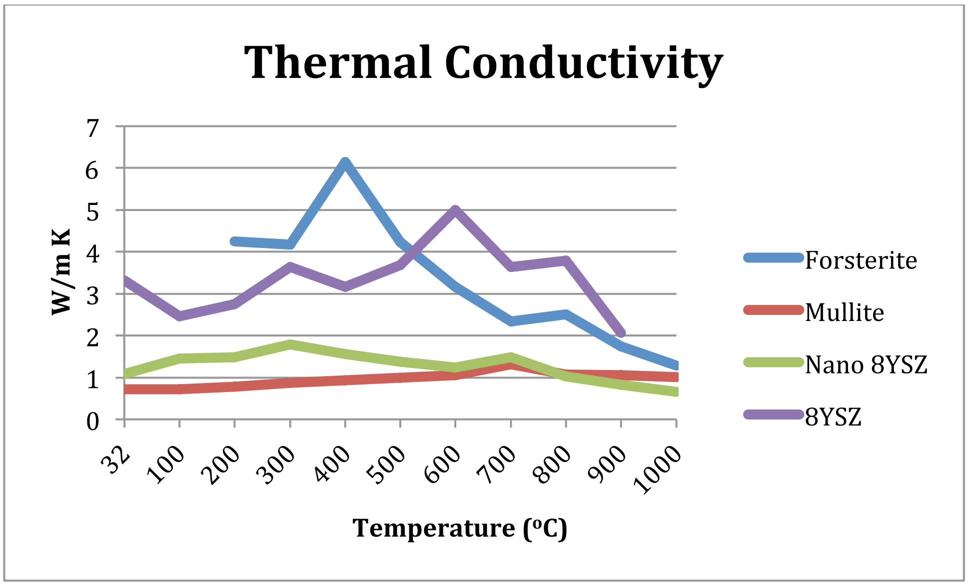

Figure 24 Thermal conductivity of tested materials

4.2 Porosity

The porosity measured using image analysis are shown in Fig. 25. As can be seen in the figure, the zirconia-based coatings exhibit the same type of behaviour. The three coatings shows an increase in porosity over the first 500h, with initial slopes of 0,82, 0,98 and 0,84 %/100h corresponding to 8YSZ, Nano 8YSZ and La2Zr2O7. The increase is followed by a stabilisation of the porosity for La2Zr2o7 and a small increase can be seen for both of the 8YSZ coating. The Mullite and Forsterite coating does not show the same large increase during the first 500h, they instead act stable over the timespan.

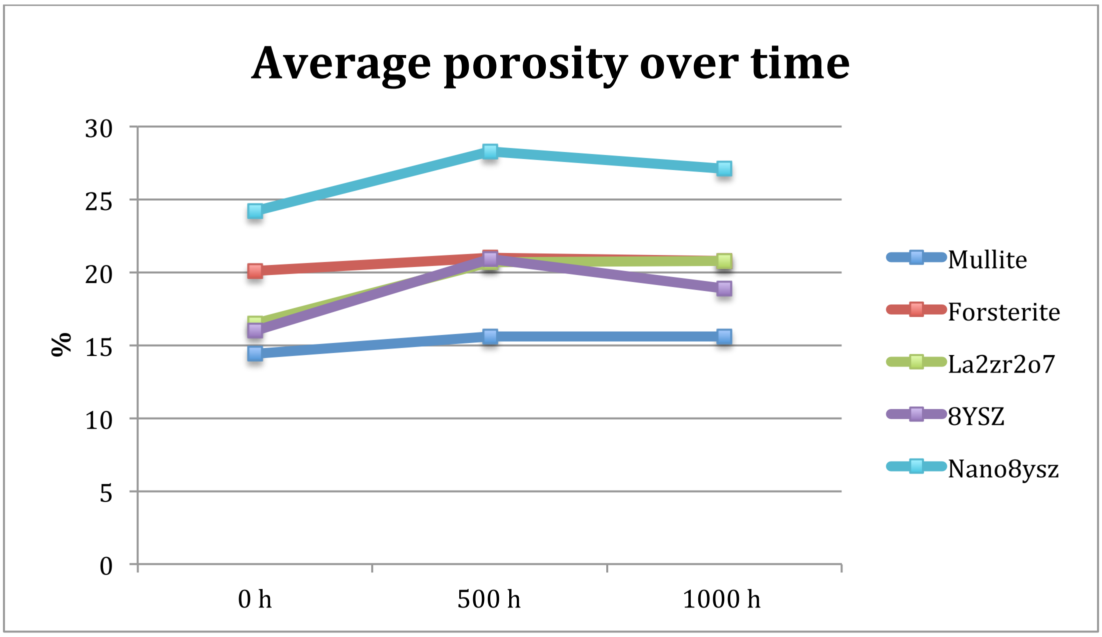

Figure 25 The measured average porosity measured at 0, 500 and 1000h.

4.3 Effective Young’s modulus

The effective Young’s modulus of the 5 different coatings can be seen in table 9. As can be seen from Fig. 26 the effective Young’s modulus shows the inverted behavior to the measured porosity with an initial decrease and then stabilization.

Table 9 variation of effective young's modulus over time

Coating	Mullite	Forsterite	La2Zr2O7	8YSZ	Nano 8YSZ
Young’s modulus fully dense (GPa)	143	150	237	220	220
Effective young's modulus 0 h	89,5	77,2	133	120	87,5
Effective young's modulus 500 h	86	74,9	114,5	99,5	74,5
Effective young's modulus 1000 h	86	75,4	114,1	107,4	78

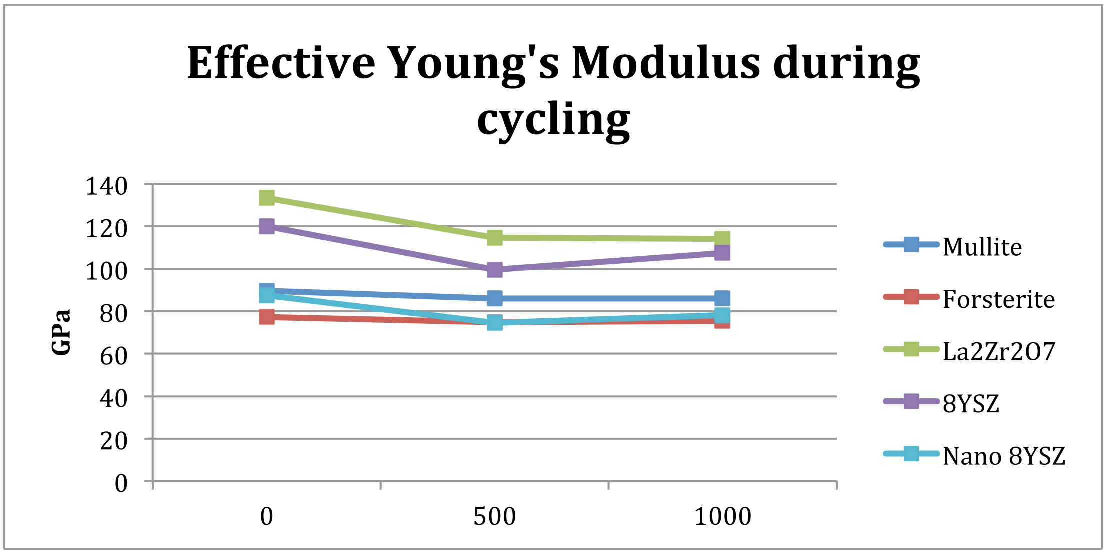

Figure 26 effective Young's modulus as a function of porosity measured over time

4.4 Vickers Hardness

Fig 27 shows the average hardness of the ceramic materials used as topcoats at as-sprayed condition and after 1000h cycling. As can be seen from the figure, the materials exhibit a decrease in hardness during the cycling where Forsterite showed the largest decrease of 44,4% after 1000h of cycling.

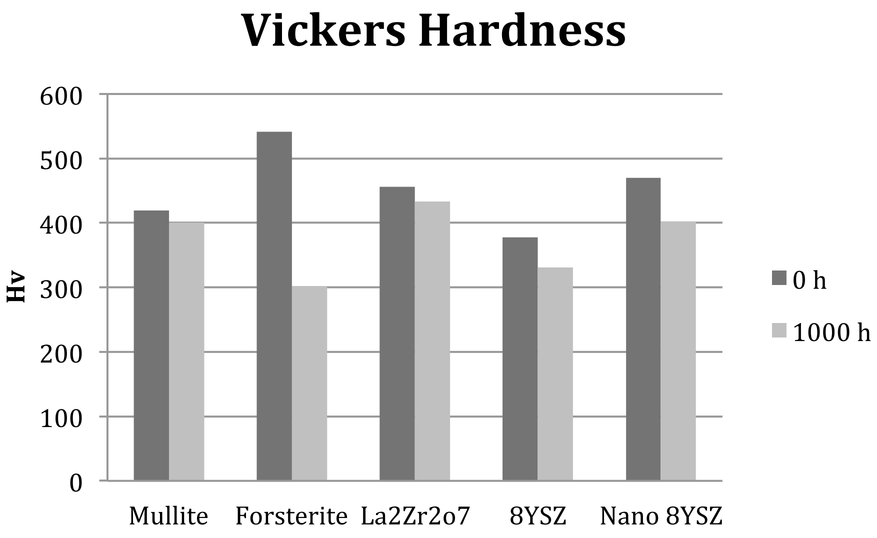

Figure 27 Vickers hardness variation of the different coatings at 0h and 1000h.

4.5 Vickers indentation Fracture toughness

The fracture toughness of the ceramic materials can be seen in Fig 28. As the figure shows, there is a decrease in $K1_c$ after 1000 h, for all of the analysed materials. The fracture toughness varies between 1,9 and 1,65 for the strongest, Mullite, and between 0,99 and 0,97 for the weakest, Forsterite. As can be seen from the figure, the zirconia-based coatings shows almost similar decrease. The decrease for the Zirconia-based coatings vary between, 22% for $La_2Zr_2O_7$, 22,5% for 8YSZ and 21,5% for Nano 8YSZ.

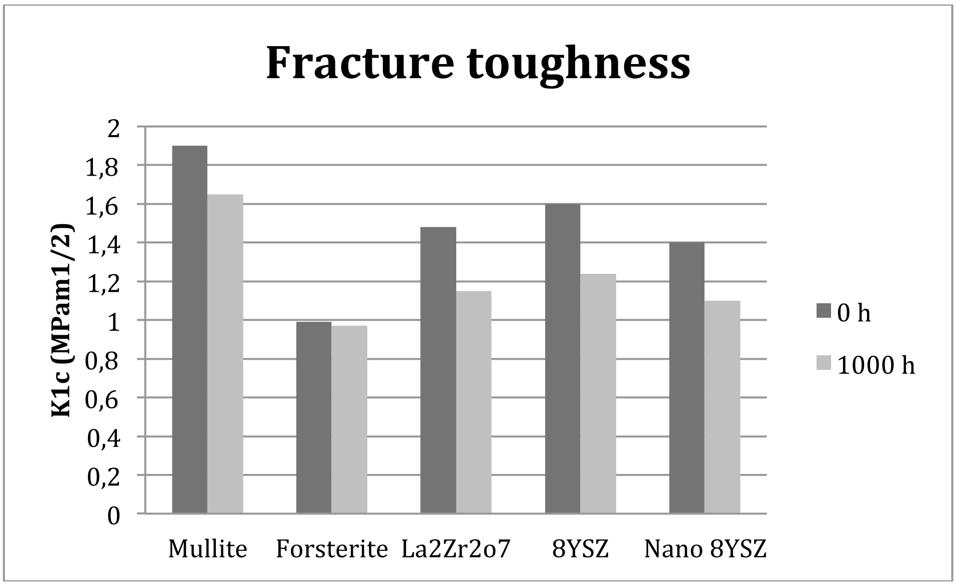

Figure 28 Fracture toughness of the different coatings between 0 h and 1000 h.

4.6 Oxide growth

As can be seen in Fig, 29, there is no formation of continuous TGO layer between the topcoat and bondcoat for any of the samples. The EDX-results, presented in table 10, shows the presence of aluminium and oxygen at the interface but not as a continuous visible layer. Fig.30 shows the formation of oxides within the bondcoat itself. The results from the EDS-analysis can be seen in table 11. Fig. 29 and Fig. 30 show the NiCrAlY bondcoat on the D5S substrate, however, similar behaviour was observed for SiMo51 and HK30 as well.

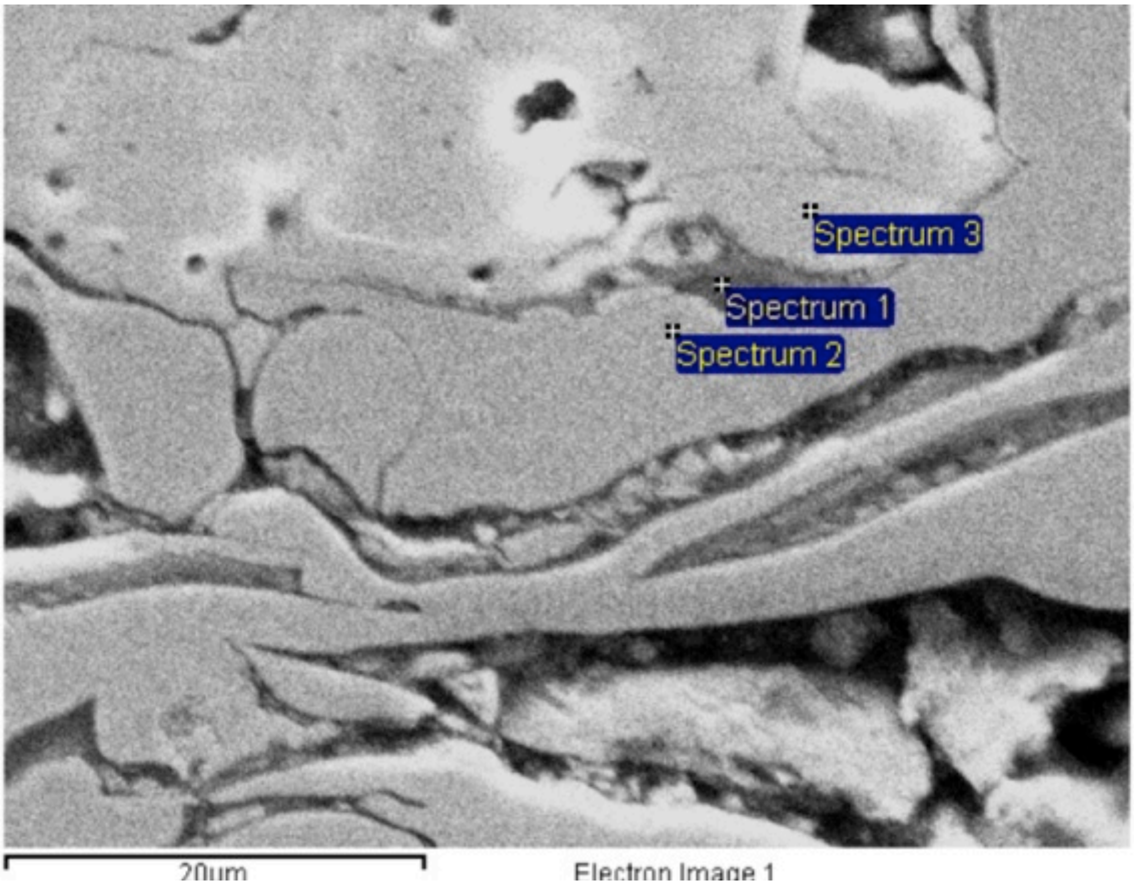

Figure 29 Interface between NiCrAlY and 8YSZ showing no sign of continous TGO layer but local formation of Al containing oxide

Table 10 EDS result showing the Weight % of the elements

Spectrum	C	O	Al	Cr	Ni	Y	Zr	Hf	Total
1	7,21	38,58	27,78	11,34	9,96	6,76			101,63
2	7,4		10,3	22,4	67,3	1,2			108,6
3	3,54	36,93				4,56	58,53	2,51	106,07

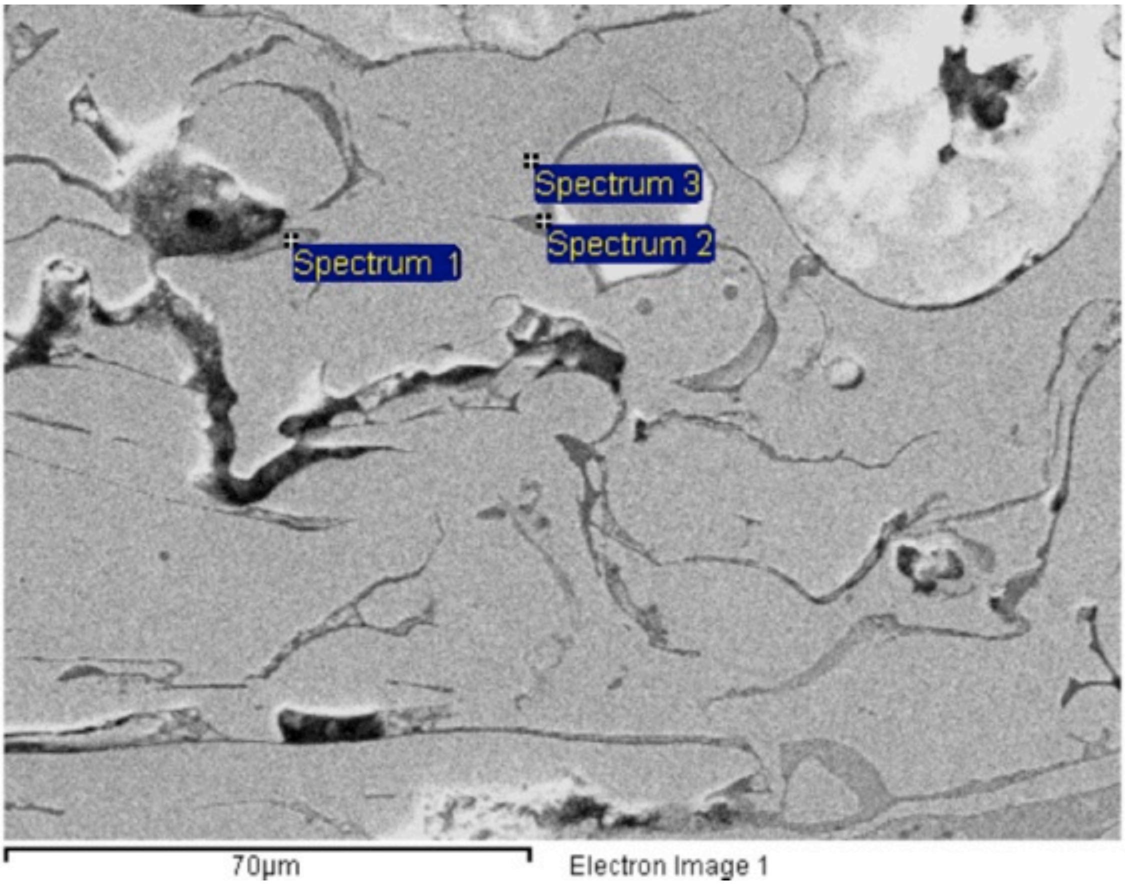

Figure 30 Formation of Al containing oxide within the bondcoat and no continuous TGO layer.

Table 11 EDS results showing the weight % of the elements

Spectrum	C	O	Al	Cr	Ni	Y	Zr	Hf	Total
1	4,63	35,17	22,47	2,27	3,8	33,7			102,04
2		39,95	33,16	2,76	2,84	22,68			101,39
3	2,64		8,66	20,77	70,38	0,42			102,87

Fig. 31 shows the formation of a continuous layer present at the interface between the bondcoat and SiMo51 substrate. No such layer where found in either D5S or HK30. Table 12 shows the results from the WDS analysis conducted at the interface. The figure also shows the prevalence of the formed layer into the voids within the bondcoat. As the spectrums show there is a high amount of oxygen within the different layers together with an increase in Silicon content compared to the bulk material in layer 3 and 4.

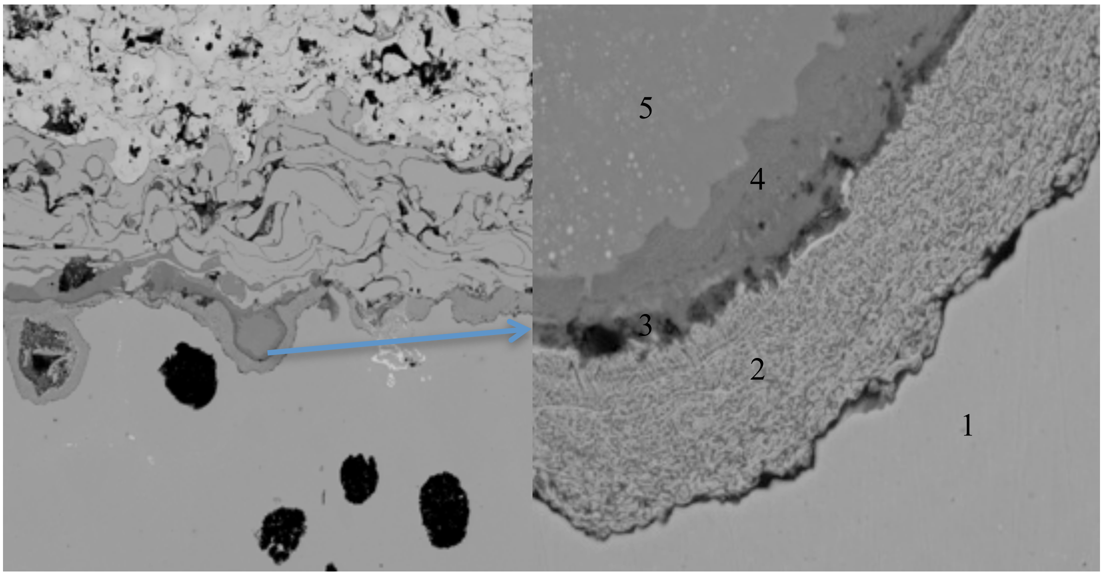

Figure 31 Oxide formation at interface between NiCrAlY and SiMo51 after 1000h.

Table 12 Chemical composition of the different layers obtained by WDS. Values presented in their normalized state.

Spectrum	C	O	Si	Cr	Mn	Fe
1	7,01	3,01	8,08	0	0,15	81,75
2	4,39	30,11	7,86	0	0,46	57,18
3	3,78	45,44	10,24	0,07	0,54	39,93
4	3,30	56,42	10,52	0	0,42	29,34
5	4,01	51,75	0,19	0	0,14	43,91

4.7 Failure modes

Below follows a number of SEM picture showing the crack propagation, oxide growth, spallation and delamination of the different systems tested during the cycling.

4.7.1 $La_2Zr_2O_7$

As shown in Fig.32, microcracks are formed in the $La_2Zr_2O_7$ coating after 1000h of thermal cycling. When compared to the reference sample material (0h of cycling Fig. 33) it could be observed that the amount of visible cracks increases with cycling time forming a web-like crack structure.

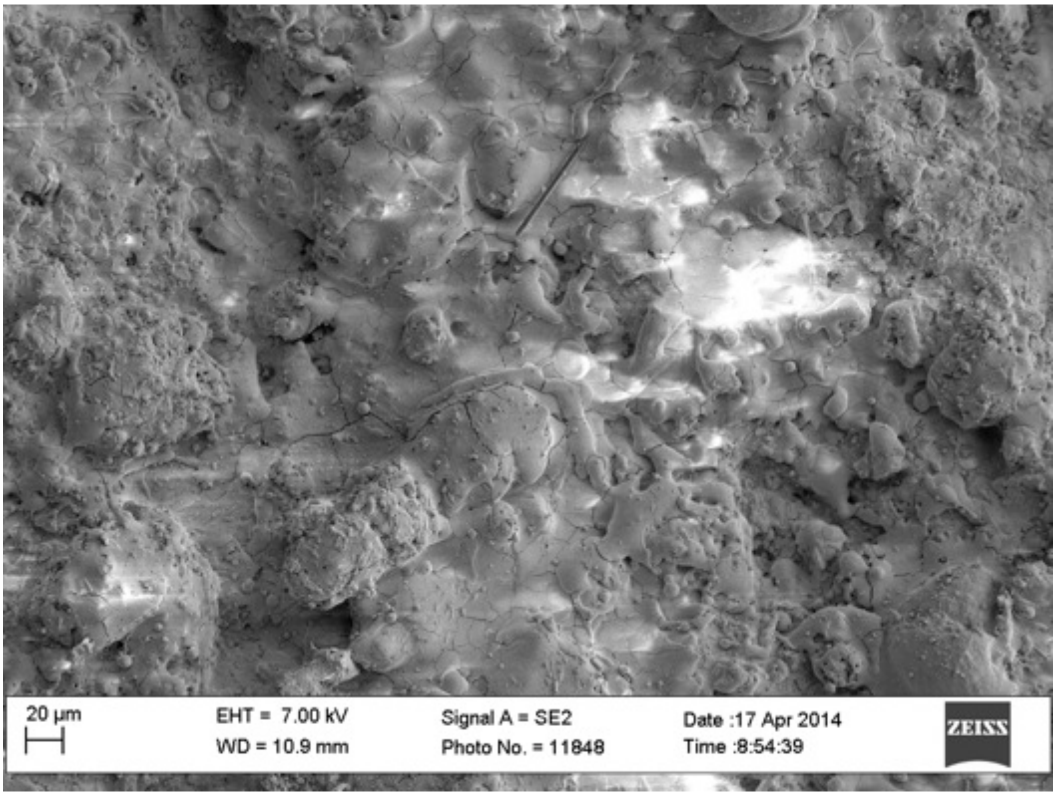

Figure 32 showing increased amounts of surface cracks of $La_2Zr_2O_7$ coating after 1000h.

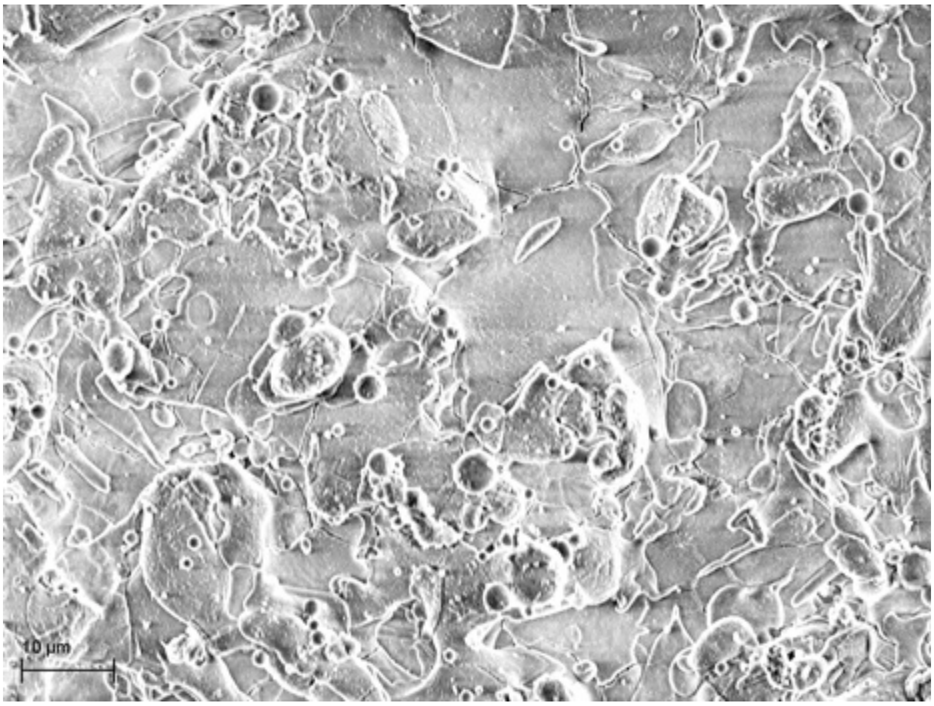

Figure 33 $La_2Zr_2O_7$ reference sample surface

Fig. 34 shows small size spallation of the $La_2Zr_2O_7$ coating after 1000h. None of the other tested coatings showed any sign of surface spallation over the 1000h cycling.

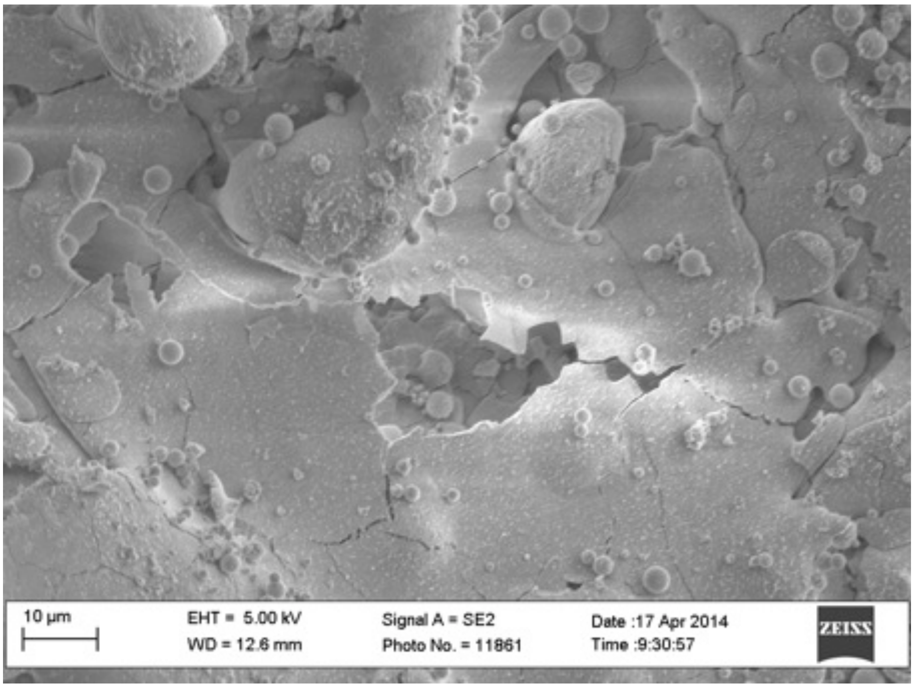

Figure 34 Small size spallation of coating $La_2Zr_2O_7$.

$La_2Zr_2O_7$ micro cracked cross-section in its as-coated condition can be seen in fig 35. The larger cracks run parallel to the interface and no large lateral cracks are visible. Comparing to the 1000h structure, there is an increase in larger lateral cracks seen in figure 36.

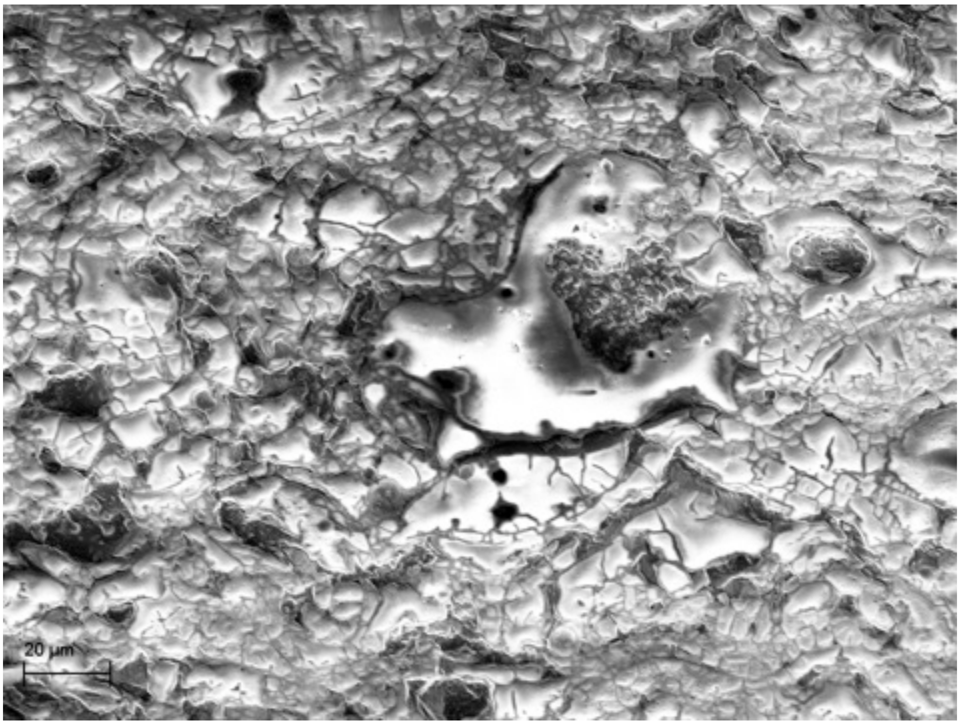

Figure 35 starting cross-section structure of La2Zr2O7.

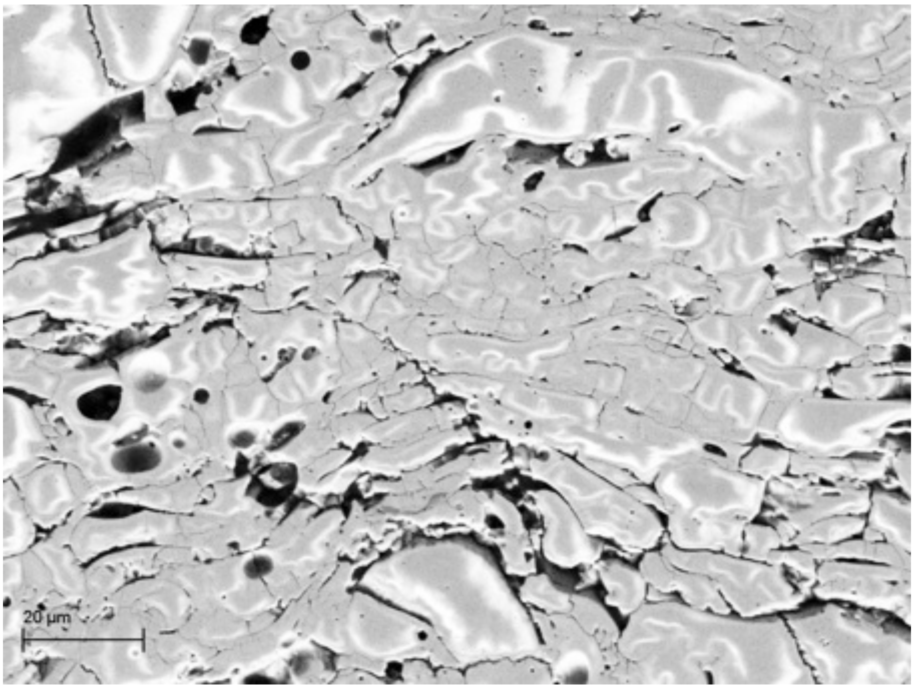

Figure 36 formation of lateral crack within La2Zr2O7 after 1000h cycling.

4.7.2 Mullite

Mullite exhibited a crack free surface and cross-section in its as coated condition. After 500h the Mullite coatings on HK30, D5S and SiMo51 substrate had started to delaminate but no cracks within the coating was observed, as can be seen in Fig. 37.

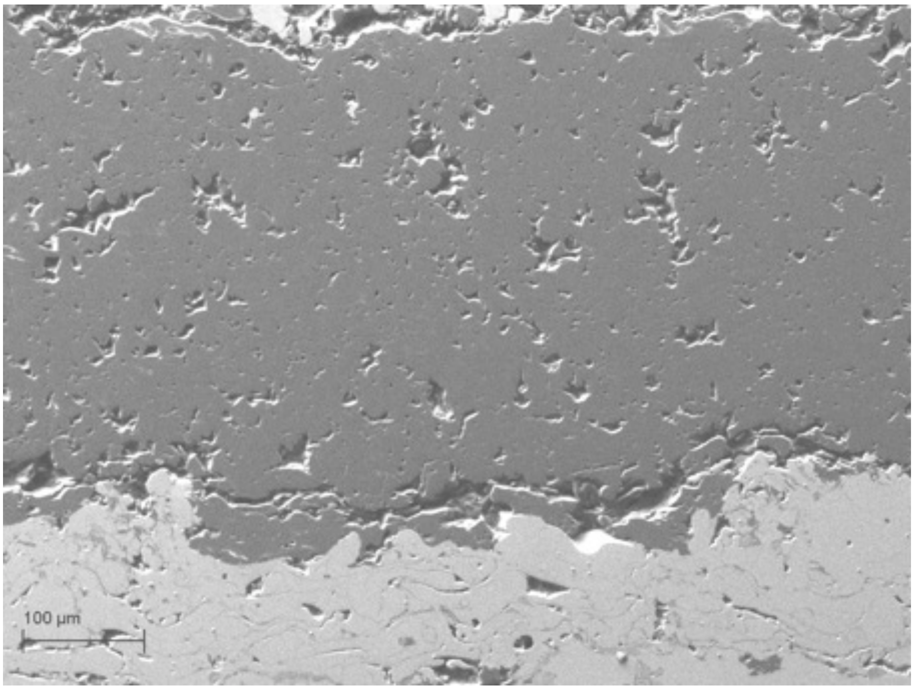

Figure 37 Mullite coated onto SiMo51 showing the initial delamination after 500h cycling seen on all substrates.

Fig. 38 shows the Mullite cross-section after 1000h were the delamination can be seen to increase and the formation of smaller cracks within the coating. The formation of cracks can be seen in Fig. 39. The same behaviour independent on substrate was spotted.

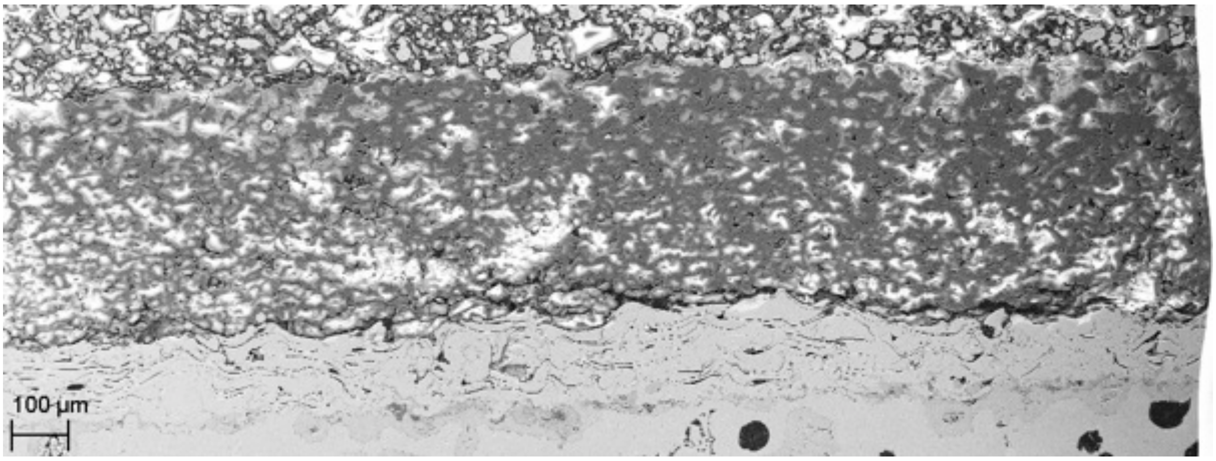

Figure 38 Mullite coated onto SiMo51 showing the increase delamination after 1000h cycling.

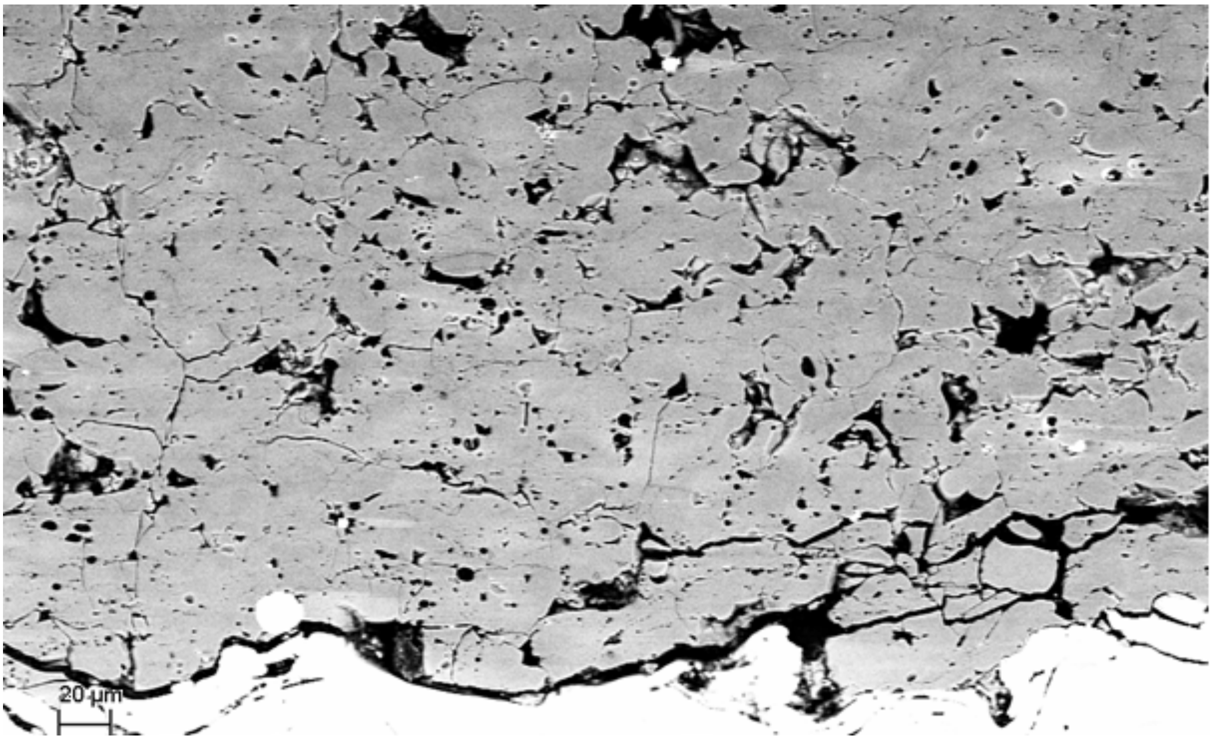

Figure 39 Cracks formed within the Mullite coating after 1000h of cycling.

After 1000h the analysis of the surface as well as of the cross-section showed that the coating had started to crack, forming long individual cracks that can be seen in Fig. 40.

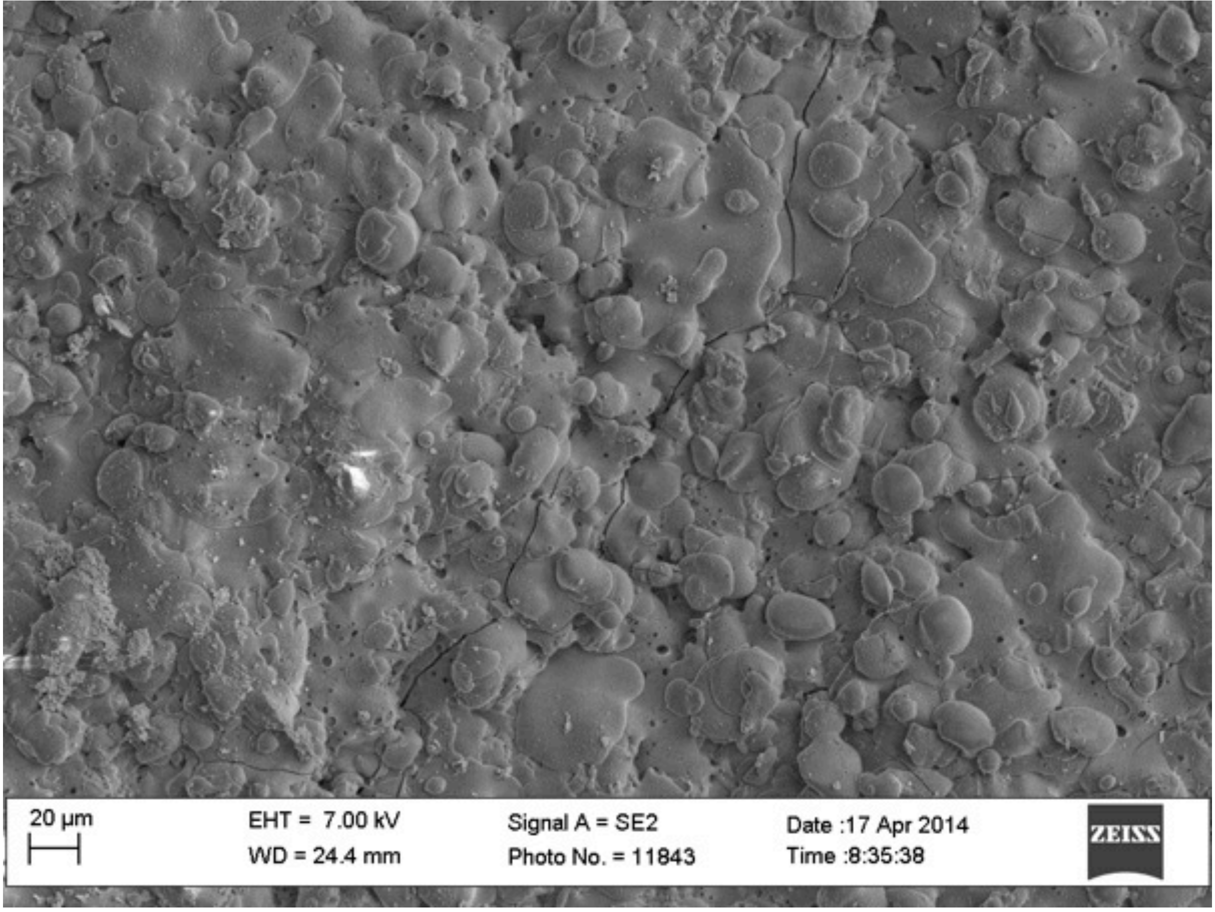

Figure 40 Surface crack after 1000h present at SiMo51 coated with Mullite.

4.7.3 Forsterite

Just as Mullite, Forsterite showed in its as coated condition a crack-free structure. After 500h, lateral cracks originating from uneven areas in the topcoat/bondcoat interface, was observed between the pores (see Fig. 41). After 1000h, these cracks had grown in size producing long lateral cracks penetrating the total thickness of the coating, which can be seen in Fig 42.

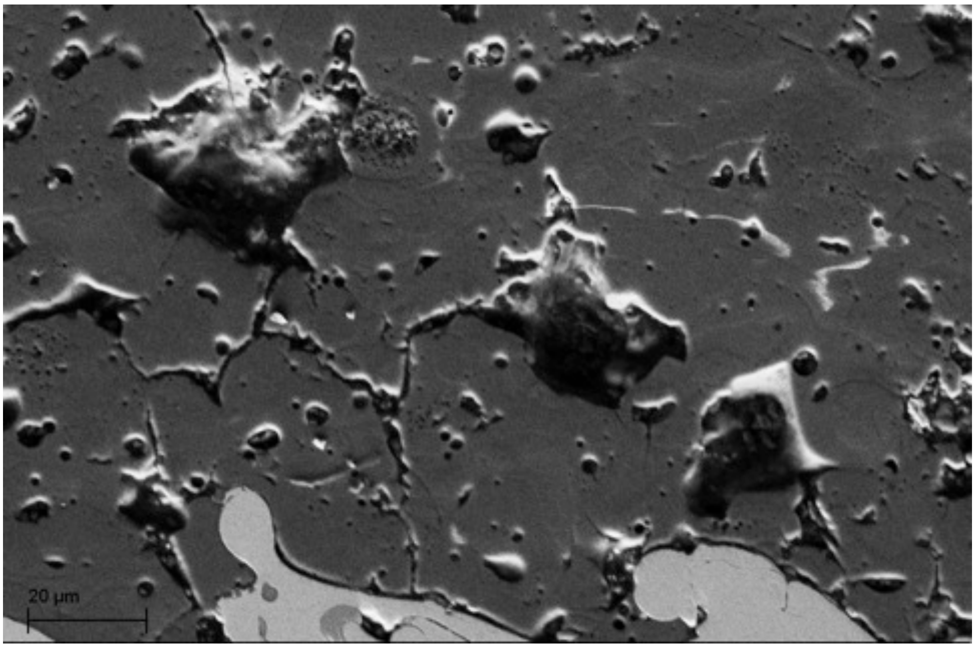

Figure 41 Forsterite coated onto HK30 showing the formation of lateral cracks after 500h cycling.

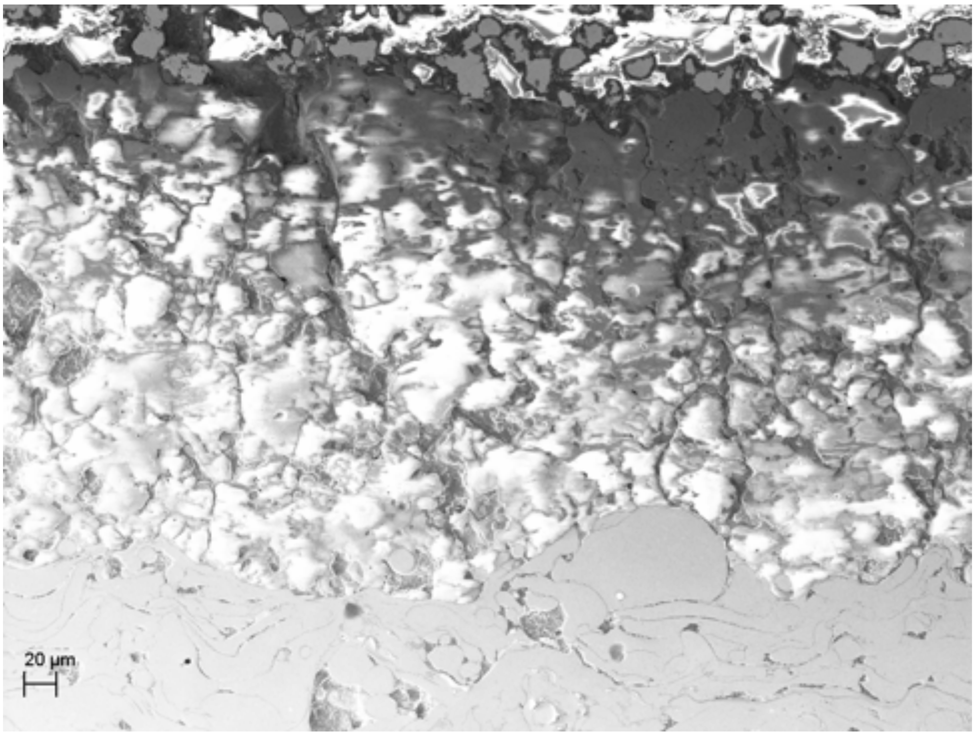

Figure 42 Large through thickness cracks present after 1000h of cycling. Picture showing Forsterite coated onto HK30.

4.7.4 8YSZ

The systems containing 8YSZ showed a starting structure of long crack parallel to the interface following the layered “splat” structure associated with the plasma spray passing’s. This structure can be seen in Fig 43.

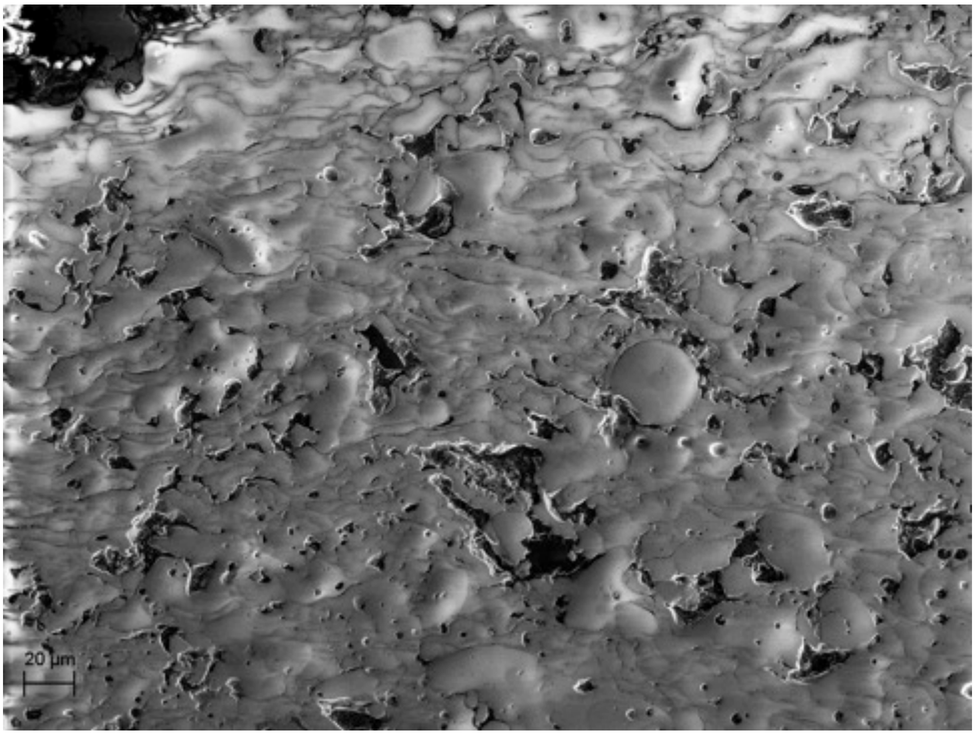

Figure 43 Starting structure of the 8YSZ coatings.

After 500h, cracks originating from the process-induced pores started to emerge, as seen in Fig. 44. The size of the induced pores was seen to increase, as can be seen in Fig. 25, resulting in an increase in porosity.

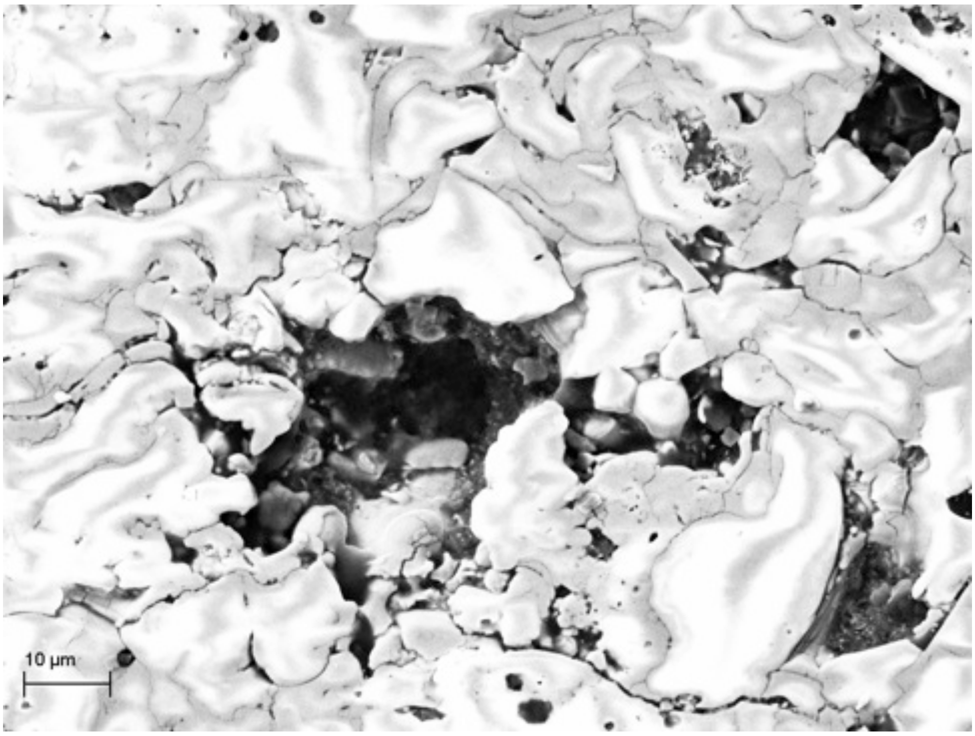

Figure 44 process induced pores with emerging cracks seen in 8YSZ coatings.

After 1000h the structure showed the same appearance as after 500h when reviewing the cross-section. The surface did, however, show an increase in surface crack width and larger cracks starting to interact with each other as can be seen in Fig. 45.

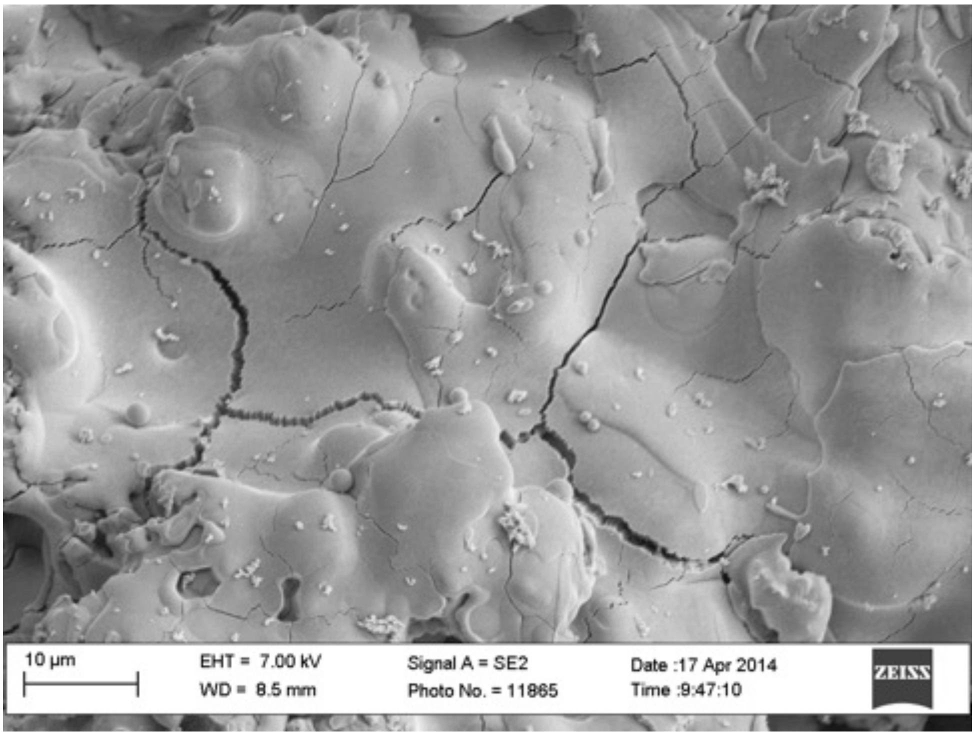

Figure 45 increased amounts of larger interacting surface cracks on 8YSZ coating onto D5S.

4.7.5 Nano sized 8YSZ

The as coated nano sized 8YSZ showed areas of “nanozones” within a matrix of conventional 8YSZ. The coating did not show long cracks running parallel to the interface within the spray layer distances as 8YSZ in the as coated condition. As seen in Fig. 46. the “nanozones” act as crack deflection zones for the process-induced cracks.

Figure 46 nano 8ysz coated onto d5s showing the coatings nanozones and micro cracked matrix.

After 500h, the “nanozones” had started to degenerate producing voids, see Fig.47. The cracks within the matrix combine the produced voids with process-induced pores, as can be seen in Fig. 48.

After the full 1000 cycles, cracks had started to emerge from uneven areas of the interface between topcoat/bondcoat as shown in Fig. 49. The figure also shows small-scale delamination emerging from the uneven areas of the interface.

Fig. 50. Shows a color change in the Zirconia based coatings that turned from white to a more yellow color during the cycling. During the cycling it was observed that 8YSZ turned more yellow compared to nano 8YSZ and $La_2Zr_2O_7$. No color change was observed for the Mullite and Forsterite coatings.

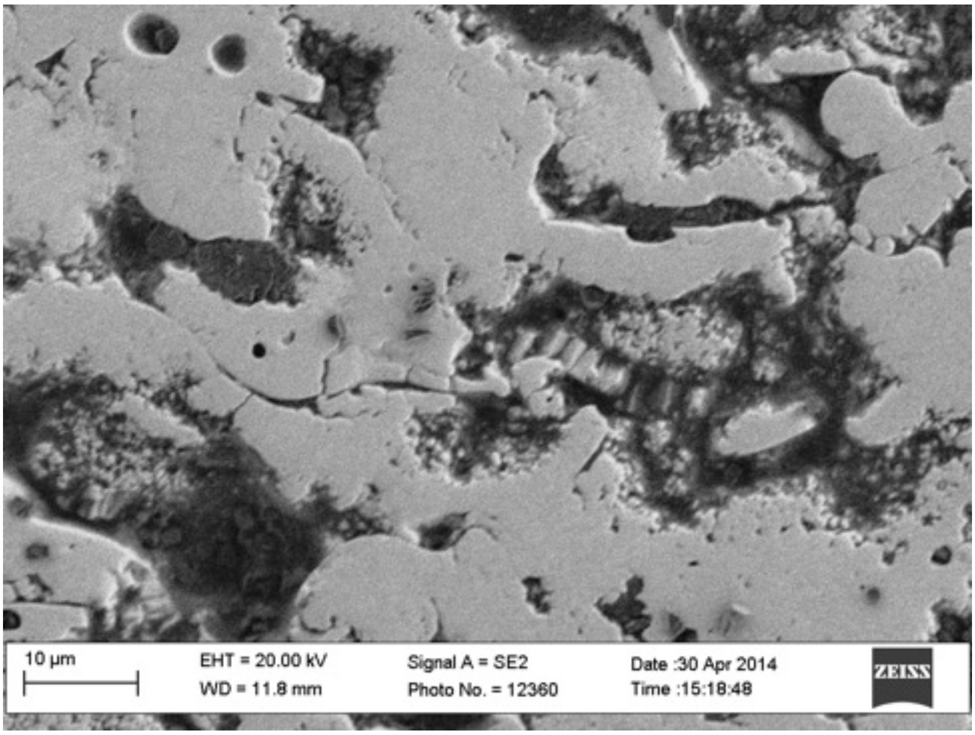

Figure 47 Nano 8YSZ coated onto D5S showing the degeneration of "nanozones".

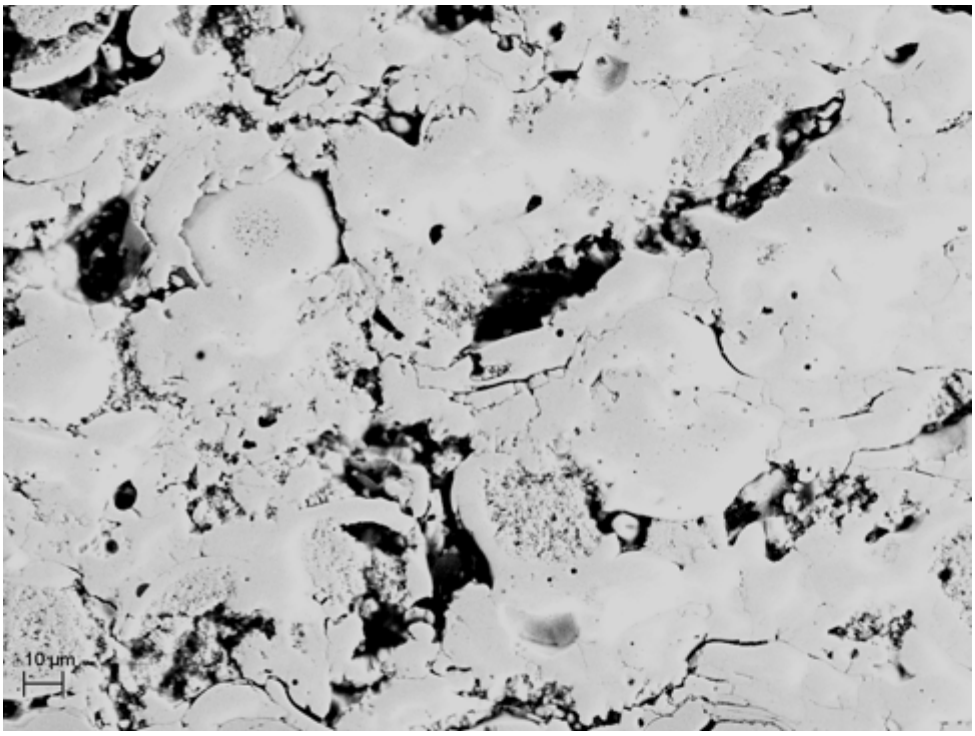

Figure 48 Cracks combining process induced pores with "nanozone" degenerated voids in Nano 8YSZ coated onto D5S

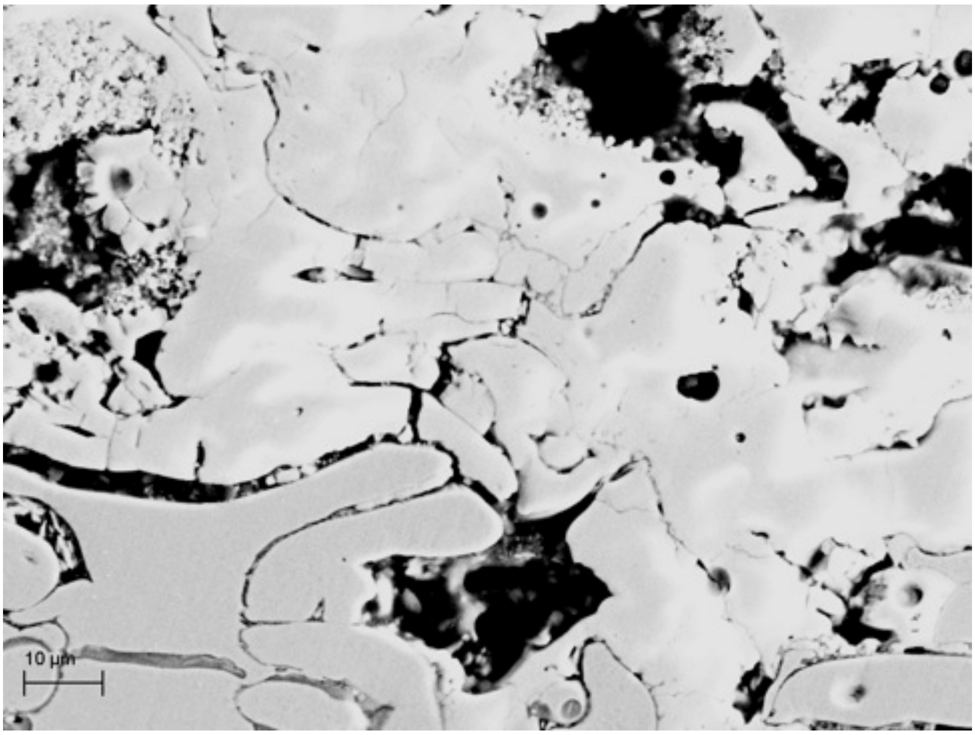

Figure 49 Small-scale delamination and crack initiations at uneven interface of the nano 8YSZ coating onto SiMo51.

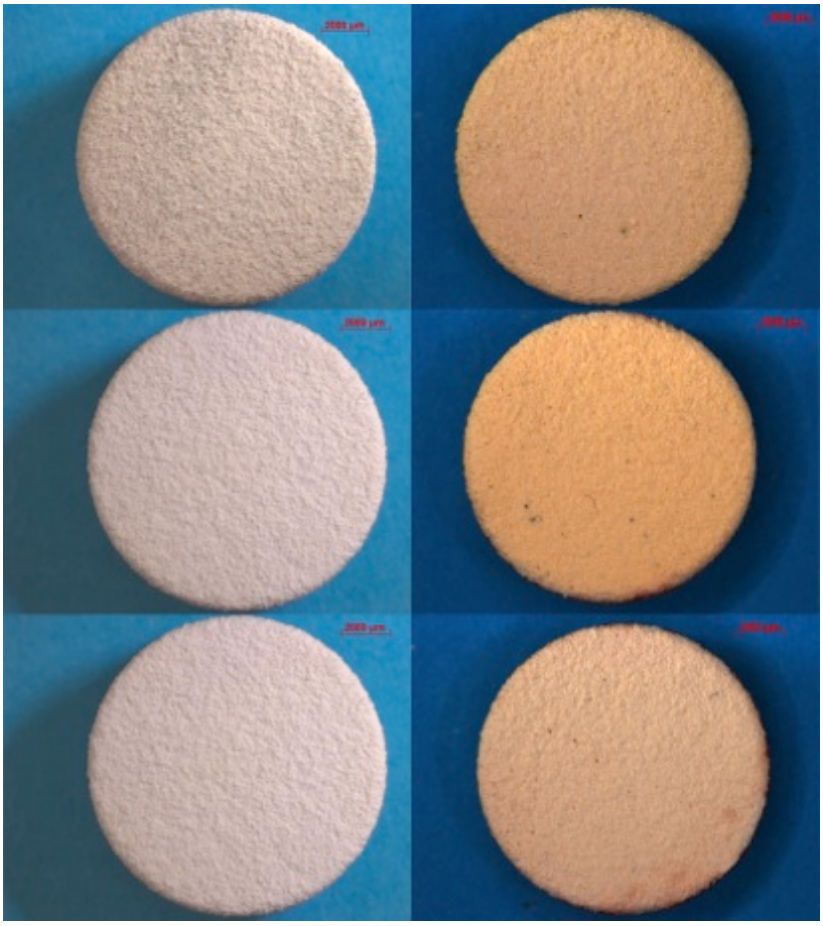

Figure 50 surface of nano 8YSZ, 8YSZ and $La_2Zr_2O_7$ in as-coated contition and after 1000h of cycling

5. Discussion

5.1 Porosity

As the results show, regarding the porosity, the Zirconia-based coatings show~~s~~ an increase in porosity over 1000h while Mullite and Forsterite show~~s~~ a relatively stable porosity level. The absence of a porosity increase for the coatings shows that none of the materials are subjected to densification within this temperature range and time. The small decrease in porosity that can be seen between 500h and 1000h (Fig. 25) is thought to be an influence of small differences in starting porosity of the samples, due to the different position during the coating process. The nano- and conventional 8YSZ should exhibit the same behaviour as $La_2Zr_2O_7$ with stabilization between 500h and 1000h. The increase in porosity seen between 0h and 500h in the zirconia-based coatings can be closely connected to the fracture toughness~~.~~

The behaviour of the Zirconia-based coatings is similar to each other and independent on the stabilizing oxide. They all present an increase in porosity between 0-500h followed by stabilization. The initial increase of porosity can be seen as the growth and interaction between already present pores and cracks. The pre-cracked structure seen in the Zirconia coatings generates a network of cracks that connects close laying pores. When the cycling is started the stresses acting on the coatings initiate a degenerating process where these cracks grow in size and interact with each other resulting in the removal of material. The rate for which this increase takes place is similar between the $La_2Zr_2O_7$ and nano 8YSZ coatings while the conventional 8YSZ shows a quicker rate of porosity increase. Both the $La_2Zr_2O_7$ and nano 8YSZ presents modes for which the crack propagation energy can be lowered compared to convention 8YSZ. In $La_2Zr_2O_7$ there is a high amount of microcracks present at the beginning and these cracks helps disperse the energy affecting the coating generating a slower growth rate compared to 8YSZ. In the nano 8YSZ case the coating is filled with so called “nanozones”, see figs 46-48, acting as strengthening phases within the coating. These areas acts as crack deflection zones generating an increase in energy input needed to connect pores to each other. The stabilization seen after 500h for all the Zirconia coatings can be understood by the coating process. The pores present in the coatings are not homogeneously distributed, generating areas of higher resp. lower porosity. When the areas of higher porosity level have been connected, the energy needed to drive cracks increases due to longer distances between pores [19].

The stability in porosity level seen in Mullite depends in high degree on the delamination seen to occur at a relatively early stage. The delamination of the coating from the bondcoat results in an increase in degrees of freedom compared to the starting position. This implies that the stress levels acting on the coating associated with the thermal cycling will decrease. Combining this with the, compared to the other four coatings, high fracture toughness of Mullite shows that the stresses affecting the coating is not high enough to initiate and drive cracks between existing pores. The same behaviour with a stable porosity level can also be seen in the Forsterite coatings. This also correlates to the failure mode and fracture toughness of the material. Forsterite is the only material seen to produce large lateral cracks running through the entire thickness of the coating. This crack behaviour generates a structure similar to coatings produced using PVD and SPS [15,19]. As stated in the theory section, these lateral cracks produce more durable coatings due to an increase in degrees of freedom producing a more flexible coating less affected by mismatches in CTE [6]. That Forsterite is the only coating that produces these kinds of coatings is an effect of the low fracture toughness it exhibits compared to the others. As seen in the pictures, the cracks are originated from unmelted particles or other imperfections at the bondcoat/topcoat interface. These imperfections introduces localized stress fields due to differences in CTE, as can be seen in Fig.52, between Forsterite and NiCrAlY exceeding K1c, during the temperature increase as well as decrease.

5.2 Hardness

Comparing the Vickers hardness, seen in Fig.27, between 0h and 1000h shows that all coatings, exhibit a decrease in hardness. The factors influencing this behaviour are many, but the main affecting factors are the chemical bond within the material, porosity level and the ability for material to maintain residual compressive stresses. In none of the cases the bonding is thought to be affected since there should be no phase transformation, as can be seen in the theory section. This implies that the hardness drop within the Forsterite coating should not be the result of any phase transformations since Forsterite transform to Enstite at temperatures above 1000^{o}C and under pressures around 15GPa [48]. Another, in this case more likely, process is that when the large lateral cracks reaches a through thickness length there is a large relive in the compressive stresses within the coating. Since hardness in brittle ceramics materials can be closely correlated to the amount of stresses present at the indentation mark [86] this relief of residual stress would generate a decrease in the coating hardness.

The small variation in hardness seen in the Mullite material, with practically constant porosity, is thought to be the effect of stress relaxation. Mullite with a melting temperature of approximately 1900^{o}C [22] could in fact exhibit small amount of creep deformation. Literature on plasma sprayed Mullite has been produced but not within the temperature range analysed here. Literature presented has, on the other hand, shown that creep can be a factor affecting the material at approximately 40% of melting temperature [22], rendering a stress relaxation of the process-induced residual stresses. As can be seen in Fig. 37-39, the delamination shown could affect both the hardness and the fracture toughness due to the increase this delamination generates, in degrees of freedom.

The increase in porosity seen in Zirconia can be closely correlated to the decrease in Hardness [86]. Once again the reduction of a material parameter shows that there are no signs of densification of the materials.

5.3 Fracture toughness

As well as the hardness studied, the fracture toughness is reduced over time. The decreasing behaviour in $K1_c$of all the coatings, seen in Fig 28, correlates to the behaviour seen in the hardness is that during the thermal cycling, the residual compressive stresses are decreased. This is the behaviour that does not present an inverted correlation between hardness and fracture toughness [86]. If the controlling factor for the increase in $K1_c$ instead would have been grain growth, an increase in $K1_c$ should have been observed together with a decrease in hardness. [86]. The likely reason should be the influence of stress relaxation during the cycling. That nano 8YSZ shows a lower fracture toughness compared to the conventional 8YSZ can only be seen as a product of poorly controlled process parameters during the coating. During the APS process of coating nano 8YSZ the powder used consists of conventional 8YSZ with nano sized 8YSZ particles within [6]. If the parameters are not correctly controlled, this will result in the complete melt of the surrounding 8YSZ while the nano 8YSZ remains unmelted or partially melted. This results in even larger residual stresses within the areas close to the “nanozones” where the energy needed to drive the crack is decreased. For nano 8YSZ to increase the fracture toughness of the material, the entire microstructure should take the form seen in the strengthening “nanozones”. The “nanozones” do act as localized strengtheners if complete melt is achieved but has little effect on the overall fracture toughness [41]. If the nano 8YSZ instead would be applied using SPS its microstructure, with finely dispersed pores [19], would generate a large increase in K_{1c}.

Another aspect, when comparing K_{1c} between the different Zirconia-based coatings, is the relatively small change dependent on the stabilizing oxide. This is mainly the result of the small amount of stabilizer used, making zirconia the driving factor when discussing strength. The stabilizer has no strengthening effect and is only used to produce a stable coating at temperatures above 670^{o}C[43]

Since both hardness and fracture toughness will be highly affected by the porosity level [86] and that the porosity is close to stable after 500 h, the largest effect of the cycling on the fracture toughness should be seen at exposure times exceeding 500 h. The affecting parameters that would lower the fracture toughness after 500h should be correlated to loss of compressive stresses due to stress relaxation.

After reviewing both the fracture toughness, hardness, and pore stability it is interesting to discuss the Mullite coating. It shows an initial hardness value close to the zirconia-based coatings but show a much more stable value over the cycling, much correlated to the stability of the porosity level. Combining this with the high fracture toughness, compared to the other coatings, this would make Mullite an interesting material to use for TBC coating if the difference in CTE could be lowered. As Fig 12 shows, Mullite as material lies closest to SiMo51 in terms of CTE but furthest away from NiCrAlY. That Mullite delaminates independent on the substrate material implies that the factor controlling the lifetime of the topcoat should be the delta CTE between topcoat and bondcoat. This is also covered in the literature where Huibin et al. [6] states that TBC lifetime are independent of the substrate CTE. On the other hand, when reviewing the above stated article, it is argued that TBC lifetime is independent on the surface roughness, which has been shown to affect the lateral cracks showed in Forsterite, Fig. 41,42. If the bondcoat were to be changed to lower delta CTE, the Mullite coating could show to be a much effective and durable material for TBC use when coating materials with lower CTE compared to NiCrAlY. But the stress lowering effect of the delamination must be remembered and evaluated further.

When it comes to the K_{1c} value after 1000h for Forsterite, the validity of this must be discussed. Due to the low fracture toughness it presents in its as-coated condition the ability to measure and evaluate the length of the crack present a problem. After 1000h the cracks no longer follow a straight line from the indentation, as can be seen in Fig. 51. The cracks instead branches of into smaller cracks or interact with the present pores. This changes the crack front geometry and following stress field generating the possibility that this value should be much lower than above stated. The length of the cracks increases with time, which is a result of the relief of the residual stresses discussed in the hardness section. The hardness decreases with lower amount of residual compressive stresses, which should mean that the cracks can travel more easily through the coating and by that decrease the fracture toughness. That the hardness does decrease and that the cracks are seen to interact with the distributed pores renders the thought that the fracture toughness is much lower than what the calculated value renders.

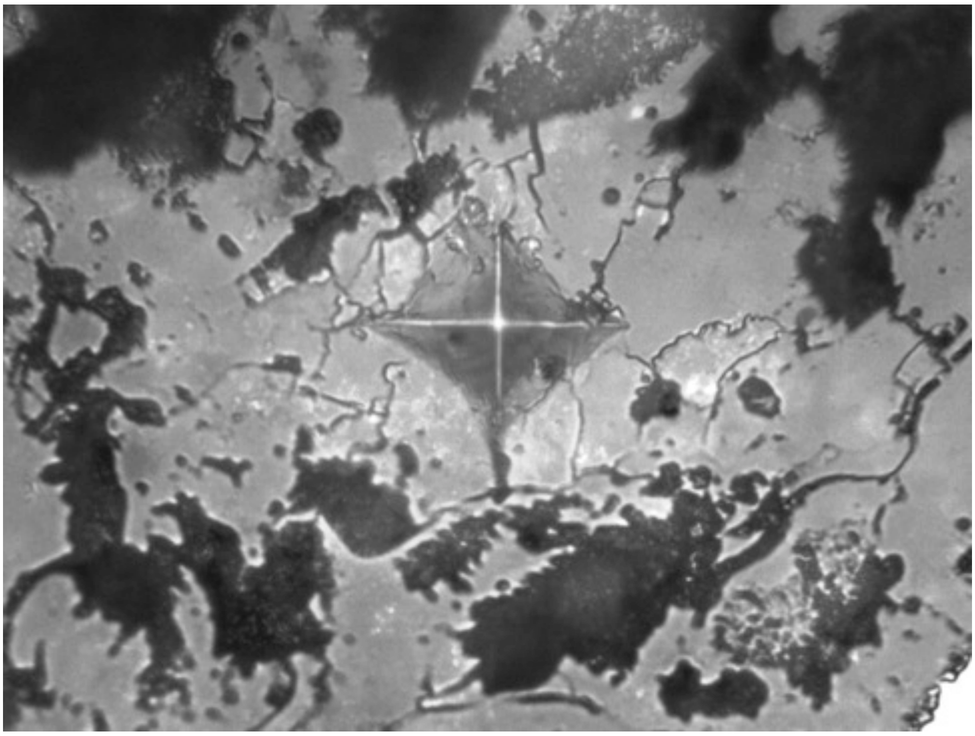

Figure 51 view of the indentation and crack formation in Forsterite.

5.4 Spallation

As the result shows none of the tested coatings show any large signs of spallation, only the $La_2Zr_2O_7$ shows micrometre sized surface spallation, see Fig 34. This is an important parameter to review due to the sensitivity of the turbo present after the manifold. There are, however, some worrying observations regarding both Forsterite and Mullite in the current system. The lateral cracks in Forsterite would have lowered the stress levels affecting the coating during cycling, but also present a factor that can make it unsuitable as TBC for manifold use. The more rapid cooling present in engine use could result in the delamination of the Forsterite topcoat from the bondcoat, due to that the cracking often take place during cooling [6] coming from the more rapid contraction of the material. The lateral crack and their influence on the hardness and subsequent effect on fracture toughness do make the coating more sensitive to the stress levels that still affects the coating within the different columns [15]. The lower fracture toughness together with the already present lateral cracks, presents the risk for large pieces, entire columns, of the topcoat to spall and damage the turbo. The same applies for the Mullite coating but in opposite order. The Mullite coating, which has shown to delaminate from the NiCrAlY, will be sensitive if the more rapid cooling generate stress levels that could drive lateral cracks. The risk for large spallation debris also increases in these two coatings when the vibrations are taken into account. The vibration amplitude measured increases the crack growth rate and should generate a more dynamic failure mode that can result in complete delamination of Mullite and Forsterite [9].

The highly cracked structure that is presented in the zirconia-based coatings is more preferred in terms of spallation, see Fig 34. The resulting debris associated with this structure is small in size (few micrometres) compared to what could be generated in Mullite and Forsterite. This should mean that the debris could pass through the manifold and into the turbo without causing severe damage or complete standstill.

5.5 Oxide Growth

None of the coatings tested show any sign of the formation of a thick TGO layer present between the topcoat and the bondcoat. When conducting an EDX analysis at the interface it shows formation of aluminium oxide but not as a continuous thick TGO layer. Since thick TGO layers are large contributors to stresses generating delamination and spallation, and the protective nature of thin Al_2O_3, the absence of thick TGO layers should generate an increase in coating lifetime, compared to Evans [57] investigation at higher temperatures, due to lower stress levels while maintaining its oxidation resistance. This is a result of the lower temperatures used combined with the slow cooling rate rendering a slower diffusion rate of aluminium in the bondcoat and slower diffusion of oxygen through the topcoat. There are, however, formation of local aluminium oxide within the bondcoat and local concentrations at the topcoat/bondcoat interface. This correlates well with earlier observations of low temperatures resulting in no visible bondcoat interface oxidation within the temperature range [2]. In the SiMo51 case, which behaves differently than the two other tested substrates, it can be seen that there are areas of iron oxide present within the NiCrAlY bondcoat. Since there's a lack of iron within the NiCrAlY alloy, the only origin for this oxide is the substrate surface. As can be seen in Fig. 31, the amount of oxygen present in the SiMo51/NiCrAlY system is higher closer to the SiMo51/NiCrAlY interface and decreases with increased distance from the interface. As the figure also reveals, the oxides are present in what used to be voids created from the different passings during the coating. There is no sign of oxidation of the bulk NiCrAlY rendering the thought that there is a thin layer of aluminium oxide capsuling the formed iron oxide. As mentioned, the aluminium oxide present in the systems is contained to process-induced voids and in many cases the thickest layer can be spotted at the interface between completely melted and unmelted particles.

The EDX results show that there is a higher concentration of aluminium oxide at the interface between topcoat/bondcoat when reviewing the samples before and after cycling. There is no thick continuous layer but the formed aluminium oxide do act as a diffusion barrier for oxygen originating from the areas above the topcoat. That this aluminium oxide layer is thin and not visible in the SEM microscope shows a slow growth rate and that the stresses associated with TGO can be neglected. The failure of the top coatings can, due to lack of thick TGO layers and a non hostile environment, be seen to be highly connected to the mismatch stresses generated by the difference in thermal expansion between bondcoat and topcoat.

When comparing the zirconia-based coatings the amount of oxygen diffusion through the coating can be seen by the coating colour [34], seen in Fig. 50. Since stabilized zirconia material consists of a high amount of oxygen vacancies, the material changes colour when oxygen diffuses through the material. The more yellow the coating turns the more oxygen diffuses through the coating. This changes the unit cell and changes the lattice by filling the oxygen vacancies. As can be seen from the pictures, the conventional 8YSZ has turned more yellow than the Nano 8YSZ, which is a result of the increased amount of grain boundaries, present in nano 8YSZ that acts as diffusion barriers. As can be seen for $La_2Zr_2O_7$ the colour has changed somewhat towards yellow but not in the same amount as the 8YSZ material. This is a combination of the stabilizing material lanthanum which in the unit cell has the same amount of free bindings as the zirconia itself, resulting in far less oxygen vacancies, making it difficult to determine the comparative diffusion based on its colour [34].

An interesting observation has also been made while examining the interface between substrate and bondcoat. The HK30 and D5S system does not appear to be affected by the thermal cycling when reviewing the interface. The interface looks unaffected with small signs of oxidations due to an uneven surface during coating. When examining the interface for the SiMo51 systems, see Fig. 31, there is a high amount of oxides formed at and around the interface. WDS and EDX analysis of the layer confirms that there are 3 different layers formed. The layer closest to the substrate is a mixed layer where there has been formation of Silicon oxide within ferritic mass rendering the darker waves within the lighter bulk material. The values seen in the quant result should be reviewed as an average value of the silicon oxide layer and the ferritic mass, this due to the small width of the oxide areas seen in the pictures and the fact that the probe drifts during the analysis making it hard to pinpoint the exact position of the spectrum. The darker layer laying on top of the mixed layer, marked 3 in the figure, consists of a both silicon oxide and iron oxide. The top layer closest to the bondcoat, marked 5 in the figure, looks from the spectrum to be iron oxide. The layered structure of the oxide with the formation of different oxides at different distances from the substrate can be correlated to the oxygen partial pressure [13]. The layered structure of Silicon and iron oxides within SiMo51 shows a behaviour seen at low oxygen partial pressure. Where the layer furthest away from the interface shows internal oxidation corresponding to the lowest partial pressure. The oxidation of the interface between substrate and interface originates from the large difference in CTE between SiMo51 and the NiCrAlY bondcoat, See Fig 52. The large difference results in small scale cracks and areas of delamination from the edges, also seen in the Mullite coating, rendering new diffusion paths for the oxygen without interacting with the oxidation barrier; Aluminium oxide, formed in NiCrAlY. This results in a poor bond between bondcoat and substrate that should result in premature failure if this setup was used. Other bondcoats are available which should lower the difference in CTE generating a more stable and durable coating. In the SiMo51 case one such bondcoat could be de ferritic FeCrAlY bondcoat.

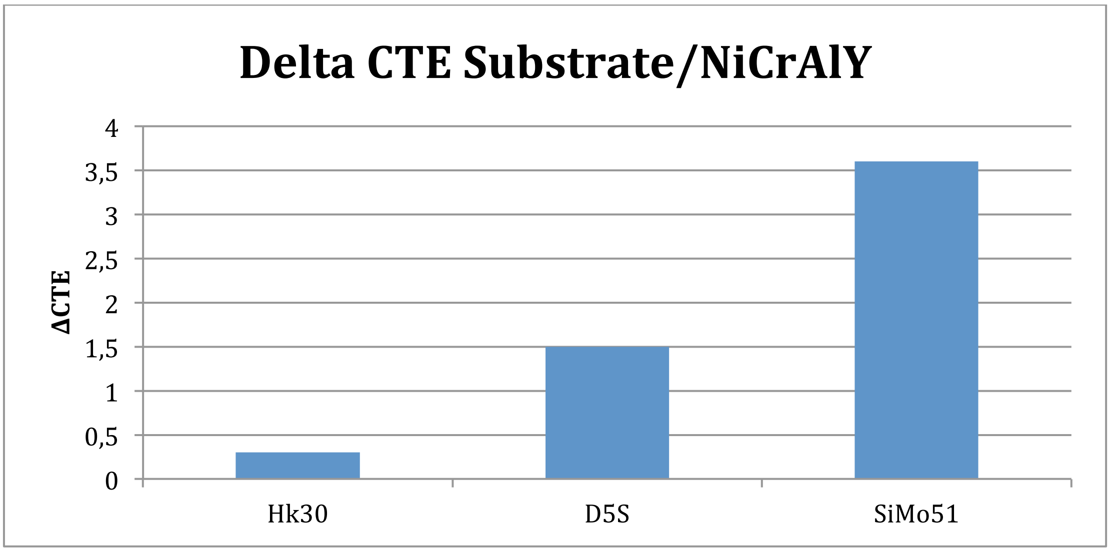

Figure 52 difference in CTE between substrate and bondcoat

5.6 Failure mode and bondcoat influence

The close similarities of the behaviour of the topcoat material between the different substrate materials do show that the mismatch stresses affecting the lifetime of the component is associated with the mismatch between bondcoat/topcoat. During this investigation no large differences between the materials that had been coated onto SiMo51 or HK30 have been spotted. This lead to the assumption that within this temperature span and the ramp rates the lifetime of a TBC topcoat is close to independent of the thermal expansion of the substrate and highly dependent on the thermal expansion of the bondcoat NiCrAlY. In the three-layered system, the stresses generated from the thermal expansion of the substrate affects the bondcoat in terms that during cooling the delamination due to mismatch CTE occurs at the interface bondcoat/substrate, as shown in Fig.52.

The surface roughness of the interface between topcoat and bondcoat has shown to affect the topcoat. In the Zirconia-based and Mullite coatings the roughness seems to increase the bonding between topcoat/bondcoat by applying to mechanical interlocking. This is most clear in the Mullite case. As Fig. 39 shows, the delamination of Mullite from NiCrAlY stops as soon as the crack fronts interact with areas containing an increased amount of unmelted particles and unevenness. In the Forsterite case, the surface roughness has the opposite effect. When reviewing the interface it can be seen that the lateral cracks present in Forsterite originates from areas where the amplitude of the surface roughness increases. This is clear when reviewing Fig. 42.

To clarify the influence of the mismatch in thermal expansion on the generated stresses, this mismatch can simplified be thought of as $\sigma = E^{*}\Delta\alpha * \Delta T$ [6]. Here it can be seen that both the difference in CTE (Fig. 53) and the effective Young's modulus is an important parameter for the duration of the coating. The stress levels are affected by the mismatch in CTE between the bondcoat and topcoat together with the effective young's modulus and temperature difference. It can be seen that the system with the highest ΔCTE is not necessarily the system affected by the highest stress, due to the influence of the effective Young's modulus.

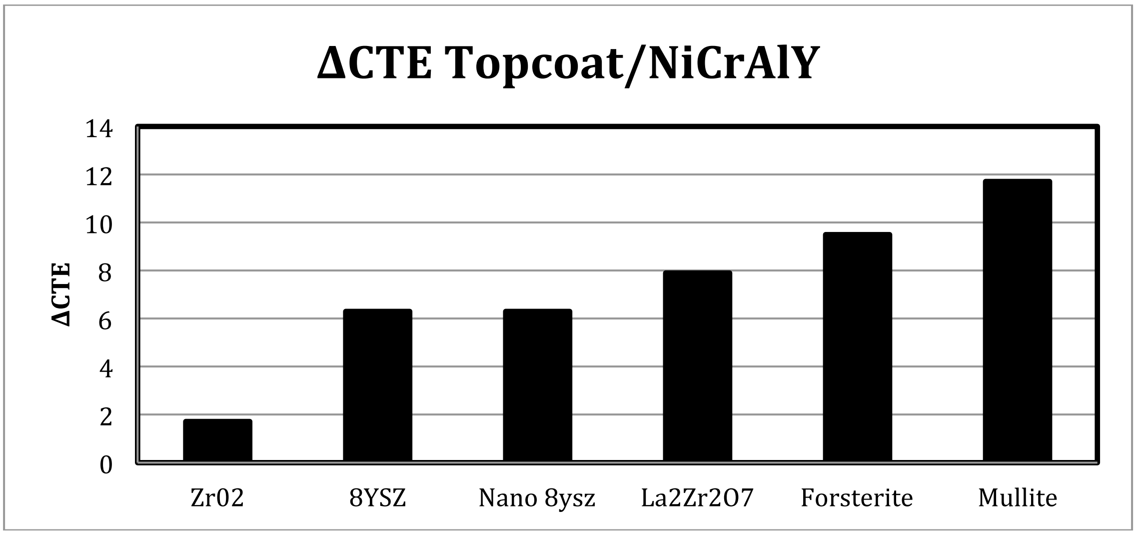

Figure 53 differences in coefficient of thermal expansion between topcoats and the NiCrAlY bondcoat.

The coating that shows the largest delamination is the Mullite coating system. Due to the large gap in CTE between Mullite and NiCrAlY, together with the relatively high effective Young's modulus, the system can be seen as none compatible. This delamination, on the other hand, can be a reason for the high fracture toughness and maintained hardness of the material. Due to the delamination the Mullite coating exhibits new degrees of freedom, being less affected by the mismatch stresses over time. The influence of the delamination on the material parameters needs to be further investigated. Since literature has shown that Mullite could work well as TBC topcoat in Diesel engines [22] Mullite should be examined with a different bondcoat. That Mullite delaminates from NiCrAlY shows that the Coating is not suitable for coating the HK30 and D5S substrate if a strain tolerant bondcoat is not used. If a bondcoat with thermal expansion coefficient closer to SiMo51 was tested the Mullite coating shows great possibility to be a good compliment to Zirconia-based coatings.

The lateral cracks in Forsterite are a consequence of the orientation of the stress levels generated at the point of origin. The unmelted particles of NiCrAlY present a stress field affecting the material above its fracture toughness that is more damaging in the temperature increase than decrease. Forsterite having the lowest fracture toughness and being crack free in in its as coated condition makes this coating the only one affected in this way. That Forsterite only presents these lateral cracks and not show any horizontal cracking is the effect of the stress relieving associated with the lateral cracks.

The pre-cracked microstructure exhibited by the zirconia-based coatings is present due to the internal mismatch stresses within the unit cell [46]. During the rapid cooling the different contraction rate within the unit cell renders a microcracked structure [53] which ispreferred in terms of spallation debris size. The Zirconia stabilized using lanthanum shows a higher amount of microcracks than the 8YSZ coatings, due to a larger internal mismatch, in the as coated condition. This structure is not only preferred in the above mentioned terms but also in terms of ability to withstand mismatch stresses. The microcracks formed are easily driven through the material due to the high porosity and low fracture toughness. During the cycling the microcracks interact with each other and forms a crack network forming these small areas of debris. The energy needed to drive the cracks is lower than the energy needed to initiate them making the cracks a good barrier for larger cracks to initiate. That the coatings crack in the horizontal direction and in connection to or in the spray layers shows that the bonding between the layers is weaker than within the different layers. The large similarities of the zirconia materials even with different stabilizing element shows that the influence of stabilizing elements is approximately the same.

5.7 Thermal conductivity

Since the main purpose of thermal barrier coatings is to protect the substrate material from the heated environment, a low value of the thermal conductivity is preferred [6]. Taking the two contributing factors into account the thermal conductivity of the TBC coating can be reduced by introducing solute cautions and/or oxygen vacancies into the lattice, decreasing the grain size and introducing larger amount of defects, i.e. pores [66]. When dealing with porous ceramic materials the gas pressure needs to be taken into account. Due to the porous structure and high gas permeability of many TBC topcoats, the pores will be filled with the surrounding gas [9]. If the pressure then increases, the heat conduction through the pores will increase, consequentially increasing the thermal conductivity of the TBC [66].

The temperature dependency of the thermal conductivity does not only link to the increased impact of radiation at higher temperatures but also to the tendency of porous coatings to undergo sintering when subjected to elevated temperatures over time [8]. The impact this process has on the conductivity is based on the densification generated by sintering, increasing the thermal conductivity. Comparing the diffusivity values, see Fig. 11, obtained from the laser flash method to tabulated data [28] it can be seen that the values acquired are lower than tabulated values. This should be an effect of the high porosity generated within these coatings now tested. As stated earlier, a higher porosity amount lowers the coatings thermal conductivity. As shown in Figs.24 and 25, the nano-sized 8YSZ and Mullite exhibited the lowest thermal conductivity relatively close to one and other. Comparing the 8YSZ between each other it can be seen that the nano-sized 8YSZ shows the lowest thermal conductivity of the two. This has much to do with the present of nanozones in the microstructure. The nanozones present in the nano 8YSZ deflects the photons within these areas lowering the conductivity within the coating. [28]

The thermal diffusivity and conductivity seen in Forsterite cannot be fully trusted. In earlier reports [28] Forsterite showed an initial thermal conductivity of 8 W/mK and then a decrease towards the same values for 8YSZ. That step decrease seen in Forsterite values is thought to be the result of a malfunction of the analysis program during the testing of Forsterite and $La_2Zr_2O_7$. For a yet unknown reason during these two sample testing's the generated curve followed a close enough behavior as earlier reported but higher values. The standard deviation during these two tests showed in some cases above 100% for $La_2Zr_2O_7$ hence these values are not presented.

5.8 Influence of environmental, processing and loading parameters

This examination shows the behaviour of the coatings in laboratory air and at slow cooling rate, in exhaust applications the degenerating effect of Na, S and other chemicals present in the exhaust gasses needs to be taken into account. This should deplete much of the stabilizing elements in the zirconia based coatings resulting in the ability of the ZrO_2 to phase transform [56] at temperatures within the cycling range. If the coatings are used in a Sulphate-rich environment, coast- or marine application, the $La_2Zr_2O_7$ coating is a poor choice due to the depletion of the stabilizing Lanthanum. The Mullite and Forsterite coatings should as seen in the theory section be stable within this range and no large effect of the hostile environment should be noted. However, there is one critical damaging effect that needs to be investigated for all the coatings, water [6]. Due to the high porosity of the topcoat water present in the exhaust have an easy path to penetrate into the material. The penetration of water into the material will have a large impact on the expected lifetime of the coating. The quick temperature differences associated with the exhaust flow generates a high expansion of the water as it phase transform, resulting in high stresses affecting the coatings from within exhaust applications the $La_2Zr_2O_7$ coating a worse choice for applications in sulphate-containing atmospheres, i.e. in coast- or marine applications.

5.9 TBC Structure design

For a TBC system to work well within this application the structure that would be the most promising, after reviewing the results achieved and literature survey, can summarized as follow:

- Dense outermost surface shielding from absorption of foreign particles and wear
- Highly porous middle part to lower thermal conductivity
- Dense material close to bondcoat to increase bonding.
- Vertical through thickness cracks generating a coating more sustainable in terms of mismatch stresses
- Small and finely distributed pores generating a more durable and more homogeneous coating.

For application on the outside of the manifold this can be achieved by using the Suspension plasma spray process using nano-sized pores [19] while in the internal case, according to literature these structure can be achieved using the Sol-Gel process with application of multilayer coatings [23]

5.10 Application method

To be successful as a thermal barrier coating the ideal system is coated on the inside of the manifold to decrease the substrate temperature as well as shielding the surrounding. Due to the geometry and dimensions of the manifold the widely used APS process cannot be applied in the conventional way. The same goes for every one of the line of sight processes studied in this thesis, but for different reasons. PVD and the none line of sight method developed, DVD, has its limitations in terms of the thickness that can be generated within reasonable costs [15,21]. SPS as a coating have shown to produce well defined and homogeneous coatings [19] but is still, due to the line of sight process a none applicable method for internal coating of exhaust manifolds. The non line of sight coating process slurry coating has in literature [17] shown to produce durable and cost effective coatings at complex geometries, but do require a heat treatment which operate above the limit for phase transformations of the substrates intended. The influence that this heat treatment has on the substrate in terms of loss of structural strength and oxidation resistance [13] can not be overcome by the application of a thermal barrier coating, making the slurry, as seen today, a poor choice for this application.

The Sol-Gel process with its low temperature heat treatment does not affect the mechanical properties of the substrates and has shown to produce durable coatings. This method due to its simplicity, cost effectiveness and small influence on the substrates properties [23] is a method well suited for the application of internal zirconia TBC coatings. The obstacle to overcome before applying Sol-Gel coatings internally is the optimisation of withdrawal speed [24]. The fact that Sol-Gel generates a structure much like APS does make it interesting to produce samples and compare the results between the two. The dipping process also presents the possibility to achieve the desired structure of the coatings described above by using multiple baths.

5.11 Cycling procedure and Analysis methods

Another parameter needs to be covered, the cooling rate. During this cycling the environment has a cooling rate of about 6^{o}C/min. when the engine cell tests are conducted this rate is much faster and due to that the cooling generates the stresses when the coatings crack this more rapid cooling will result in larger stresses which could crack the coatings even earlier. At a higher cooling rate the effects of the as coated condition cracked structure will have even large impact on the stress relaxation.

Fracture toughness for ceramic material is a property hard to determine. Due to their brittle nature and the residual stresses curtsey of the APS method, there is a possibility that the measured crack length will be affected by the crack tip mode as well, which can result in error regarding their length. The mathematically decided alpha parameter, which is a fitting parameter, does have variations that can be up to 25%, which shows another margin of error.
This is largely the problem with the result for Forsterite. Where the material is too weak in terms of fracture toughness resulting in that the cracks reach into pores that swallows the cracks. This means that the cracks measured in many cases should be longer. When the crack reaches the pores the pores themselves becomes the crack tip creating a much more blunt tip where more energy is needed to drive the crack forward.

Undoubtedly, the difficulty of measuring the cracks presents a problem since the cracks needs to be almost straight to get an accurate measurement [86]. But due to the residual stresses present in the coating, the cracks almost exclusively started to bend. The crack length was then measured as a trend line. Since the object here is to evaluate coating that has been applied using APS. The fact that Vickers indentation Fracture toughness is dependent of the residual stresses is something that generates values that can be used as comparison between the materials if applied using APS. If another process is used the result might look different. The Vickers Indentation method was used since the determination using bend testing was not applicable on the already coated materials.

Porosity measurements are done using an image analysis and the results can vary depending on the observer. The ideal way to decide the porosity would be to apply the coating on top of a dissolvent substrate and use the Archimedes principle to determine both the density and porosity.

The effect of the temperature ramp range should be that the tested systems are not affected in the same way as should be in the manifold, since most of the systems fail during cooling the cooling rate needs to be quicker to try this accurately.

The effect of the sample geometry and areas affected in high temperature regimes should be noted. When systems are applied internally the main effect will the decreased temperature of the substrate. Meaning that different temperatures will affect the substrate and coating that should generate lower stress levels at the interface since the metallic bondcoat will produce a smaller thermal expansion.

6. Further work

The influence of the hostile environment and the degenerative effect this has on the investigated materials needs to be tested and understood. To verify the results of the TBC system containing Mullite, investigation of Mullite should be tested together with a bondcoat with lower thermal expansion. To be able to fully achieve the potential of the thermal barrier coatings, samples of the internal coating process Sol-Gel should be tested to investigate their performance in exhaust applications with the influence of vibrations and hostile environment.

7. Conclusion

Combining the overall results from the different analyses after thermal cycling the TBC system most suitable for use in exhaust manifold application, in their tested state, is the conventional 8YSZ. La2Zr2O7 systems show similar results but due to lack of data regarding the thermal conductivity no conclusion can be drawn. Mullite shows the best performance in maintaining its properties but needs to be evaluated further with different bondcoats to lower the thermal mismatch stresses to verify its stability. Forsterite shows poor hardness, fracture toughness and the highest thermal conductivity, generating a system that cannot be seen as suitable for exhaust applications. It was observed that the Zirconia based coatings generated smaller sizes spallation debris due to their initial microcracked structured. Making the debris less damaging to the turbo compared to the sized that Mullite and Forsterite could generate. It was concluded that when coating SiMo51, the type of bond coat plays an important role and lowering the CTE mismatch between the TBC and the bond coat by selecting a ferritic bond coat could reduces the oxidation effect observed in this study.

8. References

(1) Beardsley MB, Happoldt PG, Kelley KC, Rejda EF, Socie DF. *Thermal Barrier Coatings for Low Emission, High Efficiency Diesel Engine Applications*. Government/Industry Meeting, Washington, DC (US), 04/26/1999--04/28/1999; 1999-04-26; United States: Caterpillar, Inc. (US); 1999.

(2) Yonushonis TM. *Overview of thermal barrier coatings in diesel engines*. Journal of Thermal Spray Technology 1997;6(1):50-56.

(3) Ciniviz M, Salman MS, Canli E, Köse H, Solmaz Ö. *Ceramic Coating Applications and Research Fields for Internal Combustion Engines*. 2012; Available at: http://www.intechopen.com/books/ceramic-coatings-applications-in-engineering/ceramic-coating-applications-and-research-fields-for-internal-combustion-engines. Accessed 01/20, 2014.

(4) Vassen R, Jarligo MO, Steinke T, Mack DE, Stöver D. *Overview on advanced thermal barrier coatings*. Surface and Coatings Technology 2010;205(4):938-942.

(5) Parker WD. *Thermal barrier coatings for gas turbines, automotive engines and diesel equipment*. Materials & Design 1992;13(6):345-351.

(6) Huibin X, Hongbo G. *Thermal barrier coatings*. 1st ed. Cambridge: Woodhead Publishing Limited; 2011.

(7) Schlichting KW, Padture NP, Jordan EH, Gell M. *Failure modes in plasma-sprayed thermal barrier coatings*. Materials Science and Engineering: A 2003;342(1-2):120-130.

(8) Mogro-Camperoa A, Johnsona CA, Bednarczyka PJ, Dinwiddieb RB, Wangb H. *Effect of gas pressure on thermal conductivity of zirconia thermal barrier coatings*. Surface and Coatings Technology 1997;94-95:102-105.

(9) Wesling KF, Socie DF, Deardsley B. *Fatigue of Thick Thermal Barrier Coatings*. Journal of the American Ceramic Society 1994;77(7):1863-1868.

(10) Li D, Perrin R, Burger G, McFarlan D. *Advances in Lightweight Automotive Castings and Wrought Aluminum Alloys*. 1st ed. Detroit, Michigan: Society of Automotive Engineers, Incorporated; 2004.

(11) Covert R. *Properties and Applications of Ni-Resist and Ductile Ni-Resist Alloys*. 2008; Available at: http://www.nickelinstitute.org/~/Media/Files/TechnicalLiterature/PropertiesandApplicationsofNi_ResistandDuctileNi_ResistAlloys_11018_.pdf

(13) M. Ekström. *DEVELOPMENT OF A FERRITIC DUCTILE CAST IRON FOR INCREASED LIFE IN EXHAUST APPLICATIONS*. Stockholm, Sweden: Royal Institute of Technology; 2013.

(14) Babakr AM, Al-Ahmari A, Al-Jumayiah K, Habiby F. *Sigma Phase Formation and Embrittlement of Cast Iron-Chromium-Nickel (Fe-Cr-Ni) Alloys*. Journal of Minerals & Materials Characterization & Engineering 2008;7(2):127-145. Accessed 02/10, 2014.

(15) Bach FW, Laarmann A, Wenz T. *Moderns surface technology.* 1st ed. Weinheim: Wiley- VCH; 2006.

(16) Brinker CJ, Frye GC, Hurd AJ, Ashley CS. *Fundamentals of sol-gel dip coating*. Thin Solid Films 1991;201(1):97-108.

(17) Nguyen P, Harding S, Ho SY, editors. *Experimental Studies on Slurry Based Thermal Barrier Coatings*. 5th *Australasian Congress on Applied Mechanics*; 10-12 December; Brisbane, Australia: Australasian Congress on Applied Mechanics; 2007.

(18) Almedia DS, Et a. *Electron Beam-Physical Vapour Deposition of Zirconia Co-Doped with Yttria and Niobia*. Materials Science Forum 2005;498-499:453-458.

(19) Curry. N. *Design of Thermal Barrier Coatings* . Trollhättan, Sweden: University West; 2014.

(20) Tarasi F, Et a. *Effective Parameters in Axial Injection Suspension Plasma Spray Process of alumina-zirconia ceramics*. Journal of Thermal Spray Technology 2008;17(5-6):685-691.

(21) J. F. Groves. *Directed Vapor deposition.* Virginia: School of Engineering and Applied Science; 1998.

(22) Schneider H, Komarneni S. *Mullite*. 1st ed. Weinheim: Wiley-VCH; 2005.

(23) Barrow DA, Petroff TE, Sayer M. *Thick ceramic coatings using a sol gel based ceramic-ceramic 0–3 composite*. Surface and Coatings Technology 1995;76-77(1):113-118.

(24) Sniezewski J, Et a. *Sol–gel thermal barrier coatings: Optimization of the manufacturing route and durability under cyclic oxidation*. Surface and Coatings Technology 2010;205(5):1256-1261.

(25) Qiuli C, Hongbo G, Shengkai G, Huibin X. *Novel microstructure of EB-PVD double ceramic layered thermal barrier coatings*, Thin Solid Films, 2008;516(16): 5736-5739

(26) Sampath S, Et a. *Role of thermal spray processing method on the microstructure, residual stress and properties of coatings: an integrated study for Ni–5 wt.%Al bond coats*. Materials Science and Engineering: A 2004;364(1-2):216-231.

(27) Gong S, Van Every S, Wang H, Trice RW. *Microstructure and thermal properties of inflight rare-earth doped thermal barriers prepared by suspension plasma spray*, Journal of the European Ceramic Society, 2014;34(5): 1243-1253

(28) Klemens PG, Gell M. *Thermal conductivity of thermal barrier coatings*. Materials Science and Engineering: A 1998;245(2):143-149

(29) Litovsky EY, Shapiro M. *Gas Pressure and Temperature Dependences of Thermal Conductivity of Porous Ceramic Materials: Part 1, Refractories and Ceramics with Porosity below 30%.* Journal of the American Ceramic Society 1992;75(12):3425-3439.

(30) Litovsky EY, Shapiro M, Shavit A. *Gas Pressure and Temperature Dependences of Thermal Conductivity of Porous Ceramic Materials: Part 2, Refractories and Ceramics with Porosity Exceeding 30%.* Journal of the American Ceramic Society 1996;79(5):1366-1377.

(31) Gaskell DR. *Introduction to the Thermodynamics of Materials*, Fifth edition . 5th ed. New York: Taylor & Francis group, LLc; 2008.

(32) Winters MR, Clarke DR. *Thermal conductivity of yttria-stabilized zirconia–hafnia solid solutions*. Acta Materialia 2006;54(19):5051-5059.

(33) Nakamura T, Qian G, Berndt CC. *Effects of Pores on Mechanical Properties of Plasma-Sprayed Ceramic Coatings*. Journal of the American Ceramic Society 2000;83(3):578-584.

(34) Wright PK, Evans AG. *Mechanisms governing the performance of thermal barrier coatings*. Current Opinion in Solid State and Materials Science 1999;4(3):255-265.

(35) Siebert B, Funke C, Vassen R, Stover D. *Changes in porosity and Young's Modulus due to sintering of plasma sprayed thermal barrier coatings*. Journal of Materials Processing Technology 1999;92-93(7):217-223.

(36) Shrirao PN, Pawar AN. *Evaluation of Performance and Emission characteristics of Turbocharged Diesel Engine with Mullite as Thermal Barrier Coating.* International Journal of Engineering and Technology 2011;3(3):256-262.

(37) Hildmann B, Schneider H. *Heat Capacity of Mullite - New Data and Evidence for a High-Temperature Phase Transformation*. Journal of the American Ceramic Society 2004;87(2):227-234.

(38) Kleebe, F. Siegelin, T. Straubinger, G. Ziegler. *Conversion of Al2O3–SiO2 powder mixtures to 3:2 mullite following the stable or metastable phase diagram*, Journal of the European Ceramic Society, 2001:21(14):2521-2533

(39) Scott, H.G. *Phase relationships in the zirconia-yttria system*. Journal of Materials Science 1975;10(9): 1527-1535

(40) Witz G, Et a. *Phase Evolution in Yttria-Stabilized Zirconia Thermal Barrier Coatings Studied by Rietveld Refinement of X-Ray Powder Diffraction Patterns*. Journal of the American Ceramic Society 2007;90(9):2935-2940.

(41) Cao XQ, Vassen R, Stoever D. *Ceramic materials for thermal barrier coatings*. Journal of the European Ceramic Society 2004;24(1):1-10.

(42) Kutz M. *Handbook of Environmental Degradation of Materials*. 1st ed. New York: William Andrew, Inc; 2005.

(43) Afrasiabia A, Saremi M, Kobayashi A. *A comparative study on hot corrosion resistance of three types of thermal barrier coatings: YSZ, YSZ +* Al_2O_3 *and YSZ/*Al_2O_3. Materials Science and Engineering: A 2008;478(1-2):264-269.

(44) Liu B, Wang JY, Zhou YC, Liao T, Li FZ. *Theoretical elastic stiffness, structure stability and thermal conductivity of La2Zr2O7 pyrochlore*. Acta Materialia 2007;55(9):2949-2957.

(45) Cao XQ, Vassen R, Jungen W, Schwartz S, Tietz F, Stöver D. *Thermal Stability of Lanthanum Zirconate Plasma-Sprayed Coating*. Journal of the American Ceramic Society 2001;84(9):2086-2090.

(46) mishra SK, Et a. *Microstructural studies on EB-PVD deposited NiCrAlY, YSZ and lanthanum zirconate for thermal barrier applications*. Surface and Coatings Technology 2012;207(1):143-148.

(47) Gasparik T. *Phase diagrams for geoscientists: An atlas of the earth's interior*. 1st ed. Würzburg: Springer-Verlag Berlin; 2003.

(48) Hazen RM. *Effects of temperature and pressure on crystal structure of forsterite*. American Mineralogist 1976;61:1280-1293.

(49) Bouhifd MA, Andrault D, Fiquet G, Richet P. *Thermal expansion of forsterite up to the melting point*. Geophysical Research Letters 1996;23(10):1143-1146.

(50) Farver JR, Yund RA, Rubie DC. *Magnesium grain boundary diffusion in forsterite aggregates at 1000°–1300°C and 0.1 MPa to 10 GP*. Journal of Geophysical Research: Solid Earth 1994;99(B10):19809-19819.

(51) Tromans D, Meech JA. *Fracture toughness and surface energies of minerals: theoretical estimates for oxides, sulphides, silicates and halides*. Minerals Engineering 2002;15(12):1027-1041.

(52) keyvani A, Saremi M, Heydarzadeh Sohi M, Valefi Z. *A comparison on thermomechanical properties of plasma-sprayed conventional and nanostructured YSZ TBC coatings in thermal cycling*. Journal of Alloys and Compounds 2012;541(1):488-494.

(53) Racek O, Berndt CC, Guru DN, Heberlein J. *Nanostructured and conventional YSZ coatings deposited using APS and TTPR techniques*. Surface and Coatings Technology 2006;201(1-2):338-346.

(54) Matejiceka J, Sampatha S, Gilmoreb D, Neiser R. *In situ measurement of residual stresses and elastic moduli in thermal sprayed coatings: Part 2: processing effects on properties of Mo coatings.* Acta Materialia 2003;51(3):873-885.

(55) Lima RS, Marple BR. *Nanostructured YSZ thermal barrier coatings engineered to counteract sintering effects*. Materials Science and Engineering: A 2008;485(1-2):182-193.

(56) Kutz M. *Handbook of Environmental Degradation of Materials*. 1st ed. New York: William Andrew, Inc; 2005.

(57) Rabiei A, Evans AG. *Failure mechanisms associated with the thermally grown oxide in plasma-sprayed thermal barrier coatings*. Acta Materialia 2000;48(15):3963-3976.

(58) Clarke, D.R, Levi, C.G. *MATERIALS DESIGN FOR THE NEXT GENERATION THERMAL BARRIER COATINGS*. Annual Review of Materials Research 2003;33: 383-417.

(59) Schlichting. K, Et.Al. *Failure modes in plasma-sprayed thermal barrier coatings*, Materials Science and Engineering: A, 2003;342(1-2):120-130

(60) Rösler J, Bäker M, Aufzug K. *A parametric study of the stress state of thermal barrier coatings: Part I: creep relaxation.* Acta Materialia 2004;52(16):4809-4817.

(61) Rösler J, Bäker M, Volgmann M. *Stress state and failure mechanisms of thermal barrier coatings: role of creep in thermally grown oxide.* Acta Materialia 2001;49(18):3659-3670.

(62) Afrasiabi A, Saremi M, Kobayashi A. *A comparative study on hot corrosion resistance of three types of thermal barrier coatings: YSZ, YSZ +* Al_2O_3 *and YSZ/*Al_2O_3. Materials Science and Engineering: A 2008;478(1-2):264-269.

(63) Afrasiabi A, Kobayashi A. *Hot corrosion control in plasma sprayed YSZ coating by alumina layer with evaluation of microstrcuture and nanoindentation data (H, E)*. Vacuum 2013;88(1):103-107.

(64) Rapp RA, Zhang YS. *Hot corrosion of materials: Fundamental studies*. JOM 1994;46(12):47-55.

(65) Marple BR, Nagy DR, Vassen R, Voyer J, Thibodeau M. *Hot Corrosion of Lanthanum Zirconate and Partially Stabilized Zirconia Thermal Barrier Coatings.* journal of Engineering for Gas Turbines and Power 2004;128(1):144-152.

(66) Vassen R, Cao XQ, Tietz F, Basu D, Stöver D. *Zirconates as New Materials for Thermal Barrier Coatings*. Journal of the American Ceramic Society 2004;83(8):2023-2028.

(67) Kobayashi A, Ando Y, editors. *High Heat Resistant Coatings by Means of Gas Tunnel Type Plasma Spraying* . 32nd International Electric Propulsion Conference ; 11-15 September; Wiesbaden: Ashikaga Institute of Technology; 2011.

(68) Takahashi J, Kawai Y, Shimada S. *Hot corrosion of cordierite/mullite composites by Na-salts.* Journal of the European Ceramic Society 2002;22(12):1959-1969.

(69) Takahashi J, Kawai Y, Shimada S. *Hot corrosion of cordierite ceramics by Na- and K-salts*. Journal of the European Ceramic Society 1998;18(8):1121-1129.

(70) Bose S. *High Temperature Coatings*. 1st ed. Oxford: Elsevier Inc; 2007.

(71)Iguchi. C, dos Santos. W, Gregorio. R, *Determination of thermal properties of pyroelectric polymers, copolymers and blends by the laser flash technique*, Polymer Testing, 2007;26(6): 788-792

(72) Altun Q, Boke YE, Kalemtas A. Problems for determining the thermal conductivity of TBCs by laser-flash method. Journal of Achievements in materials and manufacturing engineering 2008;20(2):115-120.

(73) Deshpande S, Kulkarni A, Sampath S, Herman H. Application of image analysis for characterization of porosity in thermal spray coatings and correlation with small angle neutron scattering. Surface and Coatings Technology 2004;187(1):6-16.

(74) Huff MA. Mullite (3Al2O3 2SiO2). 2013; Available at: https://www.memsnet.org/material/mullite3al2o32sio2bulk/. Accessed 03/10, 2014.

(75) Birle JD, Gibbs GV, Moore PB, Smith JV. *Crystal structures of natural olivines*. American Mineralogist 1968;53(1):807-824.

(76) Nguyen Q. Ceramic Fuel Cells. Journal of the American Ceramic Society 2005;76(3):563-588.

(77) Zhou H, Et a.
Preparation and thermophysical properties of CeO2 doped La2Zr2O7 ceramic for thermal barrier coatings. Journal of Alloys and Compounds 2007;438(1):217-221.

(78) Keller T, Et a, editors. CHARACTERIZATION OF ANISOTROPIC, THERMALLY SPRAYEDMICROSTRUCTURES USING SMALL-ANGLE NEUTRON SCATTERING Materials Structure & Micromechanics of Fracture 3 ; June 27 – 29, 2001; Brno, Czech Republic; 2001.

(79) Leitner J, Et a. Estimation of Specific heat capacities of solid mixed oxides. Thermochimica Acta 2003;395(1):27-46.

(80) Qiu L, White M.A. The constituent additive method to estimate heat capacities of complex inorganic solids. Journal of Chemical education 2001;78(8):1076-1079.

(81) Indiana Univeristy. STANDARD THERMODYNAMIC PROPERTIES OF CHEMICAL SUBSTANCES 2005; Available at: http://courses.chem.indiana.edu/c360/documents/thermodynamicdata.pdf. Accessed 02-18, 2014.

(82) Moskal G, editor. Characteristics of selected thermal properties of 8YSZ type powders produced with different methods Mo. 11th Europhysical Conference on Defects in Insulating Materials (EURODIM 2010); 12-16 July 2010; Online: IOP Science; 2010.

(83) Robie R.A, Hemingway B.S. Heat capacities and entropies of Mg2SiO4, Mn2SiO4, and Co2SiO4 between 5 and 380 K. American Mineralogist 1982;67(1):470-482.

(84) Sulzer M. Material Product Data Sheet 7 - 8% Yttria Stabilized Zirconia Spray-Dried Powder. 2013; Available at: www.sulzer.com/en/-/media/Documents/ProductsAndServices/Coating_Materials/Thermal_Spray/ProductInformation/Ceramics_Zirconium_Oxide/DSMTS_0019_1_8YOZrOAgglom.pdf Sulzer sheet 8YSZ. Accessed 03-05, 2014.

(85) Broberg P, Runnemalm A, editors. Detection of Surface Cracks in Welds using Active Thermography, 18th World Conference on Nondestructive Testing,; 16-20 April; Durban, South Africa: NDT; 2012.

(86) Kruzic. J.J, Kim. K.J, Koester. R.O, Ritchie. R.O. Indentation techniques for evaluating the fracture toughness of biomaterials and hard tissues. Journal of the mechanical behaviour of biomedical materials 2 2009: 384-395.

(87) Memsnet. Material Mullite (bulk). 2013: Available at:
https://www.memsnet.org/material/mullite3al2o32sio2bulk/

(88) Kyocera material characteristics, 2014: Available at:
http://americas.kyocera.com/kicc/pdf/Kyocera_Material_Characteristics.pdf

(89) Liu. B, Wang. J. *Theoretical elastic stiffness, structure stability and thermal conductivity of La 2Zr 2O 7 pyrochlore*. Acta Materialia 2010:58(12);4369-4377.

(90) Singh. P, Narottam. P.B, *Advances in solid Oxide fuel cells IV.* Ceramic engineering and Science Proceedings 2008;29(5): 181-188.